COUPLED MULTI-GROUP NEUTRON PHOTON TRANSPORT FOR THE SIMULATION OF HIGH-RESOLUTION GAMMA-RAY SPECTROSCOPY APPLICATIONS

A Dissertation
Presented to
The Academic Faculty

By

Kimberly Ann Burns

In Partial Fulfillment
of the Requirements for the Degree
Doctoral of Philosophy in
Nuclear Engineering

Georgia Institute of Technology

August 2009

COUPLED MULTI-GROUP NEUTRON PHOTON TRANSPORT FOR THE SIMULATION OF HIGH-RESOLUTION GAMMA-RAY SPECTROSCOPY APPLICATIONS

Approved by:

Dr. Nolan E. Hertel, Advisor
Nuclear and Radiological Engineering
Georgia Institute of Technology

Dr. Farzad Rahnema
Nuclear and Radiological Engineering
Georgia Institute of Technology

Dr. Chris Wang
Nuclear and Radiological Engineering
Georgia Institute of Technology

Dr. Bojan Petrovic
Nuclear and Radiological Engineering
Georgia Institute of Technology

Dr. L. Eric Smith
Radiation Detection and Nuclear Sciences
Pacific Northwest National Laboratory

Dr. Richard Pagh
Nuclear Materials and Engineering
Analysis
Pacific Northwest National Laboratory

Dr. Eva Lee
Industrial and Systems Engineering
Georgia Institute of Technology

Dr. William David Kulp III
Physics
Georgia Institute of Technology

Date Approved:
June 12, 2009

ACKNOWLEDGEMENTS

TABLE OF CONTENTS

LIST OF TABLES

LIST OF FIGURES

Page

LIST OF SYMBOLS

σ_0^i — Background Cross Section

$\phi^i(E)$ — Bondarenko Approximated Scalar Flux for Nuclide i

ϕ_i — Cell Averaged Flux

$f(E_n \rightarrow E_\gamma)$ — Continuum Photon Production Probability Density Function

P_n — Discrete Ordinance Order

$\phi_n(E)$ — Energy Dependent Neutron Flux

$\phi_\gamma(E)$ — Energy Dependent Photon Flux

$\varphi_g(\vec{r})$ — Energy (Group-Wise) and Spatial Dependent Neutron Flux

ℓ — Iteration Number

$\sigma_{(n,\gamma\_discrete)}(E_n \rightarrow E_\gamma)$ — Microscopic Cross Section for a Neutron with Energy E_n to Produce a Discrete Gamma Ray with Energy E_γ

$\sigma_{(n,\gamma\_continuum)}(E_n \rightarrow E_\gamma)$ — Microscopic Cross Section for a Neutron with Energy E_n to Produce a Continuum Gamma Ray with Energy E_γ

$\sigma_{(n,\gamma)}^i(E_g \rightarrow E_\gamma)$ — Microscopic Neutron Cross Section for a Reaction Producing a Gamma Ray of Isotope i

$\sigma_n(E_n)$ — Neutron Cross Section

$\omega_n(E)$ Neutron Flux Approximation

N_i Number Density of Isotope i

$\omega_\gamma(E)$ Photon Flux Approximation

$\sigma_{(n,\gamma)}(E_n)$ Photon Production Cross Section

$R(E_\gamma, \vec{r})$ Photon Production Rate

$y(E_n \rightarrow E_\gamma)$ Photon Production Yield

$p(E_n \rightarrow E_\gamma)$ Probability that an Incident Neutron with Energy E_n will produce a
                                       Continuum Gamma Ray with Energy E_γ

S_n Spherical Harmonics Scattering Order

$S(\alpha,\beta)$ Thermal Treatment of Bonded Atom

$\sigma_t^i(E)$ Total Microscopic Neutron Cross Section for Nuclide i

LIST OF ABBREVIATIONS

CAD   Computer Aided Design

DFEM   Discontinuous Finite-Element

FSDS   First-Scattered-Distributed Source

GADRAS   Gamma-Ray Detector Response Analysis Software

GEB   Gaussian Energy Broadening

HPGe   High-Purity Germanium

LCF   Last-Collided Flux

MCNP5   Monte Carlo N Particle Version 5

PGNAA   Prompt Gamma Neutron Activation Analysis

PINS   Portable Isotopic Neutron Spectroscopy

PWR   Pressurized Water Reactor

RADSAT   RAdiation Detection Scenario Analysis Toolbox

RADSAT-NG   RAdiation Detection Scenario Analysis Toolbox-Neutron Gamma

ZAID   Isotope Identification Number

SUMMARY

The accurate and efficient simulation of coupled neutron-photon problems is necessary for several important radiation detection applications. Examples include the detection of nuclear threats concealed in cargo containers and prompt gamma neutron activation analysis for nondestructive determination of elemental composition of unknown samples. In these applications, high-resolution gamma-ray spectrometers are used to preserve as much information as possible about the emitted photon flux, which consists of both continuum and characteristic gamma rays with discrete energies. Monte Carlo transport is the most commonly used modeling tool for this type of problem, but computational times for many problems can be prohibitive. This work explores the use of coupled Monte Carlo-deterministic methods for the simulation of neutron-induced photons for high-resolution gamma-ray spectroscopy applications.

RAdiation Detection Scenario Analysis Toolbox (RADSAT), a code which couples deterministic and Monte Carlo transport to perform radiation detection scenario analysis in three dimensions [1], was used as the building block for the methods derived in this work. RADSAT was capable of performing coupled deterministic-Monte Carlo simulations for gamma-only and neutron-only problems. The purpose of this work was to develop the methodology necessary to perform coupled neutron-photon calculations and add this capability to RADSAT. Performing coupled neutron-photon calculations requires four main steps: the deterministic neutron transport calculation, the neutron-induced photon spectrum calculation, the deterministic photon transport calculation, and

the Monte Carlo detector response calculation. The necessary requirements for each of these steps were determined.

A major challenge in utilizing multigroup deterministic transport methods for neutron-photon problems was maintaining the discrete neutron-induced photon signatures throughout the simulation. Existing coupled neutron-photon cross-section libraries and the methods used to produce neutron-induced photons were unsuitable for high-resolution gamma-ray spectroscopy applications. Central to this work was the development of a method for generating multigroup neutron-photon cross-sections in a way that separates the discrete and continuum photon emissions so the neutron-induced photon signatures were preserved. The RADSAT-NG cross-section library was developed as a specialized multigroup neutron-photon cross-section set for the simulation of high-resolution gamma-ray spectroscopy applications.

The methodology and cross sections were tested using code-to-code comparison with MCNP5 [2] and NJOY [3]. A simple benchmark geometry was used for all cases compared with MCNP. The geometry consists of a cubical sample with a ^{252}Cf neutron source on one side and a HPGe gamma-ray spectrometer on the opposing side. Different materials were examined in the cubical sample: polyethylene (C_2H_4), P, N, O, and Fe. The cross sections for each of the materials were compared to cross sections collapsed using NJOY. Comparisons of the volume-averaged neutron flux within the sample, volume-averaged photon flux within the detector, and high-purity gamma-ray spectrometer response (only for polyethylene) were completed using RADSAT and MCNP.

The code-to-code comparisons show promising results for the coupled Monte Carlo-deterministic method. The RADSAT-NG cross-section production method showed good agreement with NJOY for all materials considered although some additional work is needed in the resonance region and in the first and last energy bin. Some cross section discrepancies existed in the lowest and highest energy bin, but the overall shape and magnitude of the two methods agreed. For the volume-averaged photon flux within the detector, typically the five most intense lines agree to within approximately 5% of the MCNP calculated flux for all of materials considered. The agreement in the code-to-code comparisons cases demonstrates a proof-of-concept of the method for use in RADSAT for coupled neutron-photon problems in high-resolution gamma-ray spectroscopy applications.

One of the primary motivators for using the coupled method over pure Monte Carlo method is the potential for significantly lower computational times. For the code-to-code comparison cases, the run times for RADSAT were approximately 25-500 times shorter than for MCNP, as shown in Table 1. This was assuming a 40 mCi ^{252}Cf neutron source and 600 seconds of "real-world" measurement time. The only variance reduction technique implemented in the MCNP calculation was forward biasing of the source toward the sample target. Improved MCNP runtimes could be achieved with the addition of more advanced variance reduction techniques.

Table 1. Comparison of MCNP and RADSAT Computational Times for Simple Cube Problems

Simulation	RADSAT (hours)	MCNP (hours)	Run-Time Ratio
Polyethylene	5	914	183
Phosphorus	1.9	910	479
Nitrogen	3	84	28
Oxygen	3.5	93	27
Iron	5	198	40

CHAPTER 1

BACKGROUND

Neutron-induced photon signatures are an important component of many radiation detection scenarios. When a neutron interacts in matter, it can undergo a variety of interactions that can produce gamma rays: radiative capture, inelastic scatter, (n, 2n), (n, p), (n, α), (n, tritium), (n, deuterium), etc. These neutron-induced photon signatures can contribute significantly to the gamma-ray spectrum observed by the detector.

Many important radiation detection applications rely on the neutron-induced photon signatures as a primary focus of the gamma-ray spectrum. One such application includes the use of detectors at ports of entry used to identify nuclear threats concealed in cargo containers. Another application includes prompt gamma neutron activation analysis (PGNAA) for the nondestructive determination of the elemental composition of unknown samples. Both of these applications use high-resolution gamma-ray spectrometers to analyze the neutron-induced photon spectrum.

It is important to accurately predict the performance of these types of radiation detection systems. These predictions would not only aid in assessing the operational capabilities but could also identify promising paths in research. Ideally, these assessments are done through measurements in a realistic environment. Often, completing these measurements is either impractical or impossible due to time and cost constraints, or because the system does not yet exist. When performing measurements is not an option, numerical simulations become the tool of choice for calculating the detector response.

1.1 Computational Methods

The methods for modeling radiation transport problems can be divided into two general categories: the stochastic method and the deterministic method. Additionally, a coupled stochastic-deterministic method can be used to simulate radiation transport problems. In the following sections, a detailed description of each method type and its associated advantages and disadvantages for use in simulating radiation detection scenarios will be discussed.

1.1.1 Monte Carlo Methods

The Monte Carlo method uses repeated random sampling of probability distributions to determine the solution to the problem. Monte Carlo simulations can be used to solve a variety of problems of interest in "nuclear reactor design, radiation shielding, nuclear criticality safety, decontamination and decommissioning, detector design and analysis, nuclear safeguards, accelerator target design, health physics, medical tomography and radiotherapy, nuclear oil well logging, waste storage and disposal, and radiography" [4] and are the preferred tool for simulating gamma-ray spectroscopy applications. A number of computer codes apply the Monte Carlo method for solving radiation transport problems including MCNPX [5], MCNP5 [2], Geant4 [6], Fluka [7], MARS [8], and Penelope [9]. The advantages and the disadvantages of the Monte Carlo method will now be discussed briefly.

The Monte Carlo method uses the sampling of probability distributions to simulate radiation transport. By generating a statistical analogue to describe the life of a particle, random numbers can be used to determine what interactions the particle will undergo along its flight path. In order for the analogue to properly represent the particle,

the simulation must describe the physics of each interaction as accurately as possible

[10]. In order to determine the results of the experiment, many particles must be

simulated, and the expected value is obtained by determining the average behavior of the

simulated particles and the statistical error associated with the average [10].

One important advantage of the Monte Carlo method is its ability to handle

complex geometries without significant penalties in computational time. A Monte Carlo

simulation offers the flexibility to complete calculations in one-, two- or three-

dimensions. Complex three-dimensional objects are represented by quadratic surfaces in

the Cartesian coordinate system [10]. Unlike many deterministic computer codes, Monte

Carlo simulations do not have problems handling curved geometries.

Another benefit of Monte Carlo computer codes is the use of point-wise cross

section sets implemented for these calculations. (However, some Monte Carlo codes still

use multigroup cross section sets.) Pointwise cross sections allow for the cross section at

a specific energy be applied to the particle at that energy instead of an averaged cross

section over an energy range. The cross section sets implemented by these codes have

been well tested and closely approximate a continuous energy representation [1]. For

example, MCNP uses cross sections in an ACER format on an energy grid which allows

for linear interpolation between points; this interpolation scheme allows for a specified

tolerance within the continuous energy cross section [2].

The other major benefit of using a Monte Carlo simulation is the statistical nature

of the calculation. Simulating a given number of particles in a Monte Carlo code

produces a solution with a statistical uncertainty. When determining what a detector

could or could not see during a given count time, detector analysts will model the number

of particles produced during that period instead of trying to achieve a desired level of statistics thus introducing statistical noise into the system. This allows the analyst to determine if the region of interest is observable given the permitted count time. By modeling the detector response using the Monte Carlo method, the statistical nature of the problem is maintained.

Additionally, there are a number of shortcomings to overcome when utilizing Monte Carlo computer codes. Certain classes of problems can be time consuming when using the Monte Carlo method. When dealing with problems with a high degree of scatter or attenuation using analog Monte Carlo, tracking each interaction for each individual particle can become computationally expensive and cumbersome since most of the computational time is spent tracking particles that do not significantly contribute to the desired result. In order to obtain a solution with an acceptable level of error, two approaches can be implemented: run more particles or apply variance reduction techniques. Sometimes running more particles is not an option, since increasing the number of particles simulated increases the computation time required to achieve a statistically acceptable result. Additionally, the number of particles able to be simulated is dictated by the size of the random number generator. If the number of simulated particles exceeds the maximum sample size dictated by the random number generator, the simulation may yield results of sufficient precision but not accuracy (i.e. it may contain correlated samples) [10].

Alternatively, variance reduction techniques can be implemented in Monte Carlo simulations in order to reduce the number of particles sampled to achieve the desired statistical accuracy in the result, thus reducing the computational time. Implementing

variance reduction techniques requires additional time to setup the problem and is only valid for the problem at hand. Additionally, there are some types of problems where variance reduction methods provide little or no benefit.

Another major obstacle is that the Monte Carlo calculations do not provide a global solution, only the specific solution requested in the input file. If the detector location needs to be altered in a Monte Carlo simulation, the solution at the new location will have to be calculated using an entirely new simulation.

For high-resolution gamma-ray spectroscopy applications, the Monte Carlo method is the preferred method for numerical simulations by detector analysts. Monte Carlo codes allow for direct simulation of the pulse-height tally in the detector. Although Monte Carlo methods provide an accurate solution and a direct calculation of the pulse-height tally, the method can be computationally expensive when dealing with problems where scattering and attenuation are prevalent.

1.1.2 Deterministic Methods

Deterministic methods are commonly applied to nuclear reactor analysis and shielding problems; the method can also be applied to problems dealing with radiological safety, medical imaging, radiotherapy, fuel transport and storage, fusion research, homeland security and oil exploration [11]. Typically deterministic methods are not used to simulate high-resolution gamma-ray detection scenarios.

Deterministic transport codes, such as THREEDANT [12], PARTISN [13], TORT [14] and Attila [6], implement an approximation to the linearized Boltzmann transport equation; the most common of which is the discrete-ordinates method. Deterministic transport requires the discretization of the integro-differential transport

equation over space, energy and time. The discrete-ordinates method is obtained by additionally discretizing the angular variable, creating a small number of discrete directions or rays. A global solution is obtained by numerically solving the set of algebraic equations derived through the discretization process [10].

One of the main advantages of using a deterministic code is that it produces a global flux solution. Unlike in a Monte Carlo code where the user is required to define the output prior to the calculation, deterministic codes allow the user the ability to determine the solution to the calculation at any location in the problem regardless of whether or not it was specified prior to the calculation. This feature can be extremely advantageous in a detection scenario if the analyst is interested in moving the location of the detector or determining the proper location to place a detector. If the detection system is small enough that it does not directly affect the flux solution within the problem, the ability to obtain a global flux solution offers some flexibility to the problem. For this class of problems, the flux solution at any point in the problem can be obtained from the global flux solution without having to re-solve the transport problem.

Another advantage of using a deterministic code is that it produces an "infinite time solution," or a solution which does not contain the statistical uncertainty associated with Monte Carlo calculations. This is extremely advantageous when simulating long-dwell detection scenarios where little statistical noise is present and Monte Carlo simulations are very time consuming. Because deterministic transport codes calculate a numerical solution to the discretized transport equation, the code computes a solution without the statistical uncertainty associated with Monte Carlo simulations.

The third major advantage of using a deterministic code is their ability to achieve shorter computational times compared to Monte Carlo for certain classes of problems. Unlike in Monte Carlo calculations where computational time requirements is proportional to the number of particles simulated, the computational requirements for deterministic codes are directly affected by the number of discrete bins in space, energy and angle. For problems dominated by scattering and attenuation, discrete-ordinates codes have the potential to produce accurate results in relatively short computational times, when compared to Monte Carlo. This assumes that a reasonable geometric mesh size can be utilized in the problem [1].

In order to obtain accurate results using the discrete-ordinates approximation, it is important to understand the possible causes of errors. Unlike Monte Carlo simulations which implement close approximations to continuous energy cross sections, the deterministic method requires discretization in energy, resulting in multigroup cross sections. The ability to properly preserve the physics of the problem is directly related to the fidelity of the cross sections. If the cross section is varying rapidly within the energy group, errors can result from the approximation of the cross section for the group. Additionally, the methods used for the discretization of the geometry may result in some limitations on the types of geometric shapes that can be properly approximated. For instance, if a Cartesian coordinate mesh was used (i.e. cubes with faces parallel to the x-, y- and z-plane), the approximation may result in errors for volumes of spheres or other curved surfaces.

The main disadvantage to employing a discrete-ordinates code to a detector response problem is the ray effect. In the discrete-ordinates method, particles are

assumed to travel along discrete directions while preserving the overall flux. The amount and spacing of these discrete directions is determined by the order of the discrete-ordinates calculation. Low order calculations of uniform sources artificially bias the particles to travel in only a few discrete directions. This biasing of particle travel causes artificial enhancement and depression of the particle flux known as ray effects [15]. An example of the ray effects calculated of the scalar flux at a constant distance from a point source in air using a discrete ordinates approximation is shown in Figure 1 [1]. The discrete ordinates calculation should produce a uniform flux over all angels at a given distance from the source in air. At the lower discrete ordinates, the flux is artificially increased at some angles and decreased at others. As the S_n order is increased, the flux approaches a uniform solution but is computationally expensive. When modeling the detector location, it is possible to choose a position where the flux is artificially high or low. In order to mitigate this effect, the detector simulation should be carried out using a high-order angular approximation and/or using a first-collision code to generate a first collision source which will lead to an increase in the computational time required to converge on a global solution [1].
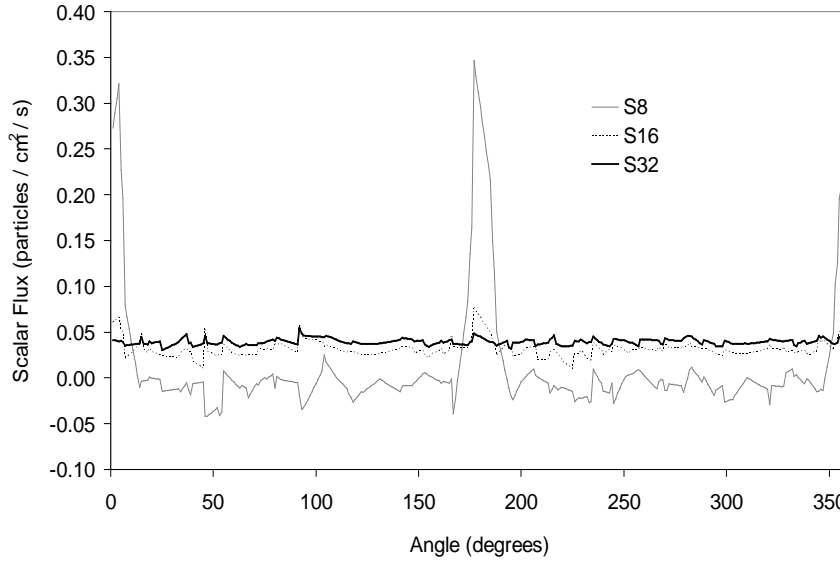
Figure 1: Example of Ray Effects Resulting from the Calculation of the Scalar Flux for a Point Source in Air. S_8, S_{16}, and S_{32} represent the S_n order used in the discrete ordinates calculation.

The other major issue encountered when using a deterministic code to simulate high-resolution gamma-ray detector response is the nature of the method. Detector response is a stochastic process. Although some work is being done to simulate the detector response directly using deterministic transport, the detector response is not typically directly simulated using deterministic transport approximations. The effects of many of the discretization errors described and the statistical nature of the detector response can be mitigated by coupling the discrete-ordinates code to a Monte Carlo simulation to obtain the detector response.

1.2   Coupled Stochastic-Deterministic Methods

Coupled stochastic-deterministic methods offer some direct advantages over pure stochastic or deterministic simulations for certain problems with a high degree of scattering or attenuation. It is possible to exploit the positive aspects while mitigating

some of the negative aspects of each of the methods acting individually. Since discrete-ordinates calculations offer advantages for determining the global flux solution, the general transport calculation is solved using a discrete-ordinates code. Due to the statistical nature of the stochastic method and its ability to accurately represent a pulse-height tally in a gamma-ray spectrometer, the final transport through the detector is simulated using a Monte Carlo code.

The coupled stochastic-deterministic method offers a number of advantages for high-resolution gamma-ray detector applications. By employing a discrete-ordinates code to calculate the global field solution, it allows for the physical size of the Monte Carlo problem to be significantly reduced, which reduces the computational time required to achieve a solution for some cases. This coupled approach also applies some additional flexibility to the simulation. For instance, if the location of the detector needs to be altered from its original location in the simulation, the flux at the new location can be extracted from the global flux solution provided from the discrete-ordinates calculation. The only additional computational time required to determine the detector response is the Monte Carlo simulation directly around the detector at the new location. The reduction in computational time requirements and the added flexibility makes the coupled discrete ordinates and Monte Carlo method attractive for certain classes of problems.

Radiation Detection Scenario Analysis Toolbox (RADSAT) is a computer interface which aids in the coupling of discrete-ordinates and Monte Carlo calculations for use in determining detector response. Attila, a discrete-ordinates code which was originally developed at Los Alamos National Laboratory and is currently updated and maintained by Transpire Inc. [16], is used to calculate the global flux solution, and Monte

Carlo N-Particle Version 5 (MCNP5) [2], which was also developed at Los Alamos National Laboratory, is used to calculate the detector response. For some instances Gamma-Ray Detector Response Analysis Software (GADRAS), a one-dimensional deterministic transport code developed at Sandia National Laboratory [17], is used in place of MCNP to calculate the detector response. Each of these computer codes were chosen for a combination of reasons: computational abilities, features, and user familiarity.

The implementation of Attila as the deterministic core of RADSAT was chosen over other deterministic codes due to the inclusion of several attractive features. Unlike most deterministic codes which employ the Cartesian coordinate system for meshing, Attila solves the transport equation using an unstructured tetrahedral mesh, allowing Attila to provide more accurate approximations to complicated geometries such as curved surfaces. Attila also has the ability to incorporate ray-tracing which is well suited for radiation detection problems and aids in the mitigation of ray effects. In order to minimize the ray effects in point source simulations, Attila implements a method called the "first-scattered-distributed source" (FSDS). The FSDS calculation consists of completing the "first-scattered" calculation to obtain a distributed source that is then used to determine the scattered source. Ray tracing is then used to determine the uncollided flux. The sum of these two components is used to determine an accurate global flux profile for the problem [1]. The second tool used to mitigate ray effects in Attila is the "last-collided flux" method or LCF. Once the global flux solution is obtained, the integral transport is applied to the user-defined edit point by transversing the mesh along many individual lines of sight to account analytically for absorption and scattering. An

LCF calculation is depicted in Figure 2. Without the ability to mitigate ray effects, the

computation of the flux on a small detector would result in erroneous solutions.
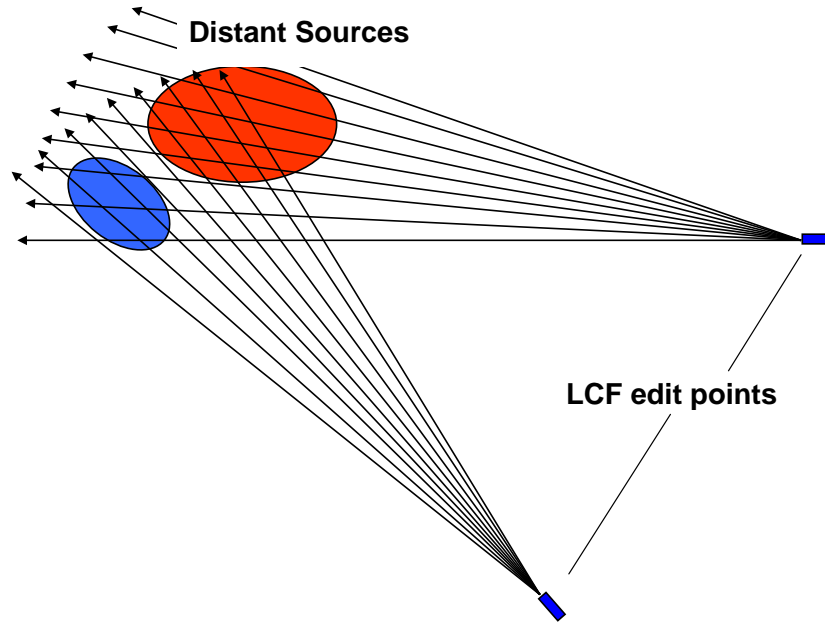
Figure 2: Illustration of last-collided flux (LCF) edit as a means to mitigate ray effects in
discrete ordinates solutions [1]

Employing MCNP instead of other Monte Carlo codes such as Geant4 offers

some advantages. The Geant4 input file is written in C and requires the user to identify

the specific physics packages required to solve the problem [6]. Alternatively, the

MCNP5 input file is more of a fixed format containing default physics packages. The

user is only required to specify the geometry and materials of the detector itself.

RADSAT generates the remainder of the input file for MCNP5 using the output file from

Attila and the source subroutine module added to MCNP5. Although development up to

this point has focused on applying MCNP5 as the Monte Carlo backend for RADSAT,

any Monte Carlo simulation code could be used to complete these calculations.

One alternative to calculating the detector response using MCNP is to employ a deterministic code to complete the calculation. The radiation detection community is familiar with the potential advantages of deterministic transport, particularly in terms of computational time for problems that can be reduced to one-dimensional approximations. This reduction to one-dimension eliminates the problems due to ray effects completely. GADRAS uses these approximations when calculating the transport in its base code ONEDANT. Once the one-dimensional transport equation has been solved, GADRAS utilizes a semi-empirical "calibration" approximation to calculate the detector response, where the one dimensional flux is assumed to be incident on a specific face of the sensor [17]. Although these methods are extremely fast at producing results, even for deep penetration problems, they "are not adequate for more complex detection scenarios, in which one-dimensional approximations are not sufficiently accurate or when using detector types that preserve directional information" [1].

Currently RADSAT has the capability to simulate detector response for neutron-only or photon-only scenarios. It cannot complete a high resolution gamma-ray calculation for photons produced by neutron interactions within the simulation. Attila possesses the capability to generate a photon spectrum from neutron interactions in coarse energy bins within the local environment, as long as the cross-section library provided contains the necessary information. For instance, the Radion15 cross-section library contains cross section data for twenty-two neutron groups (Groups 1-22) and twenty-five photon groups (Groups 23-47) [18]. When a neutron interacts producing a gamma-ray, it appears as a between group scatter starting in a neutron group and scattering into a photon group. For example, a 2-MeV neutron (Group 10) interacts with

a hydrogen atom producing a 2.223-MeV gamma-ray (Group 35). This interaction would look like a neutron scattering from Group 10 to Group 35, and no distinction between particle types would be made. This coarse energy group photon spectrum will not preserve the discreteness of photopeaks and therefore will not contain the level of detail required for use in high-resolution gamma-ray spectroscopy applications. In order to obtain the required level of detail for this application in RADSAT, a separate module was constructed to calculate the detailed photon continuum and photopeaks separately in a form that Attila can use to simulate the photon transport.

1.3   Applications of Coupled Method

The accurate and efficient simulation of coupled neutron-photon problems is necessary for several important radiation detection applications. Adding the capability to simulate coupled neutron-photon problems using RADSAT has many applications including the simulation of nondestructive assay of a uranium-hexafluoride (UF_6) cylinder, radiation portal monitor, handheld instruments used to survey people and packages, and other nondestructive assay (NDA) scenarios. The exclusion of the neutron-induced photon spectrum could omit a significant feature of the spectrum for each of these examples. The following sections give more detailed explanations of the applications and benefits of using RADSAT for coupled neutron-photon problems.

1.3.1   Interrogation of Cargo Containers

During the screening of vehicles and cargo at a border crossing, a neutron source within a cargo container may induce gamma rays in the surrounding cargo as shown in Figure 3. To simulate this scenario it is necessary to simulate the neutron-induced

photons or the detectors will not register a source within the vehicle. RADSAT would

currently only have the capability to simulate counts in the gamma-ray detectors from

gamma-ray sources explicitly defined within the problem.
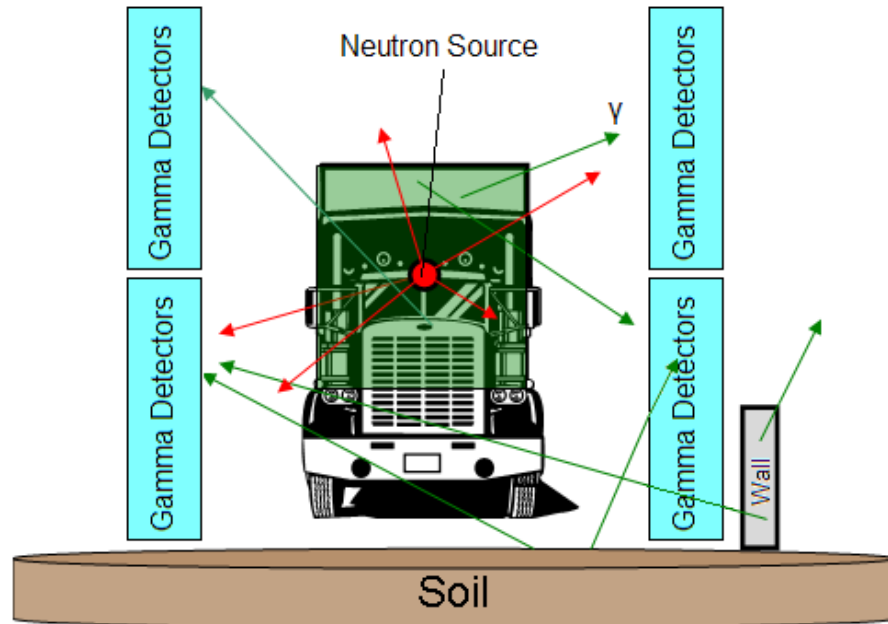
Figure 3. Passive Interrogation of Cargo Container Using Gamma Detectors to Find
Gamma Rays Produced by Neutron Interactions in the Container

The RADSAT coupled method offers many advantages for the simulation of

passive interrogation scenarios. The interrogation of cargo containers is very complex.

These are three dimensional problems, usually containing multiple sources and including

deep penetration. The large physical scale of the problem relative to the detector size

makes applying pure Monte Carlo simulations extraordinarily time consuming [19].

Also, many possible scenarios must be considered for this class of problems to determine

the response of the detectors to different classes of cargo so minimizing the computation

time is desired. With the addition of the coupled neutron photons, RADSAT is a promising tool for solving passive interrogation problems.

1.3.2   UF$_6$

The verification of declared enrichment in UF$_6$ cylinders produced at enrichment facilities is a big component of the international safeguards regimes. Various NDA methods are being utilized and considered for this application. Signatures to examine include both neutrons and gamma-rays. A significant portion of the gamma-ray spectrum produced from the UF$_6$ is due to neutron-induced photons. A diagram of a UF$_6$ cylinder and the general arrangement of such a facility are shown in Figure 4.

Being able to properly predict the results of placing a detection system around a UF$_6$ cylinder in a configuration similar to the one depicted in Figure 4 using RADSAT for the purpose of inventory would be extremely advantageous. The UF$_6$ cylinders contain a high degree of self-attenuation. Additionally, the cylinders are not isolated from each other, resulting in a high radiation background environment. The combination of these two factors makes simulating this scenario in MCNP challenging. In order to properly simulate the gamma-ray spectrum, the neutron-induced photon spectrum must be taken into account.
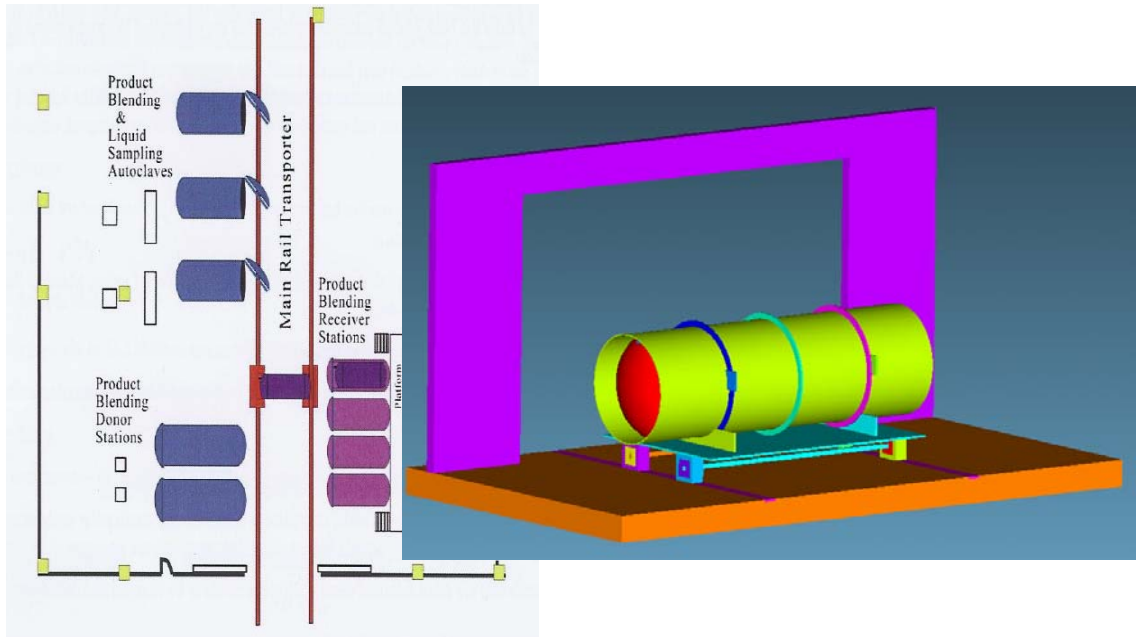
Figure 4: UF$_6$ Cylinder and Typical Facility Layout

1.3.3 Prompt Gamma Neutron Activation Analysis

PGNAA is a form of active interrogation in which neutrons are used to actively interrogate a package and nondestructively determine its contents. In this analysis, the material is irradiated with a neutron source. The neutrons interact in the material and produce gamma rays through a number of interactions, including inelastic scattering and radiative capture. An isotope can be identified using the discrete gamma rays produced from the neutron interactions. For example, hydrogen produces a 2.223-MeV gamma ray as a result of radiative capture. The presence and relative portions of these discrete gamma rays can be used to infer the chemical composition and relative abundance of the constituents within the material. In order to obtain the level of detail required to identify particular gamma-rays, the use of a high-resolution gamma-ray spectroscopy system is

required. Without the ability to account for neutron-induced photons, RADSAT will be

unable to simulate neutron activation problems altogether.

Figure 5. Prompt Gamma Neutron Activation Analysis Setup

CHAPTER 2

METHODS

Can a coupled Monte Carlo-deterministic transport code be used for the simulation of high-resolution neutron-induced gamma-ray spectroscopy? The desired outcome of this research was to add the capability to produce the detector response from a neutron-induced photon spectrum using a coupled deterministic stochastic approach to RADSAT.

2.1   Experimental Design for Testing Methods

During the initial design phase for the RADSAT coupled neutron-gamma methods, completing some of the code-to-code comparison in parallel with the development of the methodology was necessary. As a basis for testing the neutron-gamma methodology proposed for RADSAT, the RADSAT results were compared to MCNP5 results for a series of simple neutron-activation problems. The geometric configuration for these problems is shown in Figure 6 where a ^{252}Cf neutron source was placed 5 cm from one face of an 8000 cm^3 cube composed of various homogenous materials. A coaxial high-purity germanium (HPGe) spectrometer was placed 5 cm away from the opposing face of the cube.
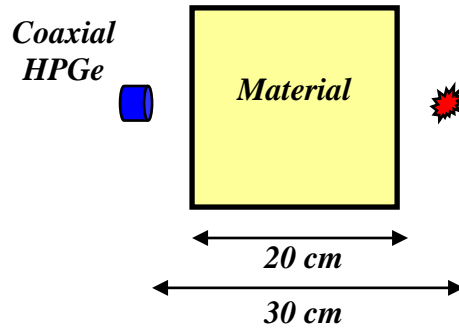
Figure 6. Source-sample-detector geometry for the neutron activation analysis problems used in code-to-code comparisons of RADSAT and MCNP5.

The simulated Ortec Detective HPGe has an active crystal dimension of approximately 5 cm in diameter by 3 cm thick with a relative efficiency of approximately 10%. The full-width at half-maximum energy resolution is approximately 3-keV at 1333-keV. A detailed graphic of the detector is shown in Figure 7. The magenta is the germanium crystal in the detector, the white is modeled as a vacuum within the detector volume, the dark blue is the aluminum detector casing, the light blue is the plastic cap on the front of the sensor, the yellow is the thin inner can cap which is modeled as low density carbon (1.01 grams/cm^3), and the green is the air surrounding the detector. This detector model had previously been utilized for another RADSAT application and was validated [1]. The original model contained a large region (10cm x 10cm x 7.5cm) of homogenized polyethylene and aluminum (14.25 grams/cm^3) behind the detector to simulate the batteries and electronics. Although this region would provide backscatter into the detector and perturb the neutron flux within the cube of moderating material, it was removed in order to examine only the induced-photon spectrum produced by the neutron irradiation of the target sample.
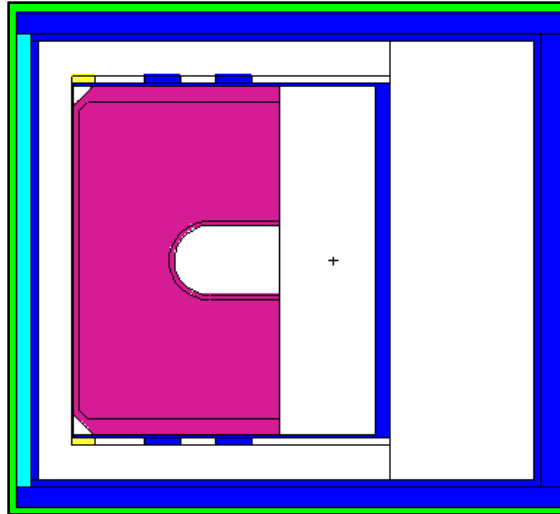
Figure 7.Schematic of the Ortec Detective HPGe. (See text for a color-coded description of the detector region)

During the method development, the composition of the target material cube was first simulated as low density (0.5 g/cm^3) polyethylene (C_2H_4). Tests were conducted using the polyethylene case to determine the effects of the neutron cross section used to solve the deterministic neutron transport problem and the spatial dependence of the neutron-induced photon spectrum. The results of these tests are discussed in the Methods Discussion Section. The same geometric configuration was also used to test several other material compositions including nitrogen, oxygen, phosphorus, and iron as discussed in the RESULTS Chapter.

2.2   Methods Discussion

Applying a coupled deterministic-Monte Carlo methods to a coupled neutron-photon problem requires the simulation to be partitioned into multiple sections. Obtaining a high-resolution detector response for coupled neutron-gamma simulations requires four steps:

1) A multigroup, deterministic neutron transport calculation of the source neutrons to all parts of the problem;

2) The generation of the corresponding spatially dependent neutron-induced gamma-ray spectrum;

3) A multigroup, deterministic photon transport calculation of the induced gamma-ray spectrum to all parts of the problem;

4) The calculation of the detector response (i.e. pulse-height tally) in a spectrometer with a Monte Carlo code.

The process is outlined in Figure 8. The methods and motivation for solving the neutron transport, photon transport to the detector location, and the detector response are previously included in RADSAT, but understanding how to utilize the individual features to solve the coupled neutron-photon simulation had not previously been addressed. The focus of the research was the development of a neutron-induced photon calculation. An explanation for completing each of the steps in Figure 8 follows.
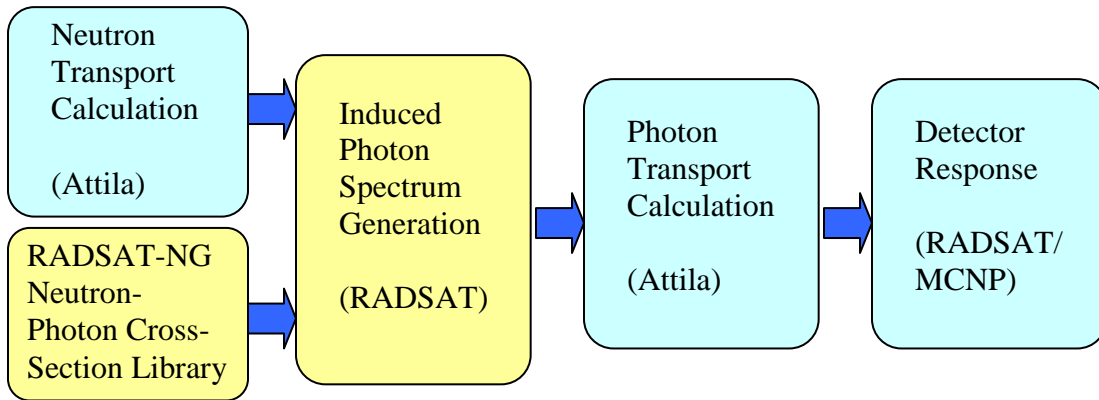
Figure 8. Procedure for Calculating Coupled Neutron-Photon Problems Using RADSAT. The blue boxes (neutron transport, photon transport and detector response) apply principles previously included in RADSAT. Yellow boxes (RADSAT-NG cross-section preparation and neutron-induced photon source generation using RADSAT) are unique steps developed in this work for coupled neutron-photon problems.

2.2.1 Neutron Transport Calculation

The first step in performing a coupled neutron-photon simulation is the neutron transport calculation using Attila. Therefore, the neutron transport utilizes a standard discrete-ordinates calculation, which is not unique to RADSAT. The required output of the neutron transport calculation is a volume-dependent neutron flux with which to calculate the neutron-induced photon spectrum. An example Attila neutron transport calculation input file for polyethylene is shown in APPENDIX A. The following sections explain the choice of neutron cross sections library, spatial dependence, transport parameters, reports, and the parameters used to determine solution convergence.

2.2.1.1 Neutron Cross-Section Libraries

The accuracy of the neutron-induced photon spectrum is directly related to the accuracy of the neutron flux which is dependent, but not solely so, on the neutron cross sections used to solve the problem. The multigroup cross sections are weighted averages

of the cross section over energy bins. The more neutron energy groups in the multigroup neutron cross-section library, the closer the representation is expected to be to the continuous energy cross section. Conversely, an increase in the number of neutron groups used to calculate the energy-dependent neutron flux in a discrete-ordinates code is directly related to the time required to obtain the global flux solution. It is desirable to achieve high degree of detail in the neutron spectrum while maintaining low computational requirements. Due to the high correlation between the energy of the neutron and both the neutron cross section and the energy of the resulting photon, it is important that the neutron interaction cross sections and the neutron flux are sufficiently resolved to allow for the proper computation of the resulting photon spectrum.

There exist a variety of multigroup neutron cross-section libraries designed to obtain solutions to an acceptable degree of accuracy for specific classes of problems. The physics of certain problems may require fine energy grouping structure in certain regions and allow coarser energy groups in other regions. There are many different reactions which may produce a gamma ray spanning a wide range of energies such as radiative capture, inelastic scatter, (n, 2n), (n, p), (n, α), (n, tritium), (n, deuterium), etc., so the energy group structure of the multigroup cross section can have a dramatic effect on the fidelity of the neutron-induced photon spectrum calculation. Some of these interactions are driven primarily by thermal neutron interactions (i.e. radiative capture in carbon has a thermal cross section of 0.135 barns and a total cross section of 0.137 barns). Conversely, threshold interactions which produce gamma rays (i.e. inelastic scatter in carbon) are dependent on the interactions of high-energy neutrons in the material. Three cross-section libraries were examined to assess which ones provide an

adequate multigroup approximation to the neutron flux for the generation of neutron-induced photon spectra: Radion15 [18], SCALE44 [20], and Kynea3 [21].

The Radion15 cross-section library was originally developed for use with Attila to solve shielding problems. The Radion15 cross-section library consists of twenty-two neutron energy groups and twenty-five photon groups. It employs a coarse neutron group structure in the thermal energy range, containing only three energy groups below 3.5-eV, and provides more detail in the high-energy region, containing 10 energy groups above 2-MeV.

The SCALE44 group cross-section library was the second cross-section library considered for use in solving the neutron transport calculation for coupled neutron-photon problems. The SCALE44 group library was developed by collapsing the SCALE 238 group library using a PWR spectrum. It was developed for the "analysis of fresh and spent fuel and radioactive waste systems" [20]. Since nuclear reactor analysis is highly dependent on the thermal neutron flux, the SCALE 44 group cross-section library consists of twenty-two energy groups below 3-eV with upscatter and only one energy group above 8-MeV.

The Kynea3 cross-section library was the final cross-section library to be considered for use in neutron transport calculations for coupled neutron-photon problems. Unlike the Radion15 and SCALE44 cross-section libraries previously described, Kynea3 was developed as a pseudo-problem independent cross-section library. Kynea3 was obtained by combining the 35 thermal energy groups with upscatter from the VITAMIN-B6 cross-section library [22] with the 44 higher energy groups from the SNAPPLE cross-section library [23]. Each of the neutron energy group structures previously mentioned

offers a different representation of the cross-section based on the intended use of the library. A comparison of the neutron energy group structure is shown in APPENDIX B. As a semi-quantitative determination of the most appropriate cross-section library to use for induced photon calculation, a direct comparison of the photon production rates for hydrogen, carbon and deuterium was calculated. The volume-averaged neutron flux within the entire polyethylene cube was calculated in Attila using each of the cross-section libraries: Radion15, SCALE44 and Kynea3. The neutron flux results obtained from each Attila calculation are compared to an MCNP calculation in Figure 9 and Figure 10. The MCNP, SCALE44 and Kynea3 simulations all use $S(\alpha,\beta)$ treatments. The total neutron fluxes calculated in Attila using SCALE44 and Kynea3 were within 1% of the MCNP simulation. The $S(\alpha,\beta)$ treatment takes into account the thermal scattering of the bonded hydrogen atom. Without the $S(\alpha,\beta)$ treatment, the thermal scattering in hydrogen is treated as a free gas. The Radion15 cross-section library does not contain the $S(\alpha,\beta)$ treatment for polyethylene which accounts for the -90.4% and 539% difference from the MCNP calculation in neutron energy groups 21 and 22, respectively. The total neutron flux calculated in Attila using Radion15 was within 14.3% of the MCNP simulation. The MCNP input file is show in APPENDIX C.
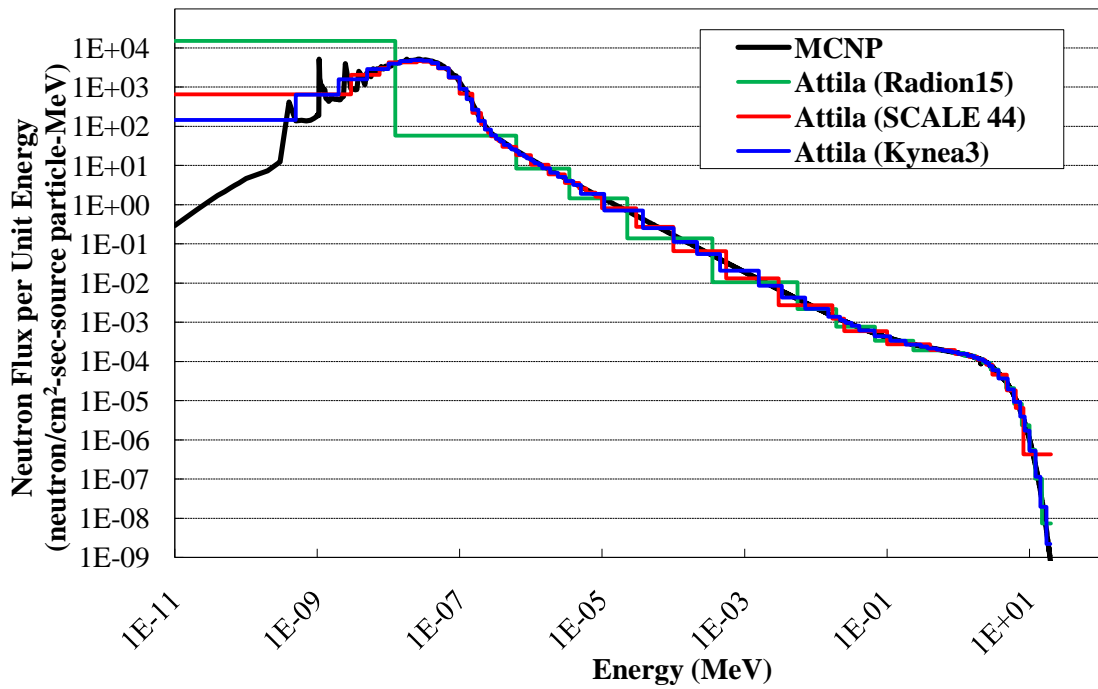
Figure 9. Comparison of Volume-Averaged Neutron Flux in Polyethylene Cube from MCNP and Attila using Radion15, SCALE44 and Kynea3 Cross-Section Libraries
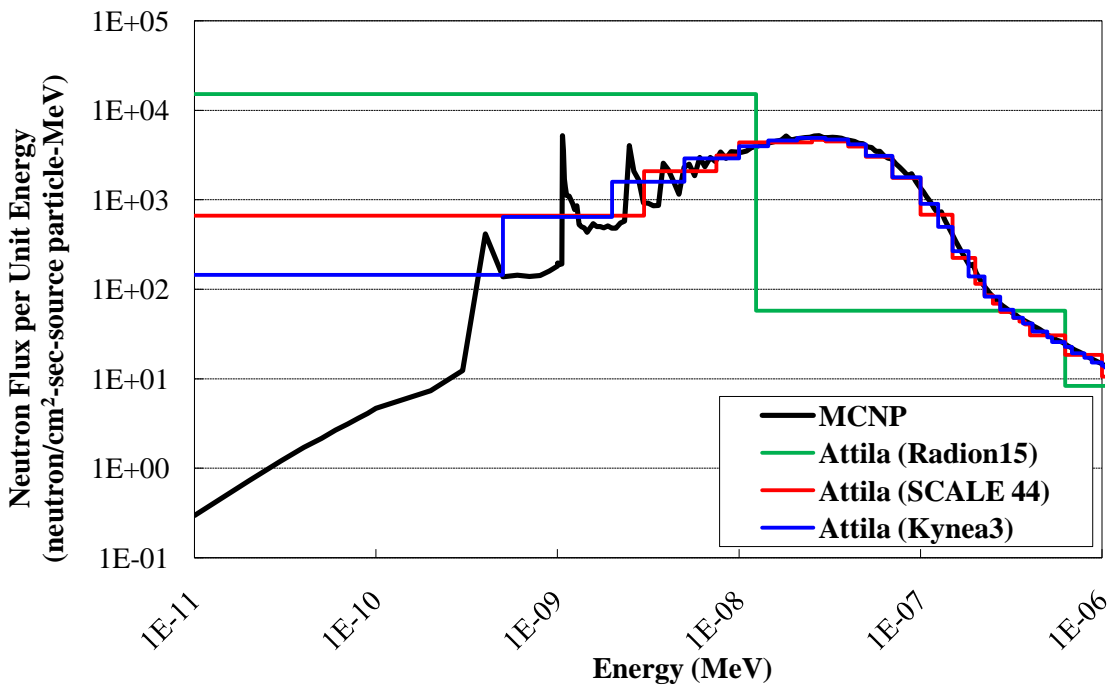
Figure 10 Comparison of Volume-Averaged Thermal Neutron Flux in Polyethylene Cube from MCNP and Attila using Radion15, SCALE44 and Kynea3 Cross-Section Libraries

The next step is to compare the total photon production cross sections for hydrogen, deuterium and carbon. None of these cross-section libraries contain the required photon production data required to simulate high-resolution gamma-ray spectroscopy, so it will be necessary to generate the photon production cross sections required. For this comparison, NJOY99.259 [3] was used to collapse the ENDF/B-VI photon production cross sections into the group structures from the Radion15, SCALE44 and Kynea3 cross-section libraries for the radiative capture interaction for hydrogen, deuterium and carbon and the inelastic capture interaction for carbon. NJOY99.259, a modular program developed at Los Alamos National Laboratory, is used to convert ENDF/B formatted cross sections into formats used by transport codes [3]. One of the modules of NJOY99.259, GROUPR can be used to generate "self-shielded, multigroup cross sections, group-to-group scattering matrices, photon production matrices, and charged-particle cross sections from pointwise input" [3], GROUPR has the ability to produce photon production matrices from pointwise data based on a user defined neutron and photon energy group structure. An additional NJOY subroutine ACER, which produces a point-wise continuous cross-section file [3], was used in order to examine the behavior of the cross section as a function of energy and to provide comparative data for the multigroup cross sections.

A comparison of the carbon radiative capture and inelastic scatter photon production cross sections are shown in Figure 11 and Figure 12, respectively. The radiative capture cross section for carbon is dominated by the thermal region which is averaged over only three groups in the Radion15 cross-section library compared to the SCALE44 group and Kynea3 cross–section libraries which contain a large number of

thermal groups. For the inelastic scattering in carbon, the SCALE44 group cross-section library spans the primary resonance with four energy groups, while the Radion15 and Kynea3 have seven and nine groups, respectively over that resonance. The more energy groups provided by a given cross-section library provide the ability to produce a higher-fidelity induced photon spectrum. The larger number of energy groups in both the thermal and high energy ranges provided by the Kynea3 cross-section library allows for higher-fidelity induced photon spectrum for both thermal and resonance-dominated cross sections.
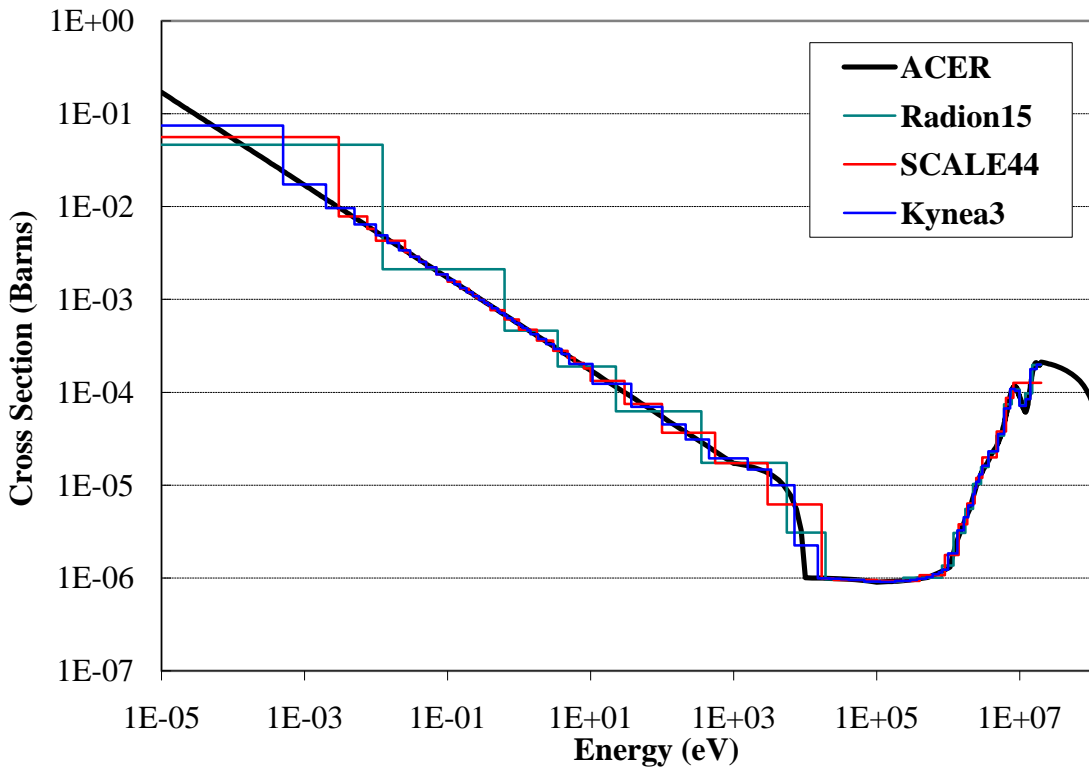
Figure 11. Carbon Radiative Capture Photon Production Cross Section in "Continuous Energy", Kynea3 Group Structure, SCALE 44 Group Structure and Radion15 Group Structure
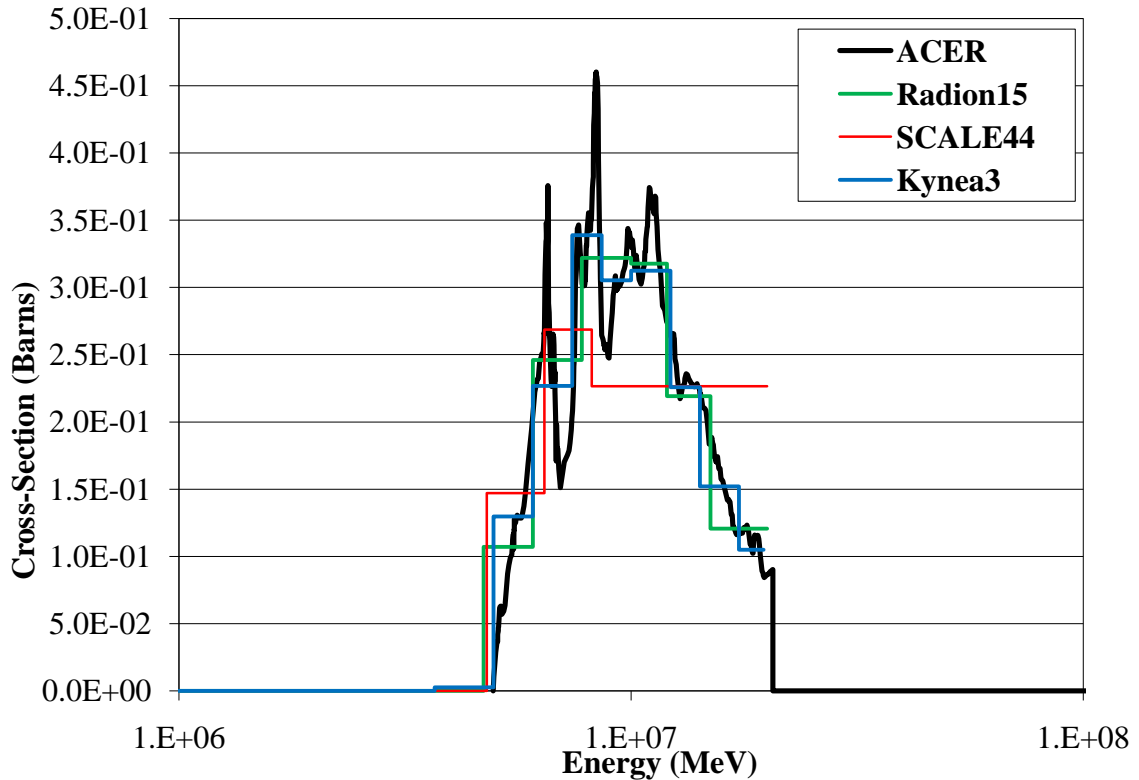
Figure 12. Carbon Inelastic Scattering Photon Production Cross Section in "Continuous Energy", Kynea3 Group Structure, SCALE 44 Group Structure and Radion15 Group Structure

A more quantitative explanation of the cross-section library choice can be seen by examining reaction rates calculated using each of the photon production cross sections. Using the neutron fluxes calculated using Attila for each cross section set and the photon production cross sections collapsed in NJOY in the appropriate energy group structures, the photon production rates in polyethylene were calculated. MCNP reaction rates were calculated and compared to the calculated photon production rates. This direct comparison of the neutron reaction rate and the photon production rate is possible for polyethylene because the photon yield for these reactions is unity where the photon yield is defined as the ratio of the photon production cross section to the neutron cross section. If the photon yield were not unity for these interactions, a direct comparison of the

neutron reaction rate and the photon production rate would not produce comparable results. The comparison is shown in Table 2. Although the neutron flux using the SCALE44 and Kynea3 cross-section libraries was within 1% of the neutron flux obtained from MCNP5, the calculated photon production rates differed by up to 2.25% for the cross sections collapsed using the Kynea3 bin structure and 4.49% for the cross sections collapsed using the SCALE44 group bin structure, both for carbon inelastic scatter. The Radion15 cross-section library overestimates the flux 14.3% when compared to the MCNP5 calculated neutron flux, because it only contains three upscatter groups and does not contain the $S(\alpha,\beta)$ treatment for polyethylene. For the cross sections collapsed using the Radion15 bin structure, the carbon inelastic scattering photon production rate differed by only 4.5%, while the hydrogen radiative capture photon production rate, which is largely dependent on the thermal neutron flux, differed from MCNP by 76.6%. The difference between the total photon production rate produced by the cross sections collapsed using the Radion15 bin structure and the total MCNP reaction rate was 77.1%. The reaction rate offered by the Kynea3 cross section neutron energy group structure will allow for more accurate generation of the induced photon spectrum, so the Kynea3 cross-section library will be used for neutron transport calculations in coupled neutron-photon simulations.

Table 2. Reaction Rates Calculated using Attila Flux and Kynea3, SCALE44 and Radion15 Cross Sections and Compared to Reaction Rates Calculated Using MCNP.

	^{1}H Radiative Capture	^{2}H Radiative Capture	C Radiative Capture	C Inelastic Scatter	Total
MCNP5 (reactions/sec-source particle)	4.74E-06	8.49E-13	2.42E-08	1.78E-07	4.94E-06
MCNP Relative Uncertainty (%)	0.01	0.01	0.01	0.02	------------
Kynea3 (reactions/sec-source particle)	4.67E-06	8.37E-13	2.39E-08	1.82E-07	4.87E-06
SCALE44 (reactions/sec-source particle)	4.91E-06	8.80E-13	2.51E-08	1.86E-07	5.21E-06
Radion15 (reactions/sec-source particle)	8.37E-06	6.51E-12	1.89E-07	1.86E-07	8.75E-06

2.2.1.2   Spatial Dependence

As the neutrons transverse material, interactions occur which alter the neutron spectrum. Due to the dependence of the neutron interaction cross section and the secondary photon energy on the neutron energy, the change in the neutron spectrum will affect the photon flux at the detector location. Since the induced photon spectrum is obtained by multiplying the energy-dependent neutron flux by the multigroup cross sections, the position dependence of the photon spectrum can be determined by examining the variation in the neutron spectrum as a function of position. Theoretically, the neutron spectrum should not change significantly in energy if the distance traveled is less than one mean-free-path, the average distance a particle travels before interacting with the material. A computational mesh can be generated to compare the variation in the neutron spectrum at multiple distances from the source throughout different materials

to help determine the required level of spatial detail required in the problem. A flux profile for the polyethylene case created using TecPlot [11] is shown in Figure 13. The flux profile graph depicts the log of the flux as a function of position. As shown by scalar flux profile graphs, there is significant flux variation as a function of position within the polyethylene cube. A slice along the z-axis at z=0 is shown in Figure 13.A, which depicts substantial flux variation through the thickness of the cube. Two graphical representations of the flux profile taken from slices along the x-axis are shown in both Figure 13.B and Figure 13.C; B was taken at the center of the cube, and C was taken 1 cm from the edge closest to the detector. The comparison of the variation in the flux profile diagrams suggests that the spatial and energy dependence of the neutron flux will have an effect on the photon spectrum at the detector location. In order to quantify this effect, a calculation was performed. The volume-averaged scalar neutron flux within entire polyethylene cube was calculated. Additionally, the polyethylene cube was subdivided into 64 equal volumes, and the volume-averaged neutron flux was calculated for each subvolume. Both the volume-averaged flux within the entire polyethylene cube and the volume-averaged flux within each of the subvolumes were used to calculate the induced photon spectrum using the procedure outlined in section 2.2.2. The photon transport calculation was then performed using the procedure outlined in section 2.2.3 to obtain the volume-averaged photon flux within the detector volume. A comparison of the photon flux in the detector calculated using the volume-averaged neutron flux within the entire polyethylene cube with RADSAT, the average neutron flux within each of the subvolumes with RADSAT and a MCNP simulation is shown in Figure 14. A comparison of the flux in each of the photopeaks is given in Table 3.
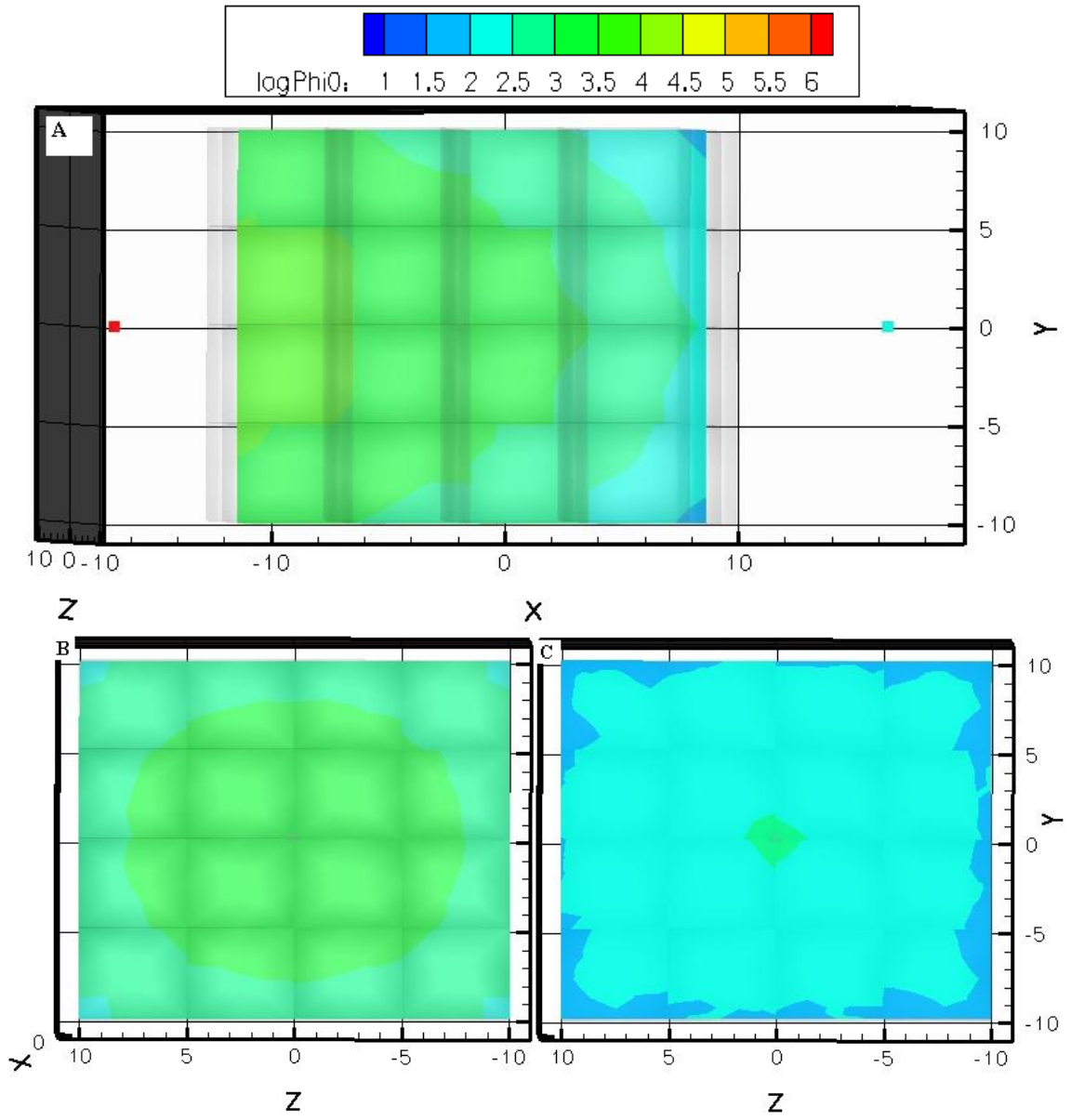
Figure 13. TecPlot of Slices of the Log of the Scalar Flux within the Polyethylene Cube. A is a slice along the z-axis at z=0, B is a slice along the x-axis at x=0 and C is a slice along the x-axis at x=9.
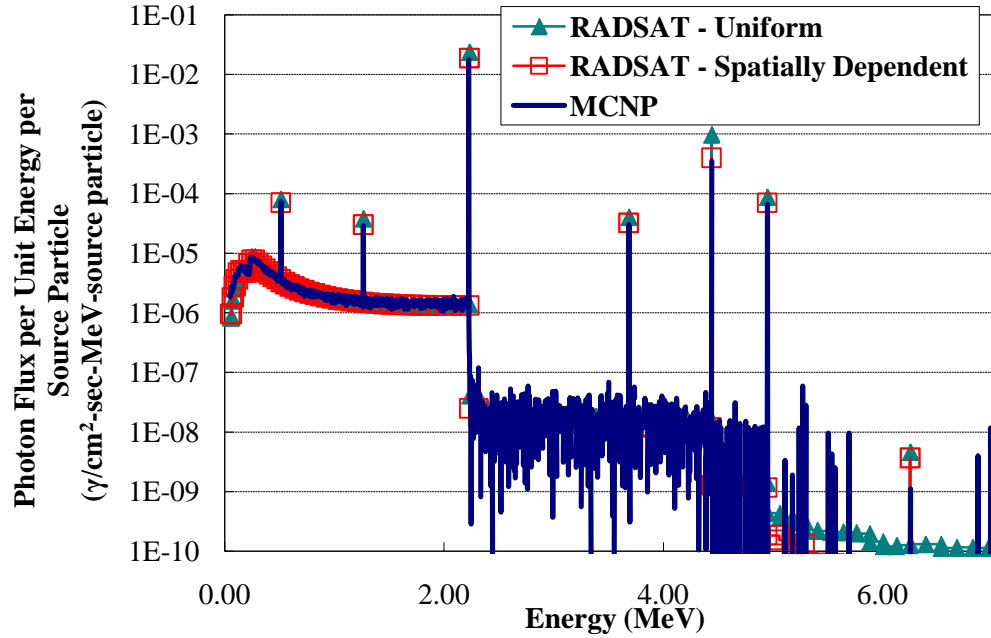
Figure 14. Comparison of Volume-Averaged Photon Flux in Detector for Uniformly Distributed Induced Photon Spectrum, Spatially Dependent Induced Photon Spectrum and MCNP

Table 3. Comparison of the Scalar Flux (γ/cm^2-sec-source particle) in Each Photopeak inside the Detector from the Irradiation of Polyethylene

	C 1.2625 MeV	^{1}H 2.223 MeV	C 3.684 MeV	C 4.439 MeV	C 4.9465 MeV	^{2}H 6.25 MeV	Total Flux
RADSAT – Uniformly Distributed	3.82E-08	2.38E-05	4.04E-08	9.77E-07	8.75E-08	4.61E-12	3.04E-05
Percent Difference (%) [Uniform and MCNP]	32.64	36.78	35.12	178.35	33.18	81.50	29.36
RADSAT – Spatially Dependent	3.01E-08	1.88E-05	3.22E-08	4.01E-07	7.01E-08	3.46E-12	2.46E-05
Percent Difference (%) [Spatial and MCNP]	4.51	8.05	7.69	14.25	6.70	36.22	4.68
MCNP	2.88E-08	1.74E-05	2.99E-08	3.51E-07	6.57E-08	2.54E-12	2.35E-05
MCNP Relative Uncertainty (%)	2.89	0.12	2.85	0.84	1.92	100	0.18

As Table 3 and Figure 14 show, there was a substantial difference in the calculated photon flux at the detector location when the spatial dependence of the neutron flux was taken into account. When the neutron flux was averaged over the entire polyethylene cube, the total photon flux reaching the detector was much too large. This has to do with the neutron flux distribution shown in Figure 13. By assuming a volume-averaged neutron flux throughout the entire cube, too many reactions were being located close to the detector. The photons produced by these reactions do not interact in the material causing more of the full energy discrete gamma rays to reach the detector location. This is particularly true for the 4.439-MeV gamma rays from the inelastic scattering interaction in carbon. The threshold for this interaction is approximately 5-MeV, and this energy neutron is only present in the region of the polyethylene cube closest to the source. By distributing the photon source uniformly throughout the cube, these gamma rays were produced closer to the detector, artificially increasing the uncollided flux reaching the detector location. The large percent difference between the 6.25-MeV gamma ray produced by the deuterium radiative capture reaction from MCNP and the spatially dependent RADSAT can be attributed to the large statistical uncertainty associated with the MCNP calculation. The log of the spatially distributed photon flux within the cube is shown in Figure 15.
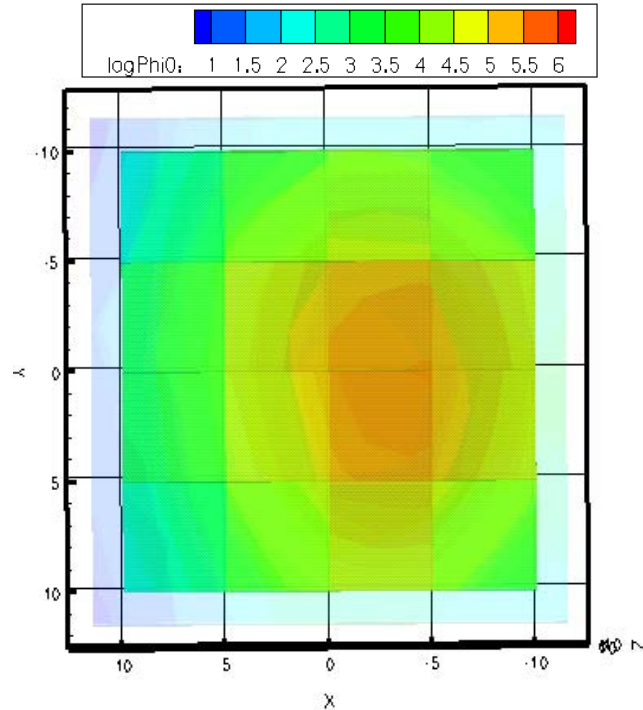
Figure 15. TecPlot of the Scalar Photon Flux within the Polyethylene Cube.

From this comparison it was determined that spatial dependence was necessary to include in the induced photon spectrum source term. It is possible in Attila to map sources to the computational mesh used for the discrete-ordinates calculation, and this method may be required for more complex problems. For the purpose of this project, the spatial dependence was handled by subdividing the volume of the cube into 64 equal subvolumes.

2.2.1.3 Neutron Transport Calculation in Attila

The neutron transport calculations were setup entirely through Attila and currently do not require the use of the RADSAT interface. The standard procedure for completing a discrete-ordinates calculation in Attila was used for these simulations: the problem geometry, cross-section library, and source spectrum must be defined; the transport

parameters and solution convergence criteria used to solve the problem must be selected; and the output parameters must be defined.

2.2.1.3.1 Problem Definition

In order to define the problem setup, three files are provided to Attila: the geometry setup file, the source definition file and the cross section file. For the benchmark cases discussed in this work, the source was defined as a ^{252}Cf Watt-Fission spectrum, and the Kynea3 cross section library was also defined.   Attila allows for the geometry of the problem to be defined using CAD (computer-aided design) models. A standard CAD model was created for all of the transport calculations using SolidWorks 2009 SP1, a commercially available CAD program [24]. The same CAD model was to be used for both the neutron and photon transport calculation because the geometry of the simulation cannot be changed between these computational steps. If the geometry of the problem was changed between the neutron transport and photon transport calculations, it could affect the solution to the neutron transport calculation, thus making the source term for the photon transport calculation incorrect. As was determined necessary in Section 2.2.1.2, the moderating cube was subdivided into 64 subvolumes within the CAD model to account for the energy spatial dependence of the neutron flux. Dividing the cube into subvolumes within the CAD model offers some advantages: it allows for easy production of specialized output files containing volume-averaged fluxes and it allows for the easy production of volume-averaged source definitions in later steps.

After the CAD model was imported into Attila, the computational mesh for the problem was created. A global mesh size of 5-cm was defined as the starting place for the iterative process. The mesh generator in Attila was used to determine the

computational mesh for the problem which contained approximately 7000 cells. Although the computational mesh was defined here, determining the appropriate computational mesh for a simulation is an iterative process and also a topic of discussion in Section 2.2.1.4.

Once the computational mesh, source and cross section files have been defined, the problem definition can be setup in Attila. First, the materials required in the problem were defined from the materials available in the provided cross-section library. Next, each region of the problem was assigned a material and density. Finally, the region the volume source occupied and the source strength were defined. It should be noted that all sources in both the neutron and photon transport calculations are volume sources in this document. In addition to defining the basic geometry, cross sections and sources necessary to complete the neutron transport simulation, the transport parameters need to be defined in order to complete calculation.

2.2.1.3.2 Transport Parameters

The transport parameters define the values required by the discrete-ordinates code to complete the calculation. The transport parameters include the angular quadrature set used discretize the simulation in angle, the scattering treatment, the scatter (P_n) and discrete-ordinance (S_n) order, and the convergence criteria for the calculation.

The angular quadrature set used to solve the neutron transport determines the approximations used to discretize the problem in angle. There are a number of quadrature sets available in Attila. The Triangular Chebyshev-Lobatto quadrature set, which is used to complete the neutron and photon transport calculations in RADSAT, places quadrature points mostly uniformly over the unit sphere and contains n^2+2n-6 total

angles, placing a point at each of the poles (+1 and -1) [11]. The integration properties of the Triangular Chebyshev-Lobatto quadrature set allow for the exact integration of "the Legendre scattering source up to and including P_2 scattering for S_4 and up to and including P_3 scattering for higher S_n orders." [11]. Although the other quadrature sets would have provided accurate solutions, the choice of the Triangular Chebyshev-Lobatto quadrature set was made for the neutron and photon transport calculation due to the decreased computational efficiency resulting from the set's integration properties and the uniformity of the distribution of the quadrature points over the unit sphere.

The scattering treatment describes the method used in the computation of the moment-to-discrete matrix. Attila includes two scattering treatments: the standard scattering treatment and the Galerkin scattering treatment. The Galerkin treatment "forces the scattering source to exactly satisfy certain spherical harmonic moment equations" which reduces the inaccuracies that can result from the standard treatment for highly anisotropic scattering [11]. Since RADSAT is designed for problems with a high degree of scattering or attenuation, the Galerkin scattering treatment was used for all of the neutron and photon transport calculations to improve the accuracy of the solution.

The discrete-ordinates (S_n) and spherical harmonic scattering (P_n) order used by Attila to calculate the transport determine the accuracy of the solution. The P_n source term accounts for the particle scattering in the problem. The integration of the spherical harmonics functions over the unit sphere, and thus the accuracy of the solution, is a characteristic of the angular quadrature set used to solve the problem. Proper treatment of the P_n scattering source "requires the use of an angular quadrature set capable of accurately integrating all the spherical harmonics moments" [11]. The P_n scattering

source term is limited by the S_n order as dictated by the angular quadrature set and scattering treatment used to solve the problem. Although iteration is performed over both the P_n and S_n order as will be discussed in Section 2.2.1.4, all of the neutron transport calculations in this document were completed using at least S_{16}/P_2.

The inner iterations, outer iterations and convergence criterion in Attila are user defined transport parameters which determine the convergence of the solution for a particular calculation. The maximum inner iterations specifies the maximum number of iterations within an energy group, and the maximum outer iterations determines the maximum number of allowable outer iterations to account for upscatter within the thermal region. Outer iterations are only necessary in problems where upscatter is present, so the maximum outer iterations for photon transport calculations is one. Both the inner and outer maximum iterations place an upper limit on the number of iterations the transport calculation will perform if the specified convergence criteria is not achieved prior to reaching the maximum. The solution meets the convergence criterion if

$$\max_i \left| \frac{\phi_i^{\ell+1} - \phi_i^{\ell}}{\phi_i^{\ell+1}} \right| < \varepsilon \qquad \text{Equation 2.1 [11]}$$

where i is the cell index, ϕ_i is the cell averaged flux, and ℓ is the iteration number [11]. For both neutron and photon transport calculations, the maximum inner iterations and the convergence criteria were set at 100 and 1×10^{-4}, respectively which are both default values in Attila. The maximum number of outer iterations for the neutron transport calculations was 200. The number of maximum outer iterations was set to 200 to ensure

that the calculation did not terminate prior to converging. These parameters were used for all of the deterministic transport calculations in this document.

2.2.1.3.3 Output Parameters

Although Attila solves the problem globally, specific outputs called reports were required to complete the induced photon calculation. Due to the required spatial dependence of the neutron flux, a specific formatting for the reports was required in order to efficiently complete the calculation. Since the spatial dependence of the problem is handled by subdividing the volumes in the CAD model, it is necessary to obtain the volume-averaged scalar flux in each of the subvolumes. Additionally a report containing the volume-averaged scalar flux within the entire cube was required. The volume-averaged scalar flux for each subvolume was used for all induced photon calculations, and the volume-averaged scalar flux over the entire cube was used for diagnostic purposes only.

2.2.1.4   Discrete Ordinates Solution Accuracy

Determining the solution convergence of the deterministic transport calculation is an iterative process. Refinement of the mesh, discrete ordinance order and scattering order should be completed to determine how the solution is changing. A numerical solution convergence is reached when the simulated solution approaches an asymptotic value. The numerically converged solution is the answer to the problem being simulated.

The consistency and stability of the numerical methods employed by Attila provide a strong foundation for the neutron transport calculations. Attila employs the discontinuous, finite-element spatial discretization (DFEM) which has been shown to be

third-order accurate for integral quantities (e.g. volume-averaged flux within a material) and second-order accurate for pointwise quantities (e.g. scalar flux at the detector location) on unstructured (tetrahedral) grids [25][26]. Additionally, the unstructured tetrahedral mesh implemented in Attila ensures that local spatial errors do not propagate throughout the entire solution [11].

The first step in the refinement process was to determine if the computational mesh has been spatially resolved. For coupled neutron-photon problems, it was important that the neutron flux solution contains no negative values and that the solution was resolved throughout the entire problem in order to properly produce the induced photon spectrum. Negative flux values can be a sign that the mesh needs to be refined in specific regions. It was also important to examine the solution for discretization errors. The flux was then visualized over the entire problem to help diagnose any obvious modeling errors or large discretization effects such as ray effects. Once the solution is examined for negative values and discrization errors, the mesh size is iterated on. This procedure was repeated several times in order to determine the appropriate mesh to use for the problem.

The second step in determining solution convergence was refinement of the discrete-ordinates (S_n) and scattering (P_n) order. An iterative process was used to determine convergence based on the S_n order. Initially, a low S_n order was used to solve the problem. Then the S_n order was increased until the solution stops changing. In addition to the S_n order, the spherical-harmonic (P_n) scattering source expansion also determines the accuracy of the solution. An iterative process was also used to determine solution accuracy based on the P_n order. The P_n order was increased iteratively within the

bounds dictated by the angular quadrature set for a given scattering treatment and S_n order. This procedure was repeated several times in order to determine the appropriate S_n and P_n order to use for the problem.

The same solution convergence criteria were applied to all photon transport calculations as were applied to the neutron transport calculations in this document. All the solutions were examined for negative values and a three-dimensional visualization tool was used to check for anomalies. Additionally, iterations were performed on S_n and P_n order to determine the appropriate transport parameters for the calculation. The coupled neutron-photon calculation required that the same computational mesh be used for both the neutron and photon transport calculations. Since the neutron transport calculation places more stringent requirements on the mesh, the mesh iterations were only completed for the neutron transport calculations

2.2.2   Generation of Neutron-Induced Photon Spectrum

The second step in simulating a prompt gamma neutron activation problem using a coupled deterministic-Monte Carlo method is the generation of the neutron-induced photon spectrum. The neutron flux obtained from the Attila neutron transport simulation was used to calculate the photon production rate in a material using Equation 2.2.

$$R\left(E_\gamma, \vec{r}\right) = \sum_{g=1}^{G} N_i \sigma_{(n,\gamma)}^i \left(E_g \rightarrow E_\gamma\right) \phi_g\left(\vec{r}\right) \qquad \text{Equation 2.2}$$

where N_i = number density of element or isotope i

$\sigma^i_{(n,\gamma)}\left(E_g \rightarrow E_\gamma\right)$ = energy dependent microscopic neutron cross section for a

           reaction producing a gamma-ray of element or isotope i

$\varphi_g\left(\vec{r}\right)$ = energy and spatial dependent neutron flux

$R\left(E_\gamma, \vec{r}\right)$ = photon production rate

The existing multigroup, coupled neutron-photon cross-section libraries are not typically used for the simulation of high-resolution gamma-ray spectroscopy. Existing multigroup, neutron-photon cross-section libraries (i.e. Radion15 cross-section library) are typically used for photon dose rate and total flux calculations rather than high-resolution gamma-ray spectroscopy. Consequently, existing cross-section libraries generally consist of a relatively few (i.e. 10-20) broad photon groups spanning energies from approximately 0.01 up to several-MeV. The broad energy groups available in current coupled neutron-photon cross-section libraries are unsuitable for the simulation of high-resolution gamma-ray spectroscopy, which requires the preservation of discrete-energy photons in order to simulate lines in the spectrum.

In addition to the energy group structure, the current format of coupled neutron-photon cross-section libraries is not suitable for high-resolution gamma-ray spectroscopy applications. Existing coupled neutron-gamma cross-section libraries combine the cross-sections for discrete and continuum gamma productions into one multigroup gamma production matrix. This means that the production rate for the characteristic discrete-energy emissions cannot be calculated separately from the continuum. Since the continuum of the gamma-ray spectrum is a smoothly varying function, a coarse energy group structure can be used to sufficiently describe it if the discrete gamma-ray

production rates can be separated from the production rates of the continuum. Using the current cross-section libraries for the calculation, the discrete gamma-ray production rates will be smeared into broad energy groups with the continuum. A specially formatted multigroup coupled neutron-photon cross-section library was developed for high-resolution gamma-ray spectroscopy applications.

2.2.2.1   Photon Production Cross-Section Library Development

In order to simulate high-resolution gamma-ray spectroscopy using a coupled deterministic-Monte Carlo method, a specialized gamma production cross section set was developed, RADSAT-NG, which overcomes the typical shortcomings of using multigroup cross sections to complete these calculations. The unique feature of RADSAT-NG is that it supports the separate calculation of discrete and continuum photons, on a reaction-by-reaction basis, from a multigroup neutron flux. The partitioning of the discrete and continuum components of the photon production cross section results in a uniquely formatted multigroup cross section library. The RADSAT-NG cross section library contains a multigroup neutron cross-section for the production of each of the discrete gamma rays and a matrix of multigroup neutron-photon cross-sections for the production of photons in the continuum. This separation allows the continuum cross-section to be expressed in coarse energy groups and the discrete energy gamma rays to be produced and transported at their exact energy (or within a very narrow energy group).

Due to the necessity to partition the continuum and discrete photon production cross sections, it was necessary to develop a methodology for the generation of the cross section set. Initially, the use of an existing cross-section preparation code that allows the user some flexibility in terms of energy group structure, in particular the GROUPR

46

subroutine of NJOY [3], was explored. Unfortunately, GROUPR does not allow

sufficient flexibility in photon group structure to achieve narrow energy bins about key

discrete-energy emissions. Additionally, GROUPR does not differentiate between a

discrete and continuum gamma ray produced by the same interaction. For these reasons,

NJOY GROUPR was not able to produce suitable cross-section libraries in this work.

Since existing cross section production methods were not capable of creating multigroup

neutron photon cross section that partition the continuum and discrete photon production

cross sections, a method for developing the RADSAT-NG cross section library was

developed.

The procedure used for producing the RADSAT-NG coupled neutron-photon

cross-section library was completed using a two step process:

1. The application of Doppler broadening,

2. The creation of point-wise cross sections (ACER format) from the raw cross-
   section data in the ENDF/B format,

3. The collapsing of point-wise data into multigroup neutron cross sections for the
   production of discrete gamma rays and a neutron-gamma production matrix for
   the production of continuum gamma rays.

The creation of point-wise cross sections from the raw cross-section data in the ENDF/B

format and the application of Doppler broadening were performed using modules within

NJOY. A breakdown of each of the NJOY modules used and the functions it performed is

provided in APPENDIX D and an example input file for NJOY to produce the pointwise

"continuous" hydrogen is shown in APPENDIX E. The collapsing of the point-wise

47

cross section data was then performed using the RADSAT-NG cross-section collapsing procedure.

2.2.2.1.1 RADSAT-NG Cross Section Collapsing Procedure

Starting from the ACER file produced using NJOY, it was first necessary to parse the data to prepare for the cross section collapsing. Since only the photon production cross sections were generated, only specific sections of the ACER file were required: the neutron cross sections, the photon production yields, photon production cross sections, and photon energy distributions. Each of these data structures were associated with a unique energy set: the neutron cross sections and the photon production cross sections were on the same neutron energy grid; the photon production yields were associated with coarser neutron energies than the neutron cross sections; and the photon energy distributions were associated with coarse neutron energies and with photon energies. The angular dependence data for the photon production was not parsed from the ACER file because isotropic photon production was assumed for all RADSAT-NG cross sections. Of the ten isotopes considered in this document, seven of them only have isotropic photon production. The remaining three have a limited number of photons produced anisotropically. Since RADSAT is intended for use in problems dominated by scattering and attenuation and many photon production interactions are isotropic, the anisotropic production of the induced photons should not drastically affect the photon flux at the detector location.

Once the ACER file was parsed, it was necessary to convert similar data into the same form. The photon production yields and the photon production cross sections contain the same data in a slightly different format. The photon production yields were

converted to photon production cross sections using Equation 2.3. Since the photon

production yields were not represented on the same neutron energy grid as the neutron

cross sections, linear interpolation was used to extrapolate the yields onto the same

neutron energy grid as the neutron cross section.

$$\sigma_{(n,\gamma)}(E_n) = \sigma_n(E_n)\, y(E_n \rightarrow E_\gamma) \qquad\qquad \text{Equation 2.3}$$

$$\textit{where} \quad y(E_n \rightarrow E_\gamma) = \frac{\sigma_{(n,\gamma)}(E_n)}{\sigma_n(E_n)} = \text{the photon production yield}$$

$$\sigma_{(n,\gamma)}(E_n) = \text{the photon production cross section}$$

$$\sigma_n(E_n) = \text{the neutron cross section}$$

In preparation for the neutron group collapsing, it was necessary to add the

neutron energies associated with the Kynea3 neutron group boundaries to the energy grid

for both the photon production cross sections and the neutron cross sections. Since the

energy grid for the photon production cross sections and the neutron cross sections was

the same, the energy grid was searched to determine if it contained the Kynea3 neutron

group boundaries. The neutron group boundaries that were not included were added to

the energy grid. The photon production cross sections and the neutron cross sections for

the added neutron group boundaries were calculated using linear interpolation.

Next the discrete photon production cross sections were separated from the

continuum photon production cross sections. Interactions were broken down into many

"sub-reactions", one for each possible discrete gamma ray that the interaction can

produce and one for the continuum. Using the photon energy distributions, the "sub-

reactions" were identified as either discrete or continuum. Once identified the discrete

photon production cross sections were stored in one array while the continuum photon production cross sections were stored in a separate data structure. This ability to obtain a cross section for each individual discrete gamma ray and one for the continuum produced by a single interaction was the cornerstone of the RADSAT-NG cross-section library.

In addition to distinguishing between discrete and continuum photon production cross sections, the photon energy distribution contained probability density functions for the production of the continuum data. In order to produce the 400 continuum groups, it was necessary to interpolate the probability density function for the continuum production to include the (401) photon energy group boundaries. 400 continuum photon groups were chosen since this allowed for equal-width energy bins (50-keV) ranging from 0 to 20-MeV. Since the probability density functions were provided in a stepwise data format as a function of photon energy, the probability density function values were assumed to be uniform within each energy group, thus linear interpolation was not used when adding the photon energy group boundaries. Next the probability density functions were interpolated over the photon production cross section neutron energy grid. Although linear interpolation was not used when adding photon energy group boundaries to the photon production cross section neutron energy grid, it was used when adding neutron energy group boundaries. Finally, the probability matrix was computed using Equation 2.4.

$$
\begin{aligned}
p\left(E_n \to E_\gamma\right) &= \int_{E_g}^{E_{g-1}} f\left(E_n \to E_\gamma\right) d_\gamma \\
&\cong \sum_{E_g}^{E_{g-1}} f\left(E_n \to E_\gamma\right) \Delta E_\gamma
\end{aligned}
$$

Equation 2.4

where $f\left(E_n \to E_\gamma\right)$ = continuum photon production probability density function

$\mathrm{p}\left(E_n \to E_\gamma\right)$ = the probability that an incident neutron with energy E_n will produce

a continuum gamma ray with energy E_γ

The appropriate neutron flux approximations were then determined for each neutron energy point on the photon production cross section energy grid. The neutron flux approximation used for the collapsing was approximated as a Maxwellian in the thermal region (1×10^{-6}-eV to 100-eV), 1/E in the epithermal region (100-eV to 50-keV), and a Watt-fission spectrum in the fast region (50-keV to 20-MeV) [27]. The reason for this flux approximation is that the anticipated neutron flux seen in many of the intended applications for the RADSAT-NG cross-section library is some variation of a fission spectrum. The source used in current applications and the benchmark cases in this document utilized a ^{252}Cf source. Some experimentation was done to determine the effect of collapsing the cross section using a different flux approximation.

The resonance self-shielding effect was then estimated for both the collapsing of the discrete and continuum cross sections using the Bondarenko method [28] as shown in Equation 2.5

$$\phi^i = \frac{\omega_n\left(E\right)}{\sigma_t^i\left(E\right) + \sigma_0^i\left(E\right)}$$

Equation 2.5

where ϕ^i is the scalar flux for the nuclide i, $\omega_n\left(E\right)$ is the neutron flux approximation, $\sigma_t^i\left(E\right)$ is the total microscopic neutron cross section for the nuclide i, and σ_0^i is the cross section for all other nuclides in the mixture excluding nuclide i per atom of the

51

nuclide i or background cross section [29]. In the Bondarenko model the flux is assumed

to vary inversely to the total macroscopic cross section. When resonances are present in

the total cross section, it produces dips in the corresponding flux profile. The background

cross section allows for the cross section to be calculated without knowing exactly what

mixtures of the isotope will be used in by assuming a constant within a given neutron

energy group. A background cross section of $1\text{x}10^{10}$ was used to create the RADSAT-

NG cross sections, which closely approximates an infinitely dilute system. Using the

neutron energies grid associated with the photon production cross sections, an array

containing the Bondarenko factor was created to use in the cross section collapsing.

Next the point-wise cross-sections for the discrete gamma rays were collapsed

into the neutron energy group structure of the Kynea3 cross-section library using

Equation 2.6.

$$\sigma_{(n,\gamma\_discrete)}^{g} = \frac{\int_{E_g}^{E_{g-1}} dE_n \sigma_{(n,\gamma\_discrete)}\left(E_n \to E_\gamma\right)\phi_n\left(E\right)}{\int_{E_g}^{E_{g-1}} dE_n \phi_n\left(E\right)}$$

$$\cong \frac{\sum_{E_g}^{E_{g-1}} \sigma_{(n,\gamma\_discrete)}\left(E_n \to E_\gamma\right)\phi^i\left(E\right)\Delta E_n}{\sum_{E_g}^{E_{g-1}} \phi^i\left(E\right)\Delta E_n}$$

Equation 2.6

where $\sigma_{(n,\gamma\_discrete)}\left(E_n \to E_\gamma\right)$ = microscopic cross-section for a neutron with energy E_n to

produce a discrete gamma ray with energy E_γ

$\phi_n\left(E\right)$ = energy dependent neutron flux

Then the continuum production was collapsed into the neutron-induced gamma production matrix using Equation 2.7. The continuum was collapsed into the neutron energy group structure of the Kynea3 cross-section library and 400 equal-width photon energy bins ranging from 0 to 20-MeV. Additionally, the lower limit threshold for collapsing continuum cross sections was set such that if the maximum continuum photon energy produced was less than or equal to 1-keV the cross section was not collapsed. This limit was set to eliminate spending computational time collapsing cross sections that would not contribute to the detector response.

$$
\sigma_{(n,\gamma\_continuum)}^{g} = \frac{\displaystyle\int_{E_g}^{E_{g-1}} dE_\gamma \int_{E_{g'}}^{E_{g'-1}} dE_n' \sigma_{(n,\gamma\_continuum)}\left(E_n' \to E_\gamma\right) p\left(E_n' \to E_\gamma\right) \phi_n\left(E'\right)\phi_\gamma\left(E\right)}{\displaystyle\int_{E_g}^{E_{g-1}} dE_\gamma \int_{E_{g'}}^{E_{g'-1}} dE_n' \phi_\gamma\left(E\right)\phi_n\left(E\right)}
$$

$$
\cong \frac{\displaystyle\sum_{E_g}^{E_{g-1}}\sum_{E_{g'}}^{E_{g'-1}} \sigma_{(n,\gamma\_continuum)}\left(E_n' \to E_\gamma\right) p\left(E_n', E_\gamma\right) \phi^i\left(E'\right)\omega_\gamma\left(E\right)\Delta E_n' \Delta E_\gamma}{\displaystyle\sum_{E_g}^{E_{g-1}}\sum_{E_{g'}}^{E_{g'-1}} \phi^i\left(E'\right)\omega_\gamma\left(E\right)\Delta E_n' \Delta E_\gamma}
$$

Equation 2.7

where $\sigma_{(n,\gamma\_continuum)}\left(E_n \to E_\gamma\right)$ = the microscopic cross section for a neutron with energy E_n to produce a continuum photon with energy E_γ

$\phi_\gamma\left(E\right)$ = energy dependent photon flux

$\omega_\gamma\left(E\right)$ = photon flux approximation

The gamma-ray flux for the collapsing was approximated as uniform over the entire energy range since the continuum photon flux should not change significantly within a particular energy group. This assumption is supported by the fact that photon cross-sections above the x-ray absorption edges are smooth and without resonance

features. Additionally, the continuum energy groups in RADSAT-NG are defined to be relatively narrow (generally less than 50-keV).

2.2.2.1.2 *Photon Production Cross-Section Library Format*

The organization of the photon production cross section is needed to support efficient calculations of the neutron-induced photon spectrum. In order to reduce the number of continuum calculations completed, thus reduce the computation time, the photon continuum production cross sections for all interactions for a given isotope were combined to form one photon production matrix for the production of all continuum photons. A calculation for the production of each discrete energy gamma ray was completed individually. The first entry in the cross section data file for a given isotope is the isotope identification number or ZAID. The first block of data preceding the ZAID contains the discrete energy gamma-ray cross sections for the isotope. The discrete energy is given in units of-MeV and followed by the multigroup neutron cross section for the discrete gamma ray. The final block of data contains the continuum photon production matrix. An example of a gamma production cross section file is shown in APPENDIX F.

2.2.2.1.3 *Photon Production Cross-Section Library Benchmarking*

Ideally, the RADSAT-NG cross-sections would be benchmarked against existing cross-sections on a reaction-by-reaction, discrete-line by discrete-line basis. Lacking an equivalent line-by-line cross-section set, the basis for benchmarking of RADSAT-NG becomes a comparison to existing multigroup cross-section sets, using the sum over all reactions, and over all discrete and continuum photon production. In order to have a

point of comparison, the GROUPR module in NJOY was used to produce multigroup

photon production. An example input file for NJOY using the GROUPR subroutine is

shown in APPENDIX G. Comparisons of the RADSAT-NG and GROUPR photon

production cross sections will be made in the RESULTS.

2.2.2.2   Neutron-Induced Photon Spectrum Calculation

Currently the calculation of the neutron-induced photon spectrum is completed

using a Visual Basic script external from the RADSAT interface. It processes the region

dependent neutron flux output file generated from the neutron transport calculation and

the required RADSAT-NG cross-section file. A separate calculation must be completed

using Equation 2.2 for each isotope in the simulation, and the user must specify the

number density for each isotope in each spatial region of the simulation. The current

output is a separate text file, called a "pseudo-isotope" file, for each isotope in each

region of the simulation. For example, the polyethylene cube case produces 194 text files

to be used as source files for RADSAT since there are three isotopes and 64 photon

production regions in the simulation. In RADSAT a "pseudo-isotope" is defined as a

commonly used spectrum, such as the cosmic ray spectrum, which is not an isotope but

does have a well-defined spectrum containing discrete photons, continuum photons, or

both. Although the induced photon spectrum are not commonly used spectrum like a

cosmic ray spectrum, the format of the "pseudo-isotope" file allows for the definition of

the induced photon spectrum as an input to RADSAT. An example "pseudo-isotope" file

for an induced photon spectrum from the neutron irradiation of phosphorus is shown in

APPENDIX H and contains both a discrete and continuum section. In the future these

calculations will be completed in the RADSAT interface, and the number densities will be obtained from the Attila neutron calculation.

2.2.3   Photon Transport

The third step in completing a coupled neutron-photon calculation for the simulation of high-resolution gamma-ray spectroscopy applications was to complete the photon transport calculation. The photon transport problem was completed in two steps: the preprocessing step which was completed through the RADSAT interface and the photon transport calculation which was completed using Attila. Both of these steps were part of the previously defined RADSAT method. While these methods were utilized heavily in this work, no modifications to the existing methodology were required in order to accommodate this new class of problems.

2.2.3.1   RADSAT Interface Process

For the coupled neutron-photon calculations, the RADSAT interface was used to simplify the source definition, define the photon energy group structure, and to produce the photon cross section library to be used in Attila.

The first step was to define the sources to be used in the Attila photon transport calculation. The isotope and region dependent induced photon spectrum calculated in the Section 2.2.2.2, in the form of "pseudo-isotope" files, were used as the photon source terms in RADSAT. A source was defined in RADSAT for each spatial region in the problem, and each induced photon spectrum was assigned to the appropriate source in RADSAT based on the spatial region in which it was produced. This combines all the

isotopes present in a specific region, so there are only two volume sources for each region in Attila, one source containing all of the discrete lines and one containing the continuum.

The second step was to determine the photon energy group structure for the photon transport calculation. The photon spectrum for each neutron-induced photon simulation is unique. Every isotope has its own unique signature, so defining a predetermined photon group structure to the photon spectrum would not allow the simulation to maintain as much detail in the gamma-ray spectrum throughout the calculation. For this reason, the photon energy group structure for the gamma problem was defined using the adaptive approach built into the RADSAT interface [1]. The upper and lower photon energy threshold, the energy weighting factor, the number of discrete photons to be included in the calculation and the number of continuum groups to be included in the calculation were defined. To preserve the important gamma-ray lines, narrow "peak" groups (typically 0.5-keV or less) were centered around the most prominent emission energies in the problem. All lower-yield discrete emissions, and any continuum source terms were then distributed into broader continuum groups that fill the energy range between peak groups. The visualization tool in RADSAT was used to iterate on the photon group structure until an appropriate group structure was created for each benchmarking problem in this document. An example of the graphical display of the RADSAT group structure for iron is shown in Figure 16. For the iron case, 149 0.3-keV wide peak groups, including one for the 511-keV annihilation peak, and 150 non-peak groups were used. A $1/\sqrt{E}$ energy weighting factor was applied to continuum groups to make finer groups in the lower energy region and coarser energy groups in the higher energy range.
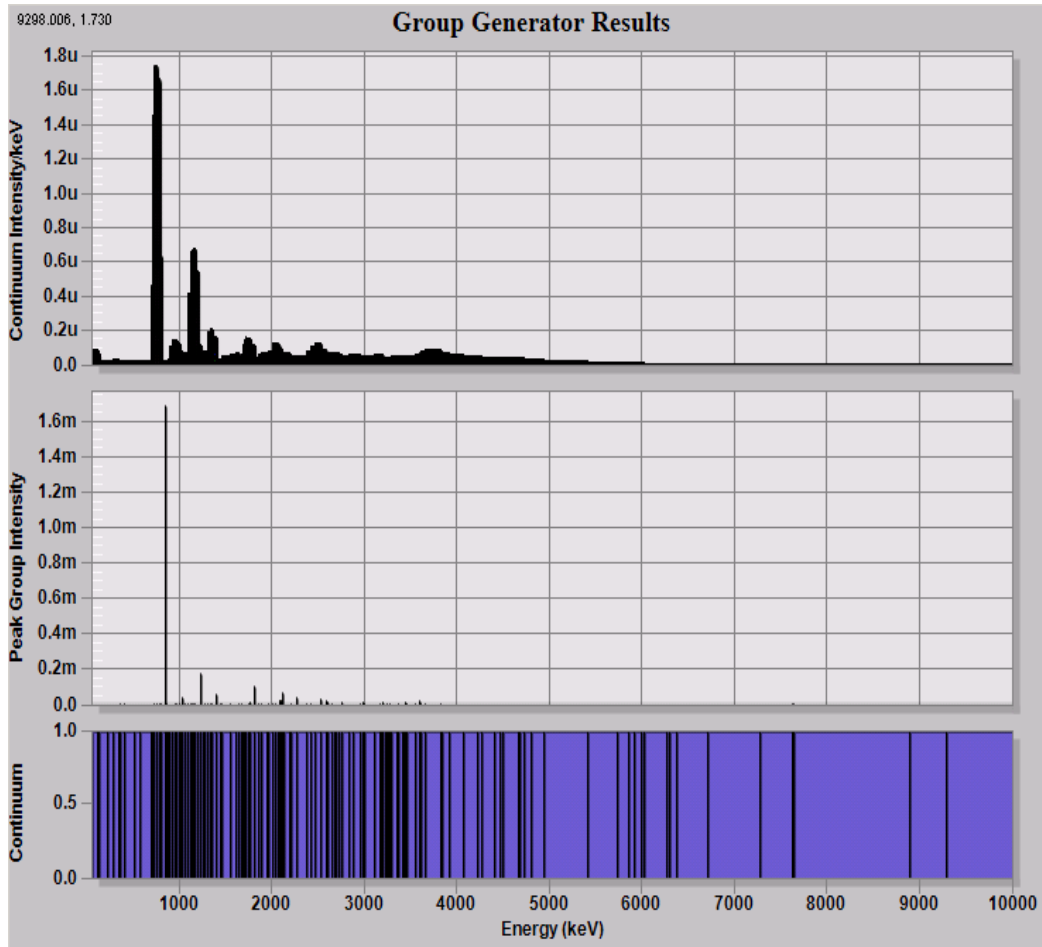
Figure 16. Adaptive Algorithm Applied to Neutron-Induced Photon Spectrum from the Irradiation of Iron

Once the energy group structure was determined using this adaptive algorithm, the group structure was used to generate a problem-specific photon cross-section library using CEPXS [30]. CEPXS produces macroscopic multigroup photon cross sections for a specified material at a particular density [30]. The CEPXS cross section file and the augmented source files in the new group structure were then used in the Attila photon transport calculation.

<u>Attila Photon Transport Calculation</u>

The RADSAT photon transport approaches are a combination of analytical ray-tracing, integral transport, and discrete ordinates methods—an approach capable of mitigating ray effects for many radiation-detection scenarios. The result of these calculations is a multigroup, discrete ordinates angular flux at all points in the problem. The angular flux can then be used for subsequent pulse-height tally calculations at the detector location.

In order to complete the photon transport, the same procedure was used as was applied for the neutron transport calculation. The CEPXS cross-section library and the regional dependent neutron-induced photon spectrum source terms were used for the photon simulations. The material must be assigned to each region of the problem. Then the volume sources were added to the appropriate regions of the problem. Since most of the induced photon spectrum were composed of both discrete and continuum emissions, typically it was necessary to assign two volume sources to a region of the problem, one for the discrete source and one for the continuum source. All of the photon-only transport calculations in this work were run with S_{16} Triangular Chebychev Legendre angular quadrature set and a minimum of P_2 Galerkin scattering moments. The same required checks for solution convergence were applied for the photon transport calculations.

The output parameters used for the photon transport calculation are different than those used for the neutron transport calculation. In order to compare the volume-averaged photon flux to that obtained from MCNP, the energy-dependent volume-averaged scalar flux edit was obtained. To obtain the required input for the detector

response calculation, the multigroup angularly discretized photon flux at the detector location is calculated using the Attila LCF edit [11], an approach described more fully in [1] and [19]. The Triangular Chebychev Lobatto quadrature set with an S_{128} was used for the LCF calculation. The Triangular Chebychev Lobatto quadrature set was used because it has a quadrature point forwardly directed.

Although in a typical coupled neutron-photon calculation the photon flux within the detector volume would not be calculated, the comparison of the volume-averaged photon flux is more diagnostically relevant to this method development work than the detector response. Understanding if the proper induced photon spectrum was created within the moderating material and properly represented as a source term in Attila needed to be tested. The calculated photon production rate calculated within a volume could be compared to a reaction rate tally in MCNP if the photon yield for the interaction was unity, but this is not typically the case and could only be done for hydrogen, deuterium and carbon. This testing was completed through the comparison of the volume-averaged photon flux within the detector volume for all remaining benchmarking cases.

2.2.4 Detector Response Calculation

The final step was calculating the high-resolution gamma-ray spectrometer response for the prompt gamma neutron activation problem. The photon flux at the detector location obtained from Attila was used as the source definition for the detector model in MCNP. This energy-dependent angular flux was then used as the source term for a "near-field" Monte Carlo simulation for pulse-height tally in the gamma-ray spectrometer [1] [19]. This coupled deterministic-Monte Carlo approach combines the attractive advantages of deterministic transport for the radiation field calculations

throughout a problem, with the inherent strength of Monte Carlo methods to calculate accurate pulse-height tallies for gamma-ray spectrometer modeling. The pulse-height tally was calculated using MCNP5 in this work, and recorded in uniform, narrow energy bins (typically 1-keV wide or less). The detector response reflects the angular fidelity of the Attila photon flux calculation as the coordinate system of the detector-scale Monte Carlo simulation was forced to be consistent with the coordinate system of the large-scale Attila calculation. While this method was utilized in this work, no modifications to the existing methods were necessary to facilitate the inclusion of this new class of problems. A detailed explanation of the mechanics and utility of the RADSAT coupling method is provided in [1] [19].

CHAPTER 3

RESULTS

Once the generally methodology had been developed, testing the methodology using code-to-code comparisons was an important part of the verification process. Completing the code-to-code comparison will indicate the capabilities and shortcomings of the method used in RADSAT to generate neutron-induced photons in material. This chapter contains the results of the code-to-code comparisons completed as part of the verification of the methodology using polyethylene, phosphorus, nitrogen, oxygen, and iron as materials of interest.

3.1   Polyethylene

Polyethylene was chosen as the first test case for the newly developed RADSAT neutron-gamma method for a number of reasons: the small number of neutron reactions which generate gamma rays, it is a molecule and not just an element, and the frequency that the material and/or its constituents would be exposed to neutrons. One frequent use for polyethylene is as a neutron shielding material and therefore often present around nuclear systems. Additionally, polyethylene and its constituents are present everywhere.

Many of the comparisons for polyethylene were included in Chapter 2 since it was used as the test case for decision making in the method development process. A comparison of the scalar neutron flux over all the entire neutron energy range and the thermal range within the polyethylene cube for Attila and MCNP are shown in Figure 9 and Figure 10, respectively. A comparison of the photon flux in the detector calculated using the volume-averaged neutron flux within the entire polyethylene cube with

RADSAT, the average neutron flux within each of the subvolumes with RADSAT and a MCNP simulation is shown in Figure 14. The comparison of the RADSAT-NG and GROUPR cross-section libraries and the comparison of the MCNP and RADSAT detector responses are given in the following sections.

3.1.1 Cross Sections

Neutron interactions in polyethylene do not produce many gamma rays. None of its constituents produce any continuum gamma rays at all. Hydrogen has two naturally occurring isotopes, ^{1}H and ^{2}H with 99.9885% and 0.0115% natural abundance, respectively. Hydrogen and deuterium only produce one gamma ray each, both of which are from radiative capture. Carbon (elemental) produces four: three from radiative capture and one from inelastic scatter. The ^{1}H, ^{2}H and C RADSAT-NG cross sections were collapsed from the ENDF/B-VI cross section data at 300K. A comparison of the newly developed RADSAT-NG cross sections and the cross sections collapsed using GROUPR for the radiative capture cross sections for hydrogen, deuterium and carbon and the carbon inelastic scattering cross section are shown in Figure 17, Figure 18, Figure 19 and Figure 20, respectively.
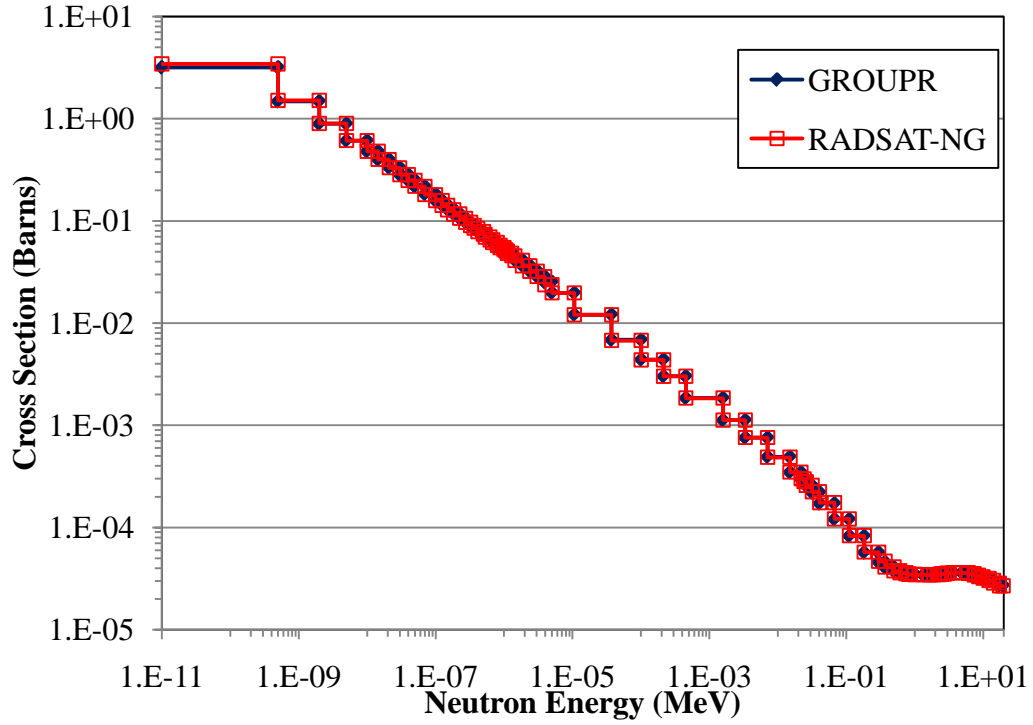
Figure 17. Comparison of Hydrogen Radiative Capture Photon Production Cross Section for RADSAT-NG and GROUPR
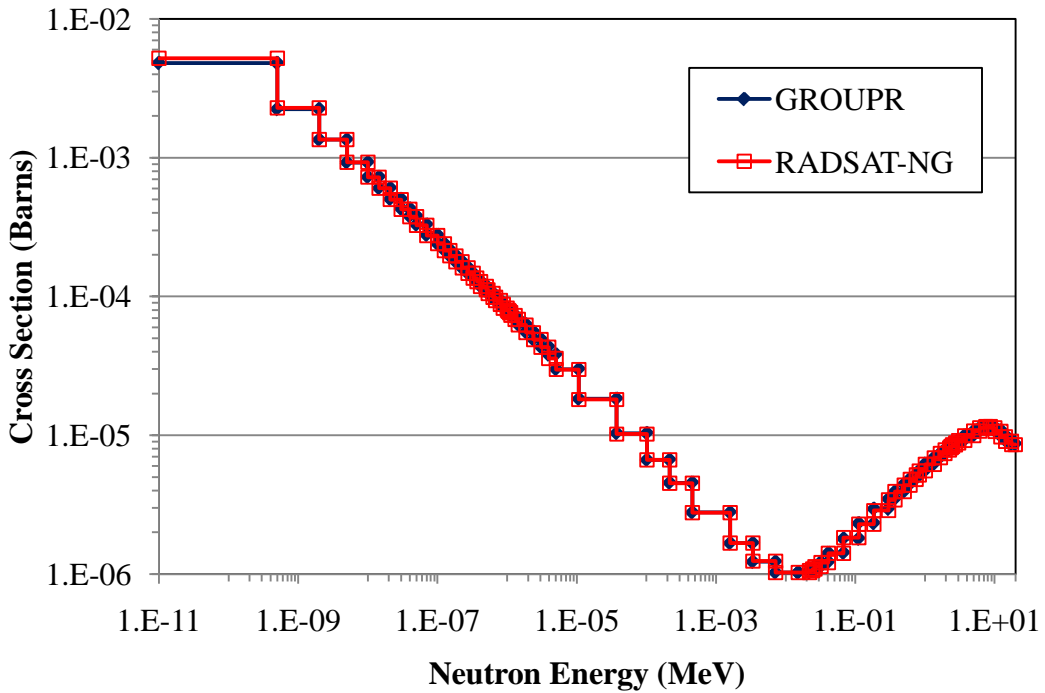
Figure 18. Comparison of Deuterium Radiative Capture Photon Production Cross Section for RADSAT-NG and GROUPR
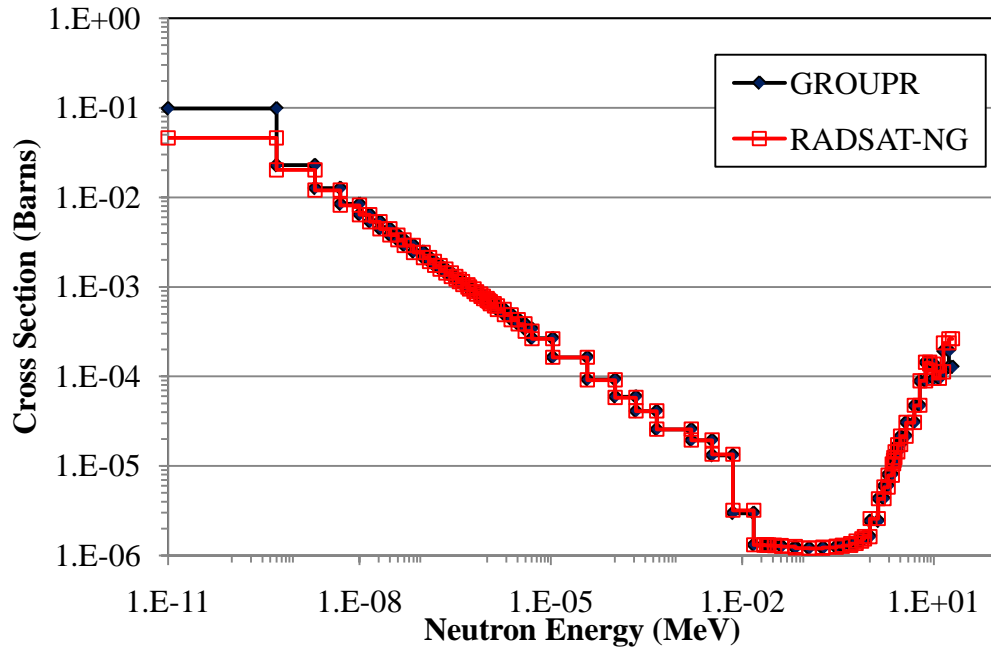
Figure 19. Comparison of Carbon Radiative Capture Photon Production Cross Section for
RADSAT-NG and GROUPR
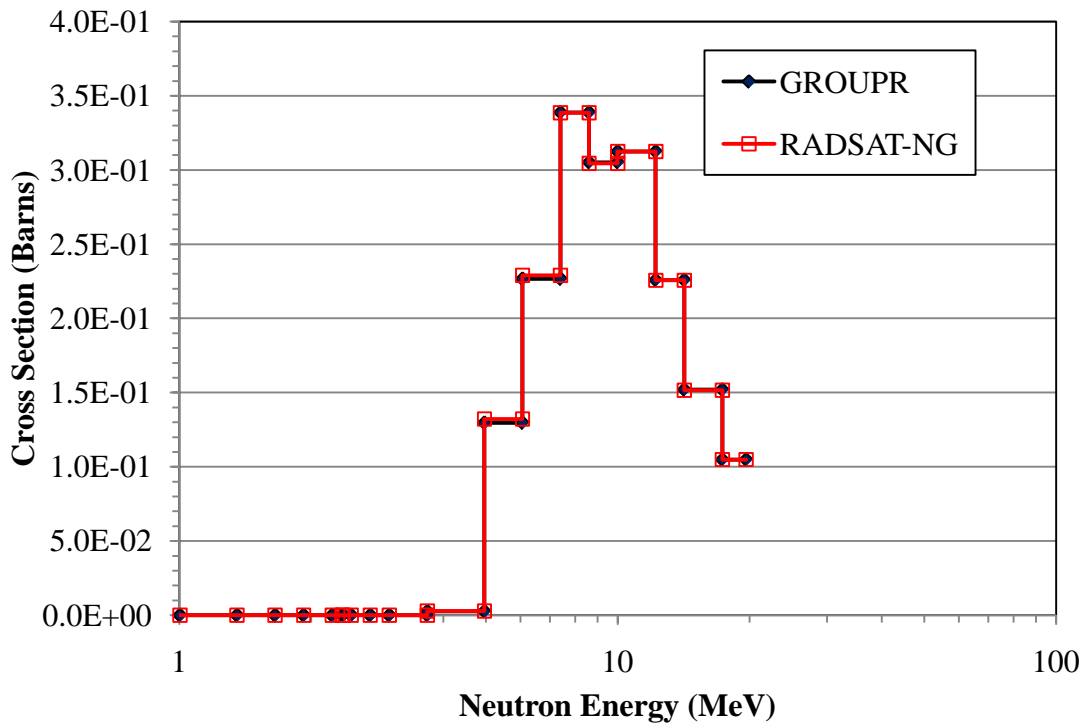
Figure 20. Comparison of Carbon Inelastic Scatter Photon Production Cross Section for
RADSAT-NG and GROUPR

The radiative capture cross sections for hydrogen, deuterium and carbon are all smoothly varying functions of neutron energy causing the collapsed cross sections to also be relatively smooth functions. A comparison of the total radiative capture cross section in hydrogen, deuterium and carbon for RADSAT-NG and collapsed using GROUPR are within 3%. The inelastic scattering cross section for carbon is a threshold interaction, so the inelastic scatter photon production cross section in carbon is zero below 4.85-MeV. Unlike the radiative capture cross section, the inelastic scattering cross section for carbon does not smoothly vary with neutron energy as was shown previously in Figure 12. Although there is some variation in the collapsed results, the total carbon inelastic scattering cross section for RADSAT-NG and GROUPR differ by less than 3%. Table 4 contains a comparison of the RADSAT-NG total cross section, total cross sections collapsed using GROUPR, the group containing the maximum variation, and the group containing the minimum variation for the hydrogen, deuterium and carbon radiative capture cross section and the carbon inelastic scatter cross section.

Table 4. Comparison of Total Cross Section for RADSAT-NG and Cross Sections Produced by GROUPR for Hydrogen, Deuterium and Carbon

Cross Section	RADSAT-NG Total Cross Section (Barns)	GROUPR Total Cross Section (Barns)	Percent Difference	Group # Largest % Difference	Group # Smallest % Difference
^{1}H Radiative Capture	10.424	10.12	3.02%	Group #79 (7.84%)	Group #14 (1.78E-3%)
^{2}H Radiative Capture	0.0161	0.0156	2.79%	Group #79 (8.51%)	Group #14 (7.20E-3%)
C Radiative Capture	0.141	0.137	1.56%	Group #1 (105.8%)	Group #33 (4.68E-3%)
C Inelastic Scatter	1.80	1.83	3.08%	Group #9 (37.4%)	Group #6 (5.86E-1%)

Most of the discrepancies between RADSAT-NG and GROUPR for hydrogen, deuterium and carbon were minor. For the carbon radiative capture photon production cross section, the RADSAT-NG cross section for energy group 1 appears to be approximately a factor of 2 greater than the GROUPR collapsed cross section. Also, the GROUPR set shows the cross section for group 1 lower than the cross section for group 2. Upon examining the pointwise cross section data obtained from ACER, which is shown graphically in Figure 11, it was noted that the cross section data were not decreasing in magnitude from the data within group 2. It was also noted that the largest percent difference for the RADSAT-NG and GROUPR radiative capture cross sections for hydrogen and deuterium were in group 79, and the largest percent difference for the carbon inelastic scatter reaction was in group 9, the first energy group containing a cross section. The discrepancies in the first and last energy group containing a cross section were investigated but no obvious data handling differences were found. The NJOY source code was examined to determine if there was a special treatment applied in this bin, but none could be found. It should be noted that although the comparison was made to GROUPR, it was determined that exactly replicating the data produced by GROUPR was not necessary. The differences were noted and the cross section set was tested through benchmarking against MCNP problem.

3.1.2 Detector Response

In order to show how the photon angular flux at the detector location translates to the detector response, the calculation of the detector response using the RADSAT method was completed. As stated in Section 2.2.4, the detector response calculation is part of the existing RADSAT package and was only drawn upon for these simulations. The

RADSAT method entailed a near field MCNP calculation containing only the detector using the photon angular flux calculated in Attila as the source term. The photon angular flux was calculated using the spatially dependent neutron-induced photon spectrum as the source term for the photon transport calculation as indicated in Section 2.2.1.2. This was then compared to a full scale MCNP calculation which included the full geometry for the neutron activation analysis of polyethylene and the results are shown in Figure 21. The same detector geometry was specified in both the RADSAT and MCNP simulations as outlined in Section 2.1, and the same Gaussian energy broadening (or GEB) was applied to both spectra. The GEB in MCNP is a parameter that allows one to "specify the full width at half maximum of the observed energy broadening in a physical radiation detector" [2].
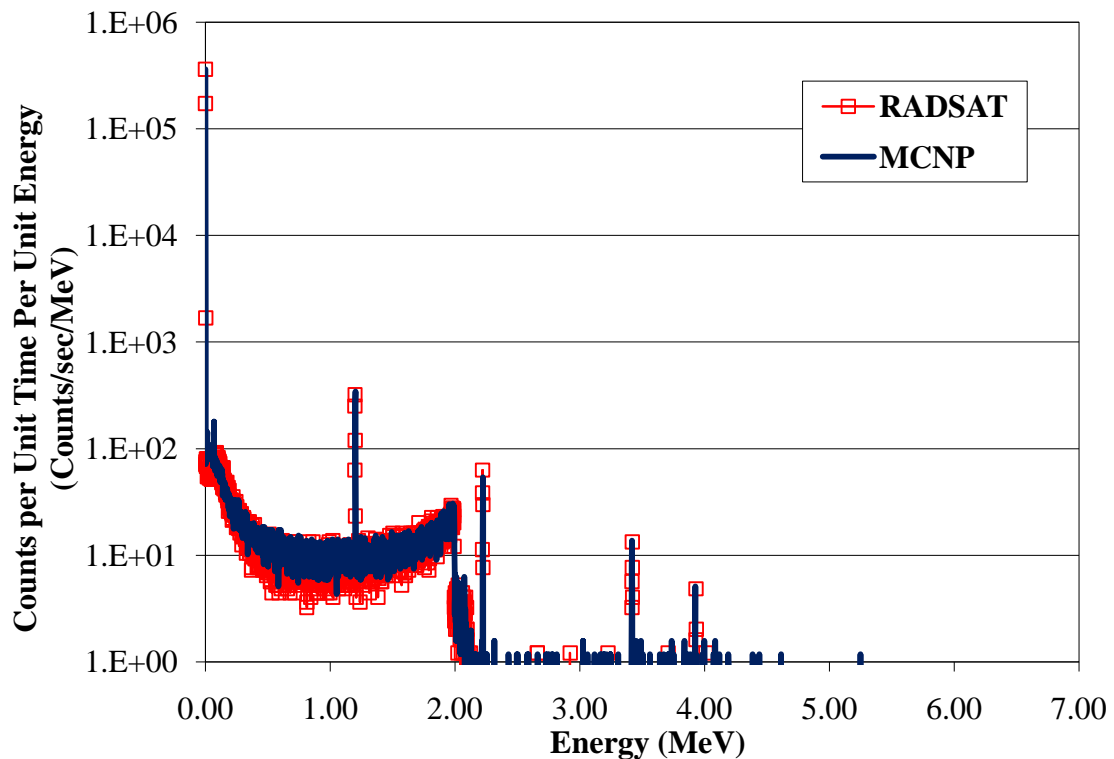
Figure 21. RADSAT and MCNP Detector Response for Neutron Irradiated Polyethylene

The total count rate in the prominent peak regions agreed to within 5% for the RADSAT and MCNP simulations. The statistical uncertainty of the MCNP simulation varied from 3.9% in the region of the 1.2-MeV line to 27.7% in the region of the 3.9-MeV line. The large statistical uncertainty associated with the MCNP calculation is due to the short count time (600 second). Additionally, the double-escape peak at 1.20-MeV is enhanced due to the small detector size.

3.2   Phosphorus

Phosphorus was chosen as the next benchmarking experiment to study an increased complexity in the cross sections. Phosphorus is commonly found in fertilizer, pesticides, explosives, fireworks, nerve agents, detergents and toothpaste. Knowing the neutron-induced photon spectrum from phosphorus could allow for the identification of explosives or nerve agents using active interrogation methods.

3.2.1   Neutron Flux Comparison

Although blocks of solid phosphorus are not found in nature due to its high chemical reactivity, a solid block of pure phosphorus was modeled to test the accuracy of the RADSAT-NG cross section. The density of the phosphorus was modeled at 1.82 grams/cm^3, the natural density of phosphorus [31]. Unlike in the polyethylene simulation, the phosphorus cube does not shield the germanium detector from fast neutrons. Since the purpose of these benchmarking cases was not to simulate the activation of the germanium detector, the neutron importance within the detector in the MCNP simulation was set to a very small number, 1×10^{-10}, reducing the number of neutron interactions that will occur within the volume of the germanium detector. This

will reduce the effect of the detector on the volume-averaged photon flux within the detector volume. By reducing the neutron importance in the detector material, the backscatter from the detector into the phosphorus cube is also reduced. Additionally, MCNP will not allow importance weighting in problems where pulse-height tallies are calculated. Although the comparison to the detector response is important, the method of calculating the detector response from the photon angular flux in Attila was unaltered as part of the method development in this work. This method has been well tested and proven to work in previous RADSAT publications [1][19]. Additionally, the detector response comparison has been made for the polyethylene case in this work. Since it is more diagnostically relevant for testing this new method to compare only the activation of the material of interest for a given benchmark problem, the importance weighting was used for phosphorus and all the other materials except polyethylene. A comparison of the volume-averaged neutron flux within the phosphorus cube for MCNP and Attila is shown in Figure 22.
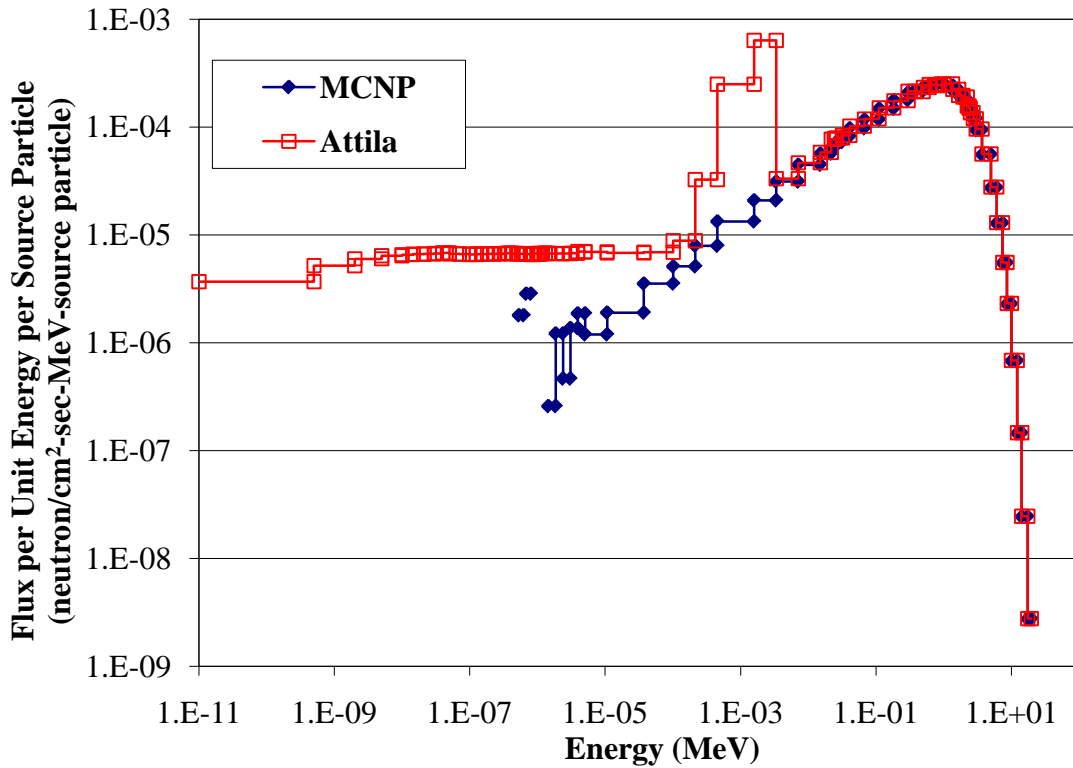
Figure 22. Comparison of Attila and MCNP Neutron Flux for the Irradiation of
Phosphorus

The Attila result is able to resolve the entire solution, whereas MCNP does not

obtain a result in every energy bin. The statistical uncertainty for the MCNP calculation

from 13.7-eV to 10.7-eV is 9.04%, and the statistics below 5-eV are above 42.82%.

There is a bias in the Attila neutron flux results which is seen in all of the remaining

neutron transport cases below approximately 50-eV. It is believed that this bias is due to

the small number of neutrons which actually scatter into this region. Additionally, the

discrepancy in the neutron flux from Attila in the energy range of 0.214-keV to 3.35-keV

appears to be an artifact of the Kynea3 cross-section library. Analysis of the original

ENDF/B-VI data, the data from which the Kynea3 cross section library was derived, does

not indicate the presence of a multiplicity interaction (n,*n) that would account for the

increase in neutrons in this energy range. Tests were also completed with MCNP using

ENDF/B-VI.0 cross section instead of the ENDF/B-VI.6 cross section for phosphorus to

determine if the shape was an artifact of the cross section library, but the shape could not

be reproduced.   Comparisons can be made using more realistic materials and

experimental setups to test the biasing in the thermal region, so the computational models

can be compared to experiment to determine which method is more accurately depicting

the neutron spectrum. Additional comparisons of the neutron transport methods were

outside the scope of this body of work. The total neutron flux for the Attila calculation

was within 1.07% of the neutron flux calculated by the MCNP simulation. A comparison

of the total neutron flux is shown in Table 5.

Table 5. Comparison of Attila and MCNP Total Neutron Flux for the Irradiation of Phosphorus

MCNP Flux (Neutron /cm^2-sec-source particle)	MCNP Statistical Uncertainty	Attila Flux (Neutron /cm^2-sec-source particle)	Percent Difference
7.67x10-4	0.01%	7.75x10-4	1.07%

3.2.2   Cross Sections

Like polyethylene, phosphorus does not have a complex induced gamma-ray

spectrum. Within the Kynea3 energy range, the cross section data for ^{31}P designates that

two continua are produced, one by radiative capture and one by an unidentified

interaction, in addition to two discrete gamma rays produced by an unidentified reaction.

In the ENDF format, photons produced by unidentified reactions are designated as

originating from "nonelastic interactions." Table 6 contains a list of the gamma-ray

producing interactions in ^{31}P and the discrete gamma rays produced by each interaction.

All of the photon production cross sections for phosphorus are smoothly varying

functions of energy containing no resonances. The ^{31}P RADSAT-NG cross sections were

collapsed from the ENDF/B-VI cross section data at 300K. A graphical comparison of

the RADSAT-NG and GROUPR radiative capture cross section and "nonelastic" cross

sections for phosphorus are shown in Figure 23 and Figure 24.

Table 6. Discrete Gamma Rays Produced by ^{31}P

Reaction	Gamma Rays (MeV)
Nonelastic	1.266, 2.234
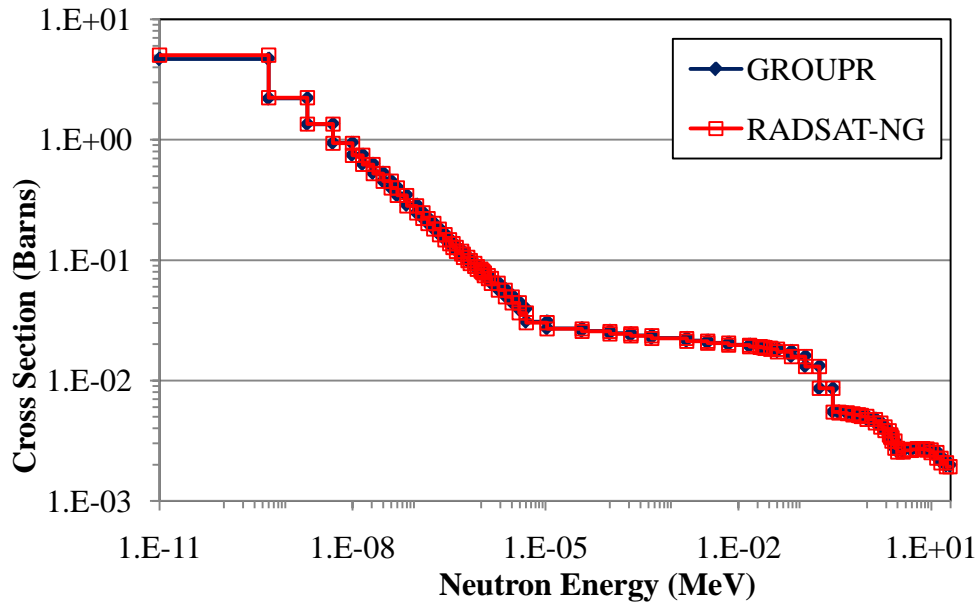
Figure 23. Comparison of Phosphorus Radiative Capture Photon Production Cross
Section for RADSAT-NG and GROUPR

The comparison of the RADSAT-NG and GROUPR collapsed cross sections

show good agreement for phosphorus. The total RADSAT-NG radiative capture and

"nonelastic" cross sections are within 0.1% and 1.9% of the GROUPR collapsed cross sections, respectively. The energy group with the largest percent difference for the radiative capture cross section was group number 79 at 7.5%. Energy group 19, the first energy group containing a cross section for the "nonelastic interaction" in phosphorus, has a difference of 7.84%. A comparison of the RADSAT-NG total cross section, total cross sections collapsed using GROUPR, the group containing the maximum variation, and the group containing the minimum variation is shown in Table 7.
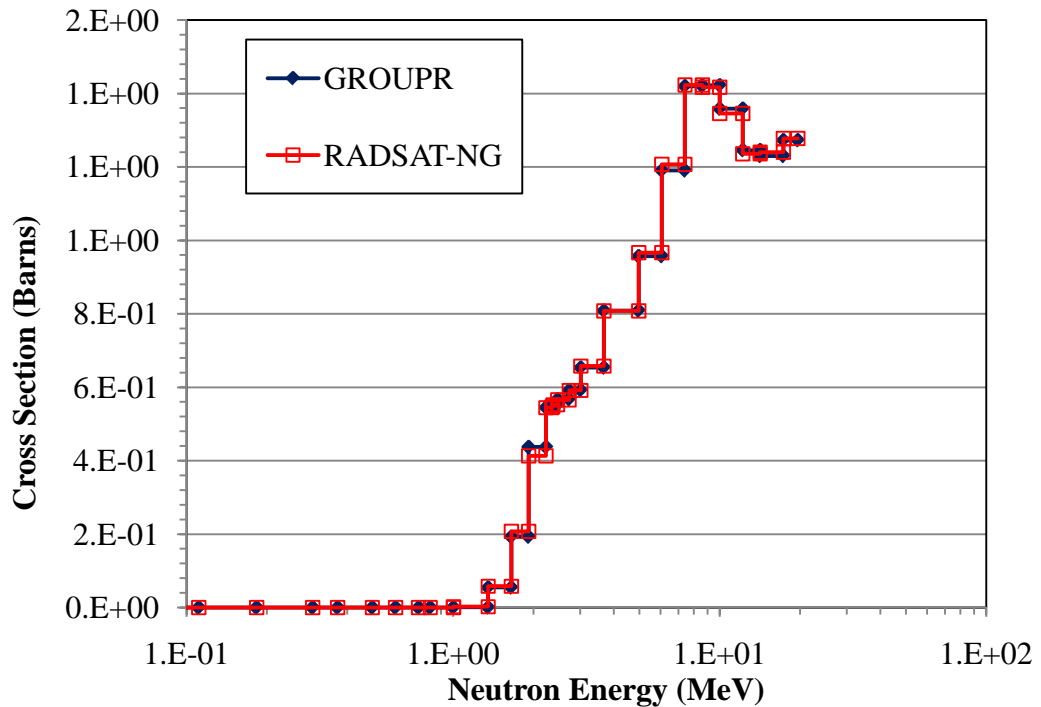
Figure 24. Comparison of Phosphorus "Nonelastic" Photon Production Cross Section for RADSAT-NG and GROUPR

Table 7. Comparison of Total Cross Section for RADSAT-NG and Cross Sections
Produced by GROUPR for Phosphorus

Cross Section	RADSAT-NG Total Cross Section (Barns)	GROUPR Total Cross Section (Barns)	Percent Difference	Group # Largest % Difference	Group # Smallest % Difference
Nonelastic Interaction	15.06	15.05	0.10%	Group #19 (7.84%)	Group #14 (5.52E-2%)
Radiative Capture	16.14	15.84	1.87%	Group #79 (7.51%)	Group #77 (2.16E-2%)

3.2.3 Photon Flux within Detector

Using the RADSAT-NG cross sections and the spatially dependent neutron flux obtained from Attila, the neutron-induced photon spectrum was calculated for the irradiation of phosphorus. Using the group generator in RADSAT, 150 continuum groups and three 0.3-keV wide peak groups were assigned, one for the 511-keV annihilation peak and the other two for the two discrete gamma rays produced by phosphorus. A $1/\sqrt{E}$ weighting factor was applied to the continuum groups which makes the continuum groups in the lower energy range finer and the continuum groups in the higher energy range broader. This group structure was used to create the photon cross-section library for the photon transport calculation.

A comparison of the volume-averaged gamma flux in the detector for MCNP and RADSAT for the irradiation of phosphorus is shown in Figure 25. The comparison of MCNP and RADSAT shows good agreement for both the continuum and the peaks. The total flux simulated using MCNP and RADSAT shows agreement to within 0.13%, and the statistical uncertainty of the MCNP simulation was 0.92%. A comparison of the 1.266 and 2.234-MeV gamma rays for MCNP and RADSAT shows typical agreement to

within 0.42 and 1.23%, respectively. The statistical uncertainty of the MCNP calculations

was 1.43 and 2.31% for those same lines and is shown in Table 8.
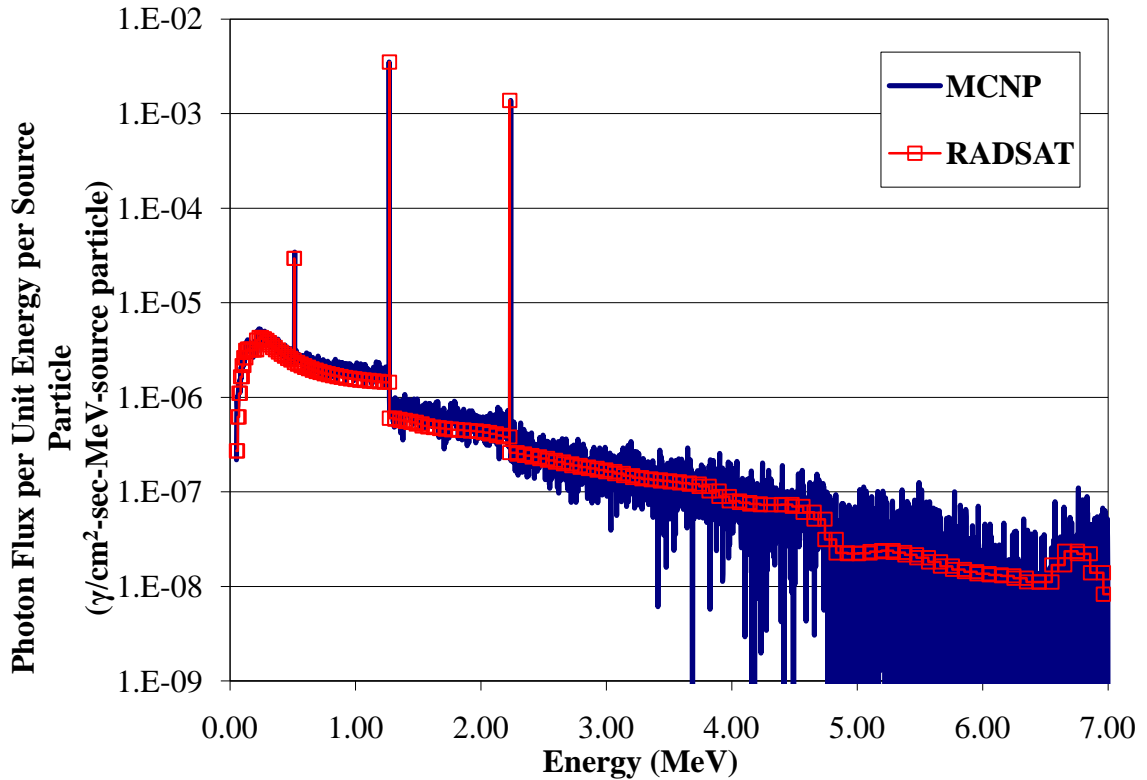
Figure 25. Code-to-Code Comparison Using RADSAT and MCNP5 of Volume-
Averaged Flux at the Detector Location for Neutron Activation Analysis of Phosphorus

Table 8. Comparison of Photon Flux for Top 2 Most Intense Peaks Produced by the
Neutron Irradiation of Phosphorus

Gamma-Ray Energy (MeV)	MCNP (γ/sec-Source Particle)	MCNP Relative Uncertainty (%)	RADSAT (γ/sec-Source Particle)	Percent Difference (%)
1.266	3.53E-06	1.43	3.52E-06	0.42
2.234	1.37E-06	2.31	1.38E-06	1.23
Total	8.48E-06	0.92	8.47E-06	0.13

3.3   Nitrogen

Nitrogen was chosen as a testing material due to its common presence in nature
and its relatively complex induced photon spectrum when compared to either
polyethylene or phosphorus. Nitrogen is one of the most abundant elements on earth. It
is present in the air, the earth's crust and many man-made substances including fertilizer,
ammonia, nitric acid, propellants (rocket fuel) and explosives. The abundance of nitrogen
in the atmosphere and the ground, in addition to being a constituent of explosives, makes
it a key element for a coupled neutron photon simulations.

3.3.1   Neutron Flux Comparison

The neutron flux comparison was completed to test the accuracy of the Kynea3
cross section for nitrogen. Since pure nitrogen is typically only present in low densities
(natural density of 0.001251 grams/cm^3 at 0°C and 0.807 grams/cm^3 at -196°C for liquid
nitrogen), an arbitrary density 0.5 grams per cubic centimeter was modeled to increase
the probability of the neutron interaction in the nitrogen.   The total neutron flux within
the nitrogen cube for Attila is within 1.25% of the MCNP simulation result and is shown
in Table 9. The Attila result was able to resolve the flux at the lower energy ranges
causing the total flux to be higher. The MCNP simulation did not obtain a neutron flux in
many of the lower energy bins. Although the MCNP statistical uncertainty for the tally is
less than 1×10^{-4}%, the statistical uncertainty for the 10-eV energy bin is 11.19%, and the
statistical uncertainty for the 5-eV energy bin and below is greater than or equal to
20.21%. A graphical comparison of the volume-averaged neutron flux within the
nitrogen cube for MCNP and Attila is shown in Figure 26. Below approximately 50-keV,
the Attila neutron flux appears to be biased. It is hypothesized that this is due to the

small number of thermal neutrons created in this problem. In order for either code to converge of the proper answer, a problem should be set up which allows for the generation of more thermal neutrons.

Table 9. Comparison of Attila and MCNP Total Neutron Flux for the Irradiation of Nitrogen

MCNP Flux (Neutron /cm^2-sec-source particle)	MCNP Statistical Uncertainty	Attila Flux (Neutron /cm^2-sec-source particle)	Percent Difference
7.67×10^{-4}	$<1 \times 10^{-4}$%	7.77×10^{-4}	1.25%
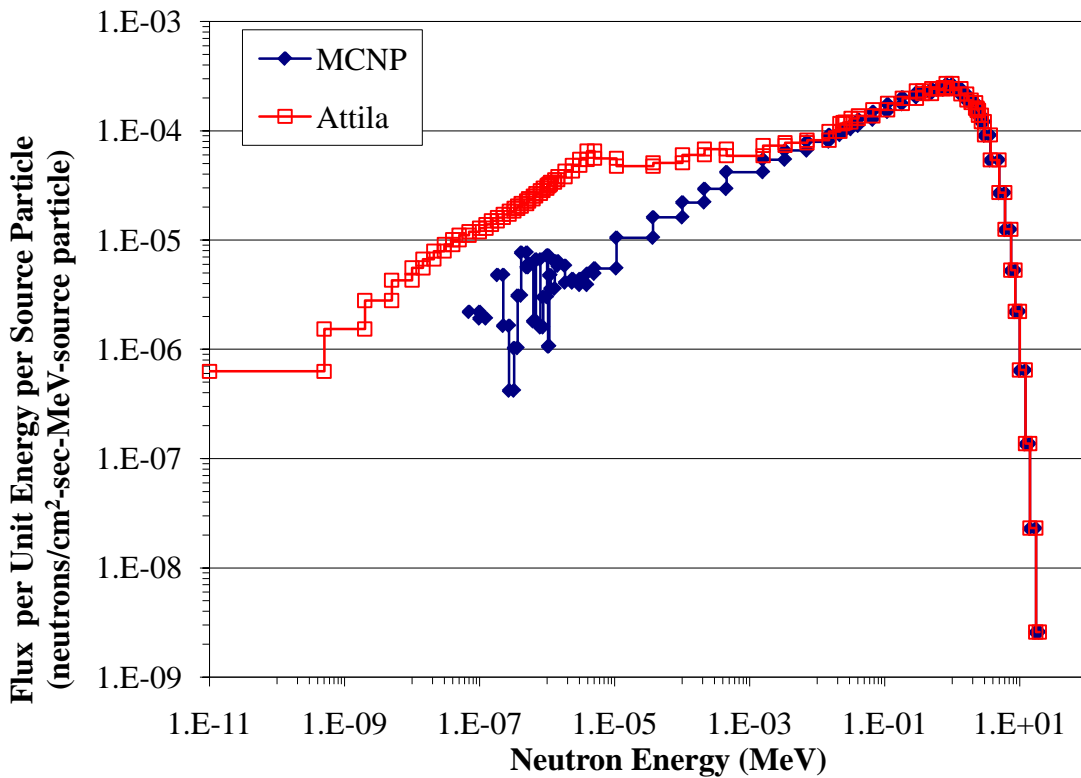
Figure 26. Comparison of Attila and MCNP Neutron Flux for the Irradiation of Nitrogen

3.3.2 Cross Sections

The multigroup cross section for nitrogen is somewhat more difficult to calculate than the phosphorus cross section data. Nitrogen has two naturally occurring isotopes ^{14}N and ^{15}N, with corresponding natural abundances of 99.634% and 0.366%. ^{14}N has eight gamma-ray producing reactions and ^{15}N has eight gamma-ray producing reactions in the neutron energy range included in the Kynea3 neutron energy group structure, none of which contain any unresolved resonances. ^{15}N produces eight continua and no discrete gamma rays, and there are a total of 136 discrete gamma-rays and one continuum produced by ^{14}N. Table 10 contains a list of the gamma producing interactions in ^{14}N and the gamma rays produced by each interaction. The ^{14}N continuum gamma rays are produced by the radiative capture cross section. The ^{14}N and ^{15}N RADSAT-NG cross sections were collapsed from the ENDF/B-VI cross section data at 300K. A comparison of the RADSAT-NG and GROUPR radiative capture cross section for ^{14}N and the (n,np) reaction in ^{15}N is shown in Figure 27 and Figure 28, respectively.

Table 10. Discrete Gamma Rays Produced by ^{14}N

Reaction	Gamma Rays (MeV)
(n,n')	0.6119201, 0.7283601, 0.9670002, 1.15779, 1.34028, 1.635302, 2.14313, 2.312799, 2.498071, 2.517631, 2.655651, 2.682731, 2.726081, 2.793093, 2.928261, 3.081021, 3.294651, 3.338001, 3.378643, 3.384011, 3.480811, 3.890703, 3.948101, 4.018801, 4.365831, 4.671601, 4.716323, 4.915101, 5.105891, 5.691441, 5.834251, 6.203501, 6.446171, 6.859454, 7.029122, 7.966902, 8.062002, 8.619702, 8.776002, 9.128902, 9.172252, 10.432, 11.05
(n,np)	0.1693, 0.5951001, 0.7644001, 3.089401, 3.684501, 3.853801
(n,nd)	4.438911
(n,γ)	0.1314, 0.383, 0.5838, 0.6083, 0.7678, 0.7704, 0.8312, 0.9084, 1.0117, 1.0252, 1.0539, 1.073, 1.6108, 1.6783, 1.6812, 1.7836, 1.854, 1.8848, 1.9885, 1.9997, 2.0023, 2.0308, 2.2474, 2.2618, 2.2932, 2.5204, 2.726, 2.8308, 2.8984, 3.0136, 3.2692, 3.3007, 3.532, 3.6777, 3.8556, 3.8809, 3.8842, 3.9239, 4.5087, 4.6541, 5.2692, 5.2978, 5.5334, 5.5621, 6.3224, 7.1534, 7.299, 8.3102, 8.5686, 9.0467, 9.149, 9.1519, 9.2195, 9.7571, 9.9213, 10.0619, 10.6978, 10.83291
(n,p)	0.4956001, 0.6132001, 0.6344001, 0.8088001, 0.9182001, 1.2476, 6.093801, 6.589401, 6.728202, 7.012002, 7.341402
(n,d)	0.1693, 0.5951001, 0.7644001, 3.089401, 3.684501, 3.853801
(n,t)	4.438911
(n, α)	1.77149, 2.12469, 2.265201, 2.298011, 2.442101, 2.840621, 2.895621, 3.539991, 4.115411, 4.444891, 4.475311, 4.667111, 4.740111, 5.020311, 5.853151, 6.435611, 6.742902, 6.791802, 7.285512, 7.977842, 8.560302, 8.920202, 9.185002
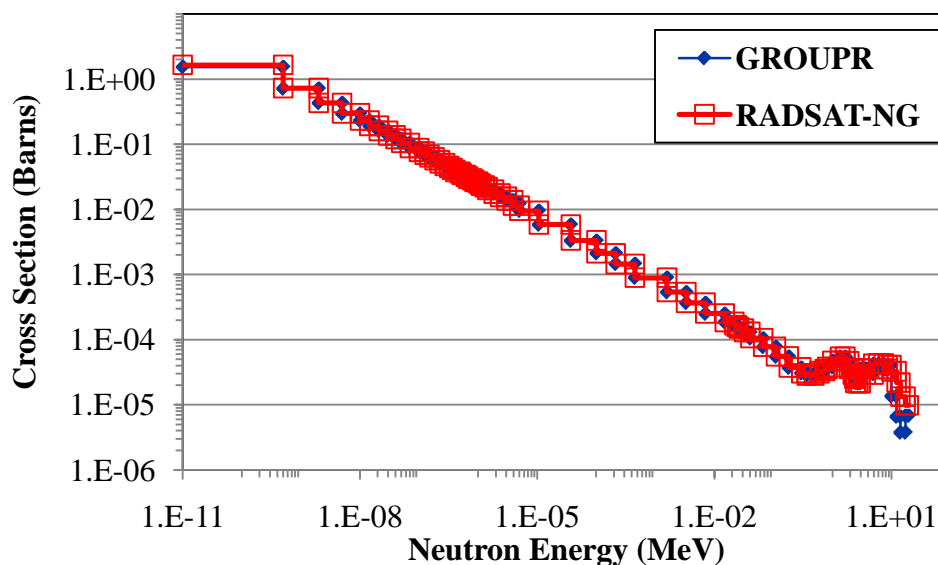
Figure 27. Comparison of ^{14}N Radiative Capture Photon Production Cross Section for RADSAT-NG and GROUPR
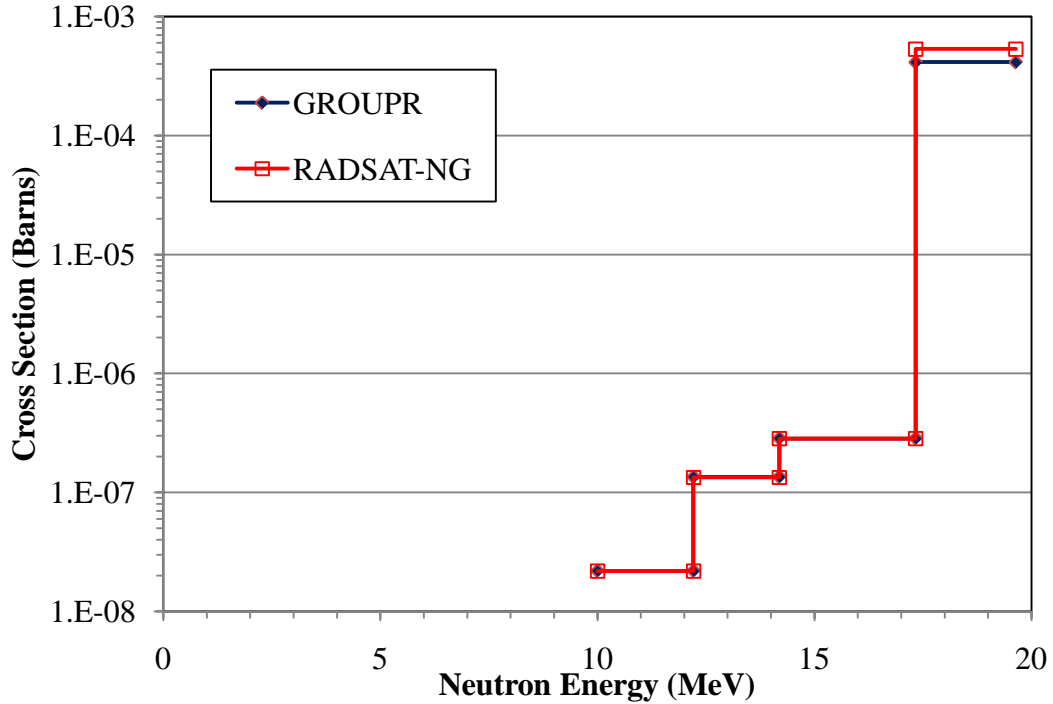
Figure 28. Comparison of ^{15}N (n,np) Photon Production Cross Section for RADSAT-NG and GROUPR

The nitrogen RADSAT-NG and GROUPR collapsed nitrogen cross sections agree reasonably well. The comparison of the total RADSAT-NG ^{15}N (n,np) cross section is within 28.82% of the GROUPR collapsed cross section. The large percent difference for this cross section is due to the difference in the cross section in highest energy group, 5.39×10^{-4} for RADSAT-NG and 4.13×10^{-4} for GROUPR which accounts for 99.893% of the total cross section. For the ^{14}N radiative capture cross section, there is a discrepancy in the cross section between the four highest energy groups when comparing the RADSAT-NG cross to the GROUPR collapsed cross section. The energy-dependent RADSAT-NG radiative capture cross section for ^{14}N is compared to the GROUPR collapsed cross section and the energy-dependent ACER cross section for the same interaction in Figure 29 to examine this discrepancy against the energy-dependent cross

section data. For the region between 10 and 19.6-MeV (neutron energy groups 1 thru 4), it appears that the RADSAT-NG cross section more accurately represents the pointwise data. This discrepancy is the main source of the 2.62% difference in the ^{14}N radiative capture cross section when comparing the cross section produced by GROUPR and RADSAT-NG.
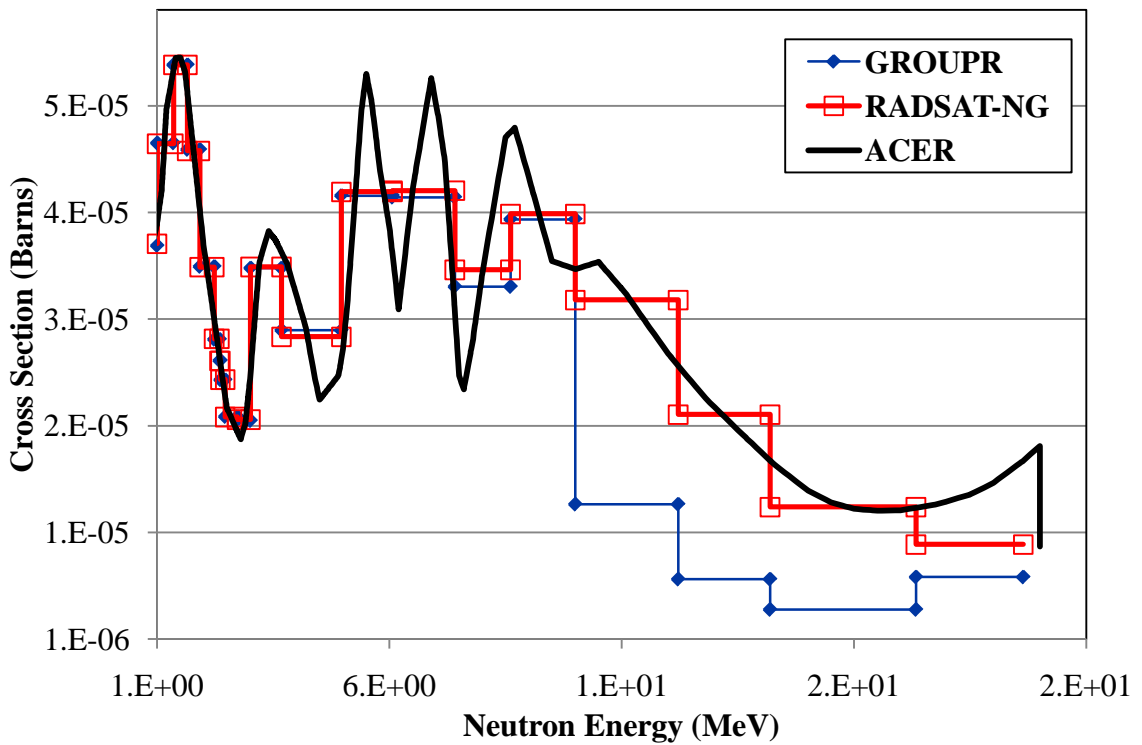
Figure 29. Comparison of Energy-dependent ^{14}N Radiative Capture Photon Production Cross Section for RADSAT-NG, GROUPR and ACER

Table 11 contains a comparison of the total for each of the gamma-ray producing cross sections for ^{14}N and ^{15}N for RADSAT-NG and GROUPR and the percent difference for the two. All of the ^{14}N RADSAT-NG cross sections are within 1.5% of the GROUPR cross sections except for the radiative capture cross section. The comparison

of the ^{15}N RADSAT-NG cross sections to the GROUPR cross section was not as close as

the ^{14}N comparison. All but one of the ^{15}N RADSAT-NG cross sections were within 5%

of the GROUPR cross sections. The ^{15}N (n,np) total RADSAT-NG cross section differs

from GROUPR by 28.82%. Although the ^{15}N (n,np) cross section spans four energy

groups, the highest energy group composes 99.17% of the total cross section for the

interaction. The RADSAT-NG cross section in the highest energy neutron group was

larger than the GROUPR collapsed cross section by 28.82%. As previously noted, there

is a known difference in the handling of RADSAT-NG and GROUPR cross sections in

the highest and lowest energy groups which has been documented but is still under

investigation.

Table 11. Comparison of Total Cross Section for RADSAT-NG and Cross Sections
Produced by GROUPR for ^{14}N

Cross Section	RADSAT-NG Total Cross Section (Barns)	GROUPR Total Cross Section (Barns)	Percent Difference (%)
^{14}N (n,n')	2.0093	2.0270	0.87
^{14}N (n,np)	0.1478	0.1480	0.19
^{14}N (n,nd)	0.0256	0.0257	0.11
^{14}N (n,γ)	5.0332	4.9037	2.64
^{14}N (n,p)	0.2563	0.2579	0.62
^{14}N (n,d)	0.0951	0.0953	0.27
^{14}N (n,t)	0.0668	0.0677	1.43
^{14}N (n, α)	0.5969	0.6004	0.57
^{15}N (n,n')	3.9162	3.9123	0.10
^{15}N (n,2n)	0.0295	0.0283	4.31
^{15}N (n, nα)	0.0209	0.0200	4.65
^{15}N (n, np)	0.0005	0.0004	28.82
^{15}N (n,p)	0.0325	0.0326	0.37
^{15}N (n,d)	0.0290	0.0283	0.89
^{15}N (n,t)	0.0315	0.0346	1.65
^{15}N (n,α)	0.1899	0.1914	0.80

3.3.3 Photon Flux within Detector

Once the induced photon spectrum was calculated for the neutron irradiation of nitrogen using the RADSAT-NG cross sections and the spatially dependent neutron flux obtained from Attila, the RADSAT group generator was used to produced the specialized photon group structure. 166 continuum groups and 133 0.3-keV wide peak groups were assigned using the group generator, one for the 511-keV annihilation peak and the remaining peak groups 165 most intense gamma rays produced by ^{14}N. A $1/\sqrt{E}$ energy weighting factor was applied to the continuum groups. This group structure was used to create the photon cross-section library for the photon transport calculation.

A comparison of the volume-averaged gamma flux in the detector for MCNP and RADSAT is shown in Figure 30. A comparison of the 5 highest intensity gamma rays for MCNP and RADSAT show typical agreement to within 3%, with the statistical uncertainty of the MCNP calculations generally greater than 4% for those same lines and is shown in Table 12. The nitrogen test case indicates that the RADSAT-NG cross-section creation methods are adequately collapsing and compiling the many cross-sections needed for more complex neutron activation isotopes.
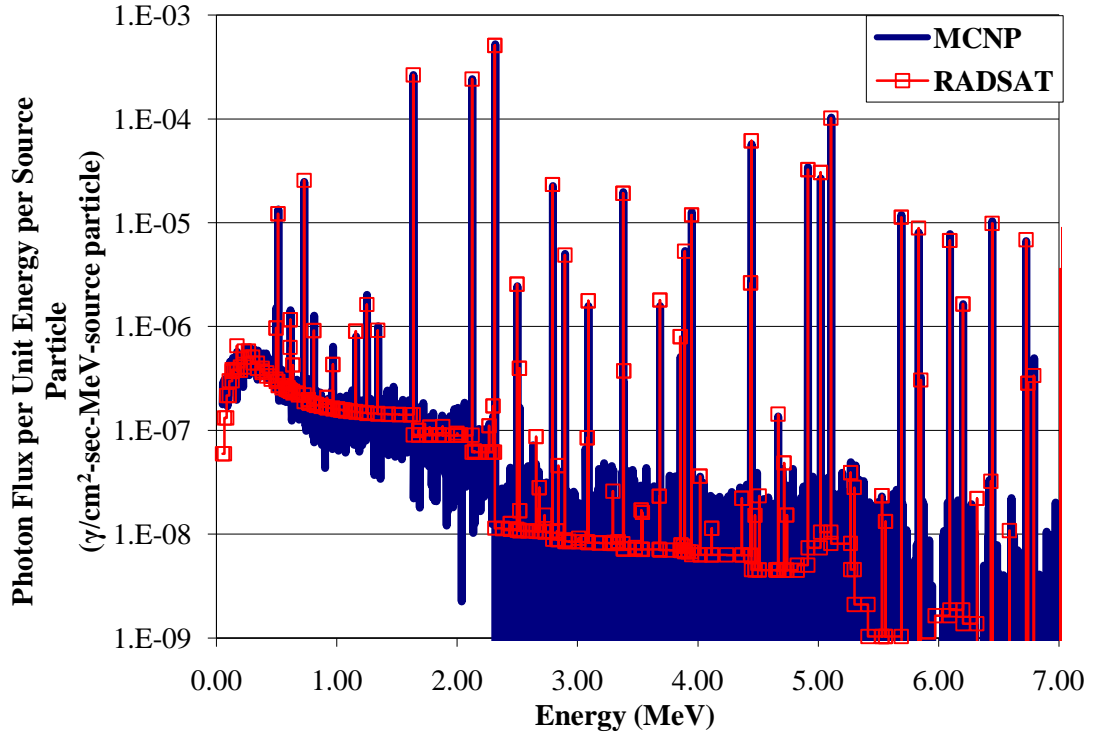
Figure 30. Comparison of Volume-Averaged Photon Flux in Detector using RADSAT and MCNP for Nitrogen

Table 12. Comparison of Photon Flux for Top 5 Most Intense Peaks Produced by the Neutron Irradiation of Nitrogen

Gamma-Ray Energy (MeV)	MCNP (γ/cm^2-sec-source particle)	MCNP Relative Uncertainty (%)	RADSAT (γ/cm^2-sec-source particle)	Percent Difference (%)
1.635302	2.65E-07	4.38	2.64E-07	0.38
2.12469	5.23E-07	4.59	5.06E-07	3.23
2.312799	5.23E-07	3.15	5.08E-07	2.87
4.444891	5.73E-08	9.65	5.56E-08	2.90
5.105891	1.03E-07	6.62	1.01E-07	1.94
Total	1.86E-06	1.65	1.82E-06	2.17

3.4   Oxygen

Oxygen, like nitrogen, is very common in nature, and the induced photon

spectrum for the neutron irradiation of oxygen is approximately the same level of

complexity as nitrogen. Oxygen, also like nitrogen, is one of the most abundant elements

85

on Earth. It composes a larger fraction of the Earth's crust and oceans than nitrogen but a smaller percentage of the air. Oxygen is used for many applications including torches, rocket propellants, chemical weapons, medicine, antifreeze, plastics and fabrics. Due to oxygen's wide range of applications and abundance on Earth, many applications may benefit from the addition of the inclusion of oxygen in the RADSAT-NG photon production cross sections in the library.

3.4.1 Neutron Flux Comparison

The first step in completing the coupled neutron-photon calculation was to complete the neutron transport calculation for oxygen. An arbitrary density 0.5 grams per cubic centimeter was modeled to increase the probability of the neutron interaction in the oxygen since pure oxygen is typically only present in low densities (natural density of 0.001429 grams/cm^3 at 0°C [31]). The total neutron flux within the oxygen cube for Attila is within 1.69% of the MCNP simulation result and is shown in Table 13. Unlike the Attila simulation which provides an infinite time solution, the MCNP result does not obtain counts in many of the lower energy bins even though the statistical uncertainty for the overall tally is less than $1x10^{-4}$%. The statistical uncertainty for the 10-eV energy bin is 17.83%, and the statistical uncertainty for the 5-eV energy bin and below is greater than or equal to 29.65%. Only two of the energy bins below 0.145-eV registered any counts at all. A comparison of the volume-averaged neutron flux within the entire oxygen cube obtained from MCNP and Attila using the Kynea3 cross section library is shown in Figure 31. Although the statistical uncertainly below 50-kev is relatively poor on the MCNP calculation, the Attila calculation exhibits a substantial bias. Determining the origin of this bias remains outside of the scope of this body of work, but it is believed

that the bias is caused by a lack of thermalization of neutrons to this region.   Adjusting

the density of the problem or the target material to a mixture of poly and oxygen may

remedy this bias.

Table 13. Comparison of Attila and MCNP Total Neutron Flux for the Irradiation of Oxygen

MCNP Flux (Neutron /cm^2-sec-source particle)	MCNP Statistical Uncertainty (%)	Attila Flux (Neutron /cm^2-sec-source particle)	Percent Difference (%)
8.21×10^{-4}	$<1 \times 10^{-4}$	$8.34E \times 10^{-4}$	1.69
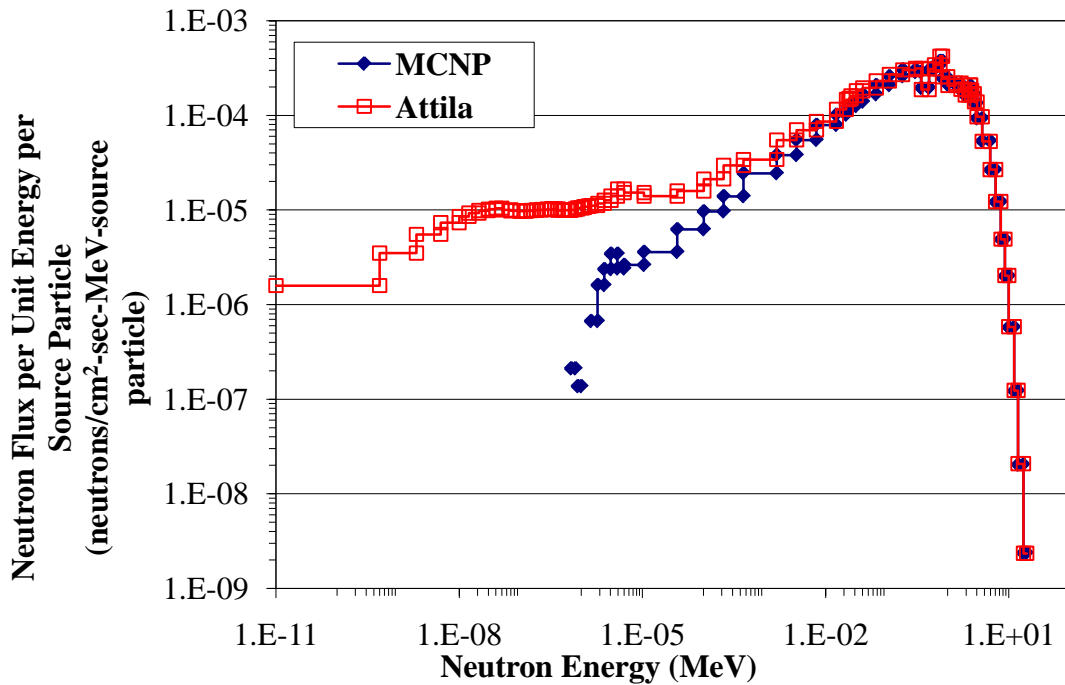
Figure 31. Comparison of Attila and MCNP Neutron Flux for the Irradiation of Oxygen

3.4.2 Cross Sections

The cross section for oxygen is similar to that of nitrogen in that it does not contain any unresolved resonance features. Oxygen is composed of three naturally occurring isotopes ^{16}O, ^{17}O and ^{18}O (99.762%, 0.038% and 0.2% respectively). There is no neutron cross section for ^{18}O, so it will not be included in these calculations. Additionally, the ENDF/B-VI cross section for ^{17}O does not contain any photon production cross section data. Thus, the only isotope of oxygen used for the photon production calculations is ^{16}O. ^{16}O has eight gamma-ray producing reactions in the neutron energy range included in the Kynea3 neutron energy group structure, producing a total of 51 discrete and 4 continua gamma rays. A list of the gamma-ray producing interactions in ^{16}O and the gamma rays produced by each interaction is shown in Table 14. The ^{16}O RADSAT-NG cross sections were collapsed from the ENDF/B-VI cross section data at 300K. A comparison of the RADSAT-NG and GROUPR radiative capture and (n,α) cross sections for ^{16}O are shown in Figure 32 and Figure 33, respectively.

Table 14. Discrete Gamma Rays Produced by ^{16}O

Reaction	Gamma Ray Energy (MeV)
(n,n')	0.51, 0.8677, 0.986957, 1.75505, 1.9548, 2.2081, 2.742007, 2.8225, 3.84015, 4.1629, 4.950107, 6.129893, 6.9171, 7.11685, 8.8719
(n,nα)	4.438
(n,γ)	0.8708, 1.088, 2.1842, 3.2722
(n,p)	0.1201, 0.2774, 0.297, 0.3975
(n,d)	1.0117, 1.1577, 1.4163, 1.885, 1.9889, 2.0023, 2.031, 2.2475, 2.297, 3.014, 3.3013, 5.2701, 5.2988, 6.3239, 7.3011, 7.5671, 8.3128, 8.5714
(n,t)	1.635302, 2.312798, 3.9481
(n,α)	0.1693, 0.5951, 0.7644, 3.0894, 3.6845, 3.8538
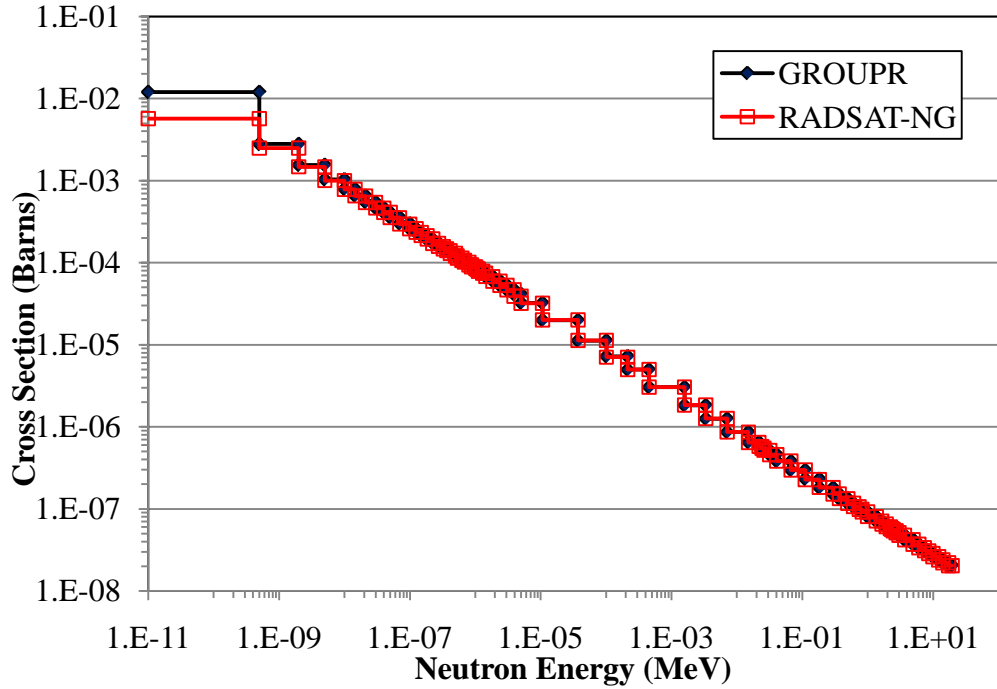
Figure 32. Comparison of the GROUPR and RADSAT-NG ^{16}O Radiative Capture
Photon Production Cross Section
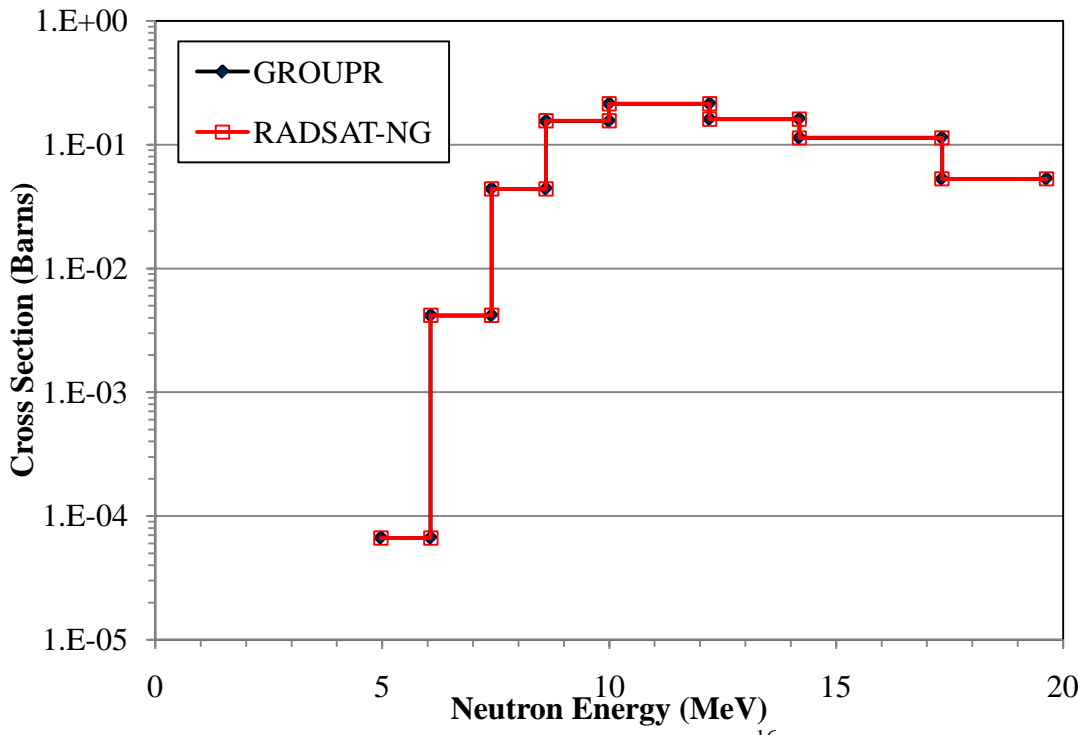
Figure 33. Comparison of the GROUPR and RADSAT-NG ^{16}O (n,α) Photon Production
Cross Section

The comparison of the RADSAT-NG cross sections and the cross sections collapsed using GROUPR shows reasonably good agreement for ^{16}O as shown in Table 17. The difference in ^{16}O radiative capture cross section is due to a difference in the lowest energy group. The RADSAT-NG radiative capture cross section for the lowest energy group is a factor of 2 lower than the GROUPR collapsed cross section. The remainder of the cross section agreed with the GROUPR collapsed cross section.

The large percent difference of 19.96% for the (n,n3α) cross section is due to the fact that the cross section is present in only one energy bin. The RADSAT-NG and GROUPR method rarely calculate the same value for the lowest and highest cross section bins, so when a cross section relies on the calculation of only one bin the codes do not agree. The reason for this discrepancy is still under investigation. The RADSAT-NG cross section library calculates a cross section in a second energy bin, but its value is 10 orders of magnitude smaller than the cross section in highest neutron energy group which is believed to be below the minimum cross section value calculated by GROUPR. A similar scenario is true for the (n,np) cross section which would account for the 6.93% difference in the RADSAT-NG and GROUPR cross sections.

The (n,2α) cross section was not collapsed by GROUPR at all even though the cross section is present in the Kynea3 energy range. A comparison of the continuous energy ACER photon production cross section to the RADSAT-NG photon production cross section for the (n, 2α) reaction is shown in Figure 34. It is hypothesized that GROUPR did not collapse this particular reaction due to the small magnitude of the cross section.

Table 15. Comparison of Total Cross Section for RADSAT-NG and Cross Sections
Produced by GROUPR for ^{16}O

Cross Section	RADSAT-NG Total Cross Section (Barns)	GROUPR Total Cross Section (Barns)	Percent Difference (%)
^{16}O (n,n')	2.39E+00	2.39E+00	0.04
^{16}O (n,nα)	1.96E-01	1.95E-01	0.16
^{16}O (n,n3α)	5.70E-08	4.75E-08	19.96
^{16}O (n,np)	4.13E-05	3.86E-05	6.93
^{16}O (n,γ)	1.71E-02	2.39E-02	28.35
^{16}O (n,p)	1.29E-01	1.29E-01	0.07
^{16}O (n,d)	1.85E-02	1.85E-02	0.50
^{16}O (n,t)	6.65E-04	6.36E-04	4.47
^{16}O (n,α)	7.44E-01	7.44E-01	0.02
^{16}O (n,2α)	1.37E-13	0.00E+00	N/A
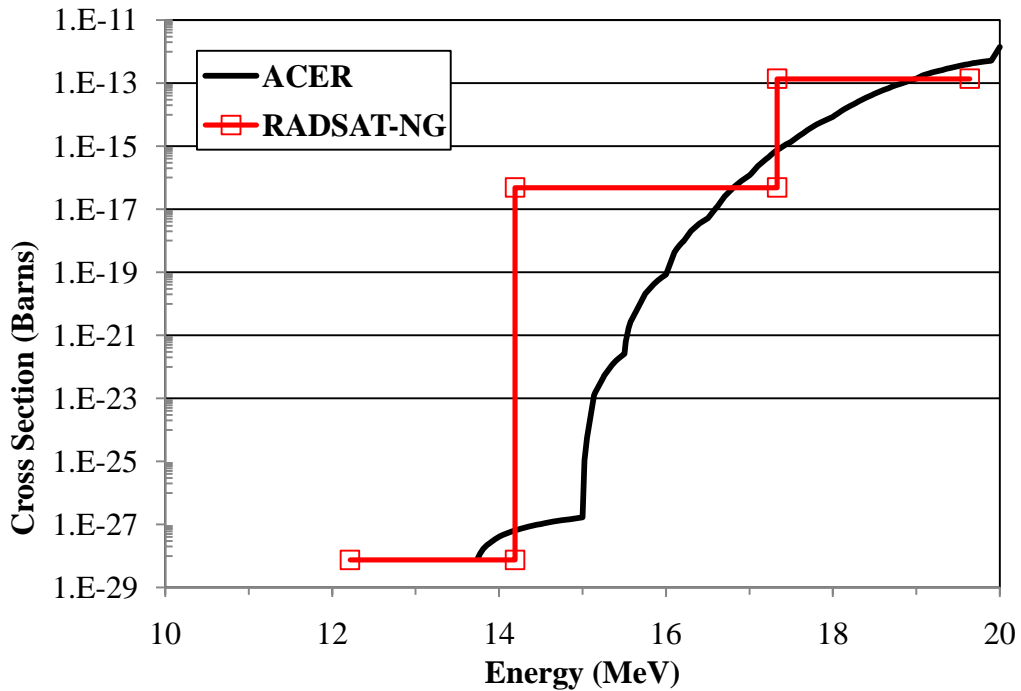
Figure 34. Comparison of Energy-dependent ^{16}O (n,2α) Photon Production Cross Section
for RADSAT-NG, GROUPR and ACER

3.4.3 Photon Flux within Detector

Using the RADSAT-NG cross sections and the spatially dependent neutron flux obtained from Attila, the induced photon spectrum was calculated for the neutron irradiation of oxygen. The RADSAT group generator then was used to produce the specialized photon group structure containing 248 continuum groups and 52 0.3-keV wide groups, one for the 511-keV annihilation peak and for the remaining groups 51 most intense gamma rays produced by ^{16}O using a $\mathbf{1/\sqrt{E}}$ energy weighting factor for the continuum energy groups.

The volume-averaged gamma flux in the detector from the neutron irradiation of oxygen calculated using the RADSAT method agrees well with the results obtained from the MCNP simulation as shown in Figure 35. The total photon flux within the detector is within 6.4% of the MCNP result. The 0.511-MeV annihilation line is underestimated using the RADSAT method, and the continuum region below the 0.511-MeV line does not quite obtain the same shape as the MCNP simulation. The 5 most intense gamma rays for MCNP and RADSAT show typical agreement to within 3%. The statistical uncertainty of the MCNP simulation for the same gamma ray emissions is equal to or greater than the percent difference between the MCNP and RADSAT calculations as shown in Table 16.

Figure 35. Comparison of Volume-Averaged Photon Flux in Detector using RADSAT and MCNP for Oxygen

Table 16. Comparison of Photon Flux for Top 6 Most Intense Peaks Produced by the Neutron Irradiation of Oxygen

Gamma-Ray Energy (MeV)	MCNP (γ/cm^2-sec-source particle)	MCNP Relative Uncertainty (%)	RADSAT (γ/cm^2-sec-source particle)	Percent Difference (%)
2.742007	1.22E-09	9.68	1.28E-09	5.26
3.0894	3.98E-09	5.10	3.88E-09	2.38
3.6845	8.70E-09	3.24	8.53E-09	2.03
3.8538	3.60E-09	5.35	3.35E-09	0.41
6.129893	5.84E-08	1.25	5.85E-08	0.15
6.9171	9.34E-09	3.31	8.62E-09	3.37
Total	1.46E-07	0.90	1.55E-07	6.40

3.5   Iron

Iron was selected as a benchmarking material due to its common presence in many common applications. Iron is the main material component of steel. Also, iron is commonly used as a structural component for buildings, cars, planes, ships, office supplies, and computers. Many of these items could be exposed to neutron fields, so understand the neutron-induced photon spectrum is important to many detector scenarios.

3.5.1   Neutron Flux Comparison

The neutron flux comparison was completed to test the accuracy of the Kynea3 cross section for iron. The iron was modeled at 7.874 grams/cm^3 which is the natural density of iron at 300 K [31]. The total neutron flux within the iron cube for Attila is within 1.25% of the MCNP simulation result and is shown in Table 17. The Attila was able to resolve the flux at the lower energy ranges causing the total flux to be higher than the flux obtained by MCNP since it did not obtain any counts in the lower energy bins at all. Although the MCNP statistical uncertainty for the tally is less than $1x10^{-4}$%, the statistical uncertainty for the 37.3-eV energy bin is 8.49%, and the statistical uncertainty for the 5-eV energy bin and below is greater than or equal to 38.52%. A graphical comparison of the volume-averaged neutron flux within the nitrogen cube for MCNP and Attila is shown in Figure 36. As with the other neutron transport calculations that do not contain many thermal neutrons, the Attila calculation exhibits a systematic bias below 50-keV when compared to MCNP for the neutron flux.

Table 17. Comparison of Attila and MCNP Total Neutron Flux for the Irradiation of Iron

MCNP Flux (Neutron /cm²-sec-source particle)	MCNP Statistical Error (%)	Attila Flux (Neutron /cm²-sec-source particle)	Percent Difference (%)
7.60×10^{-4}	$>1 \times 10^{-4}\%$	7.77×10^{-4}	1.25%
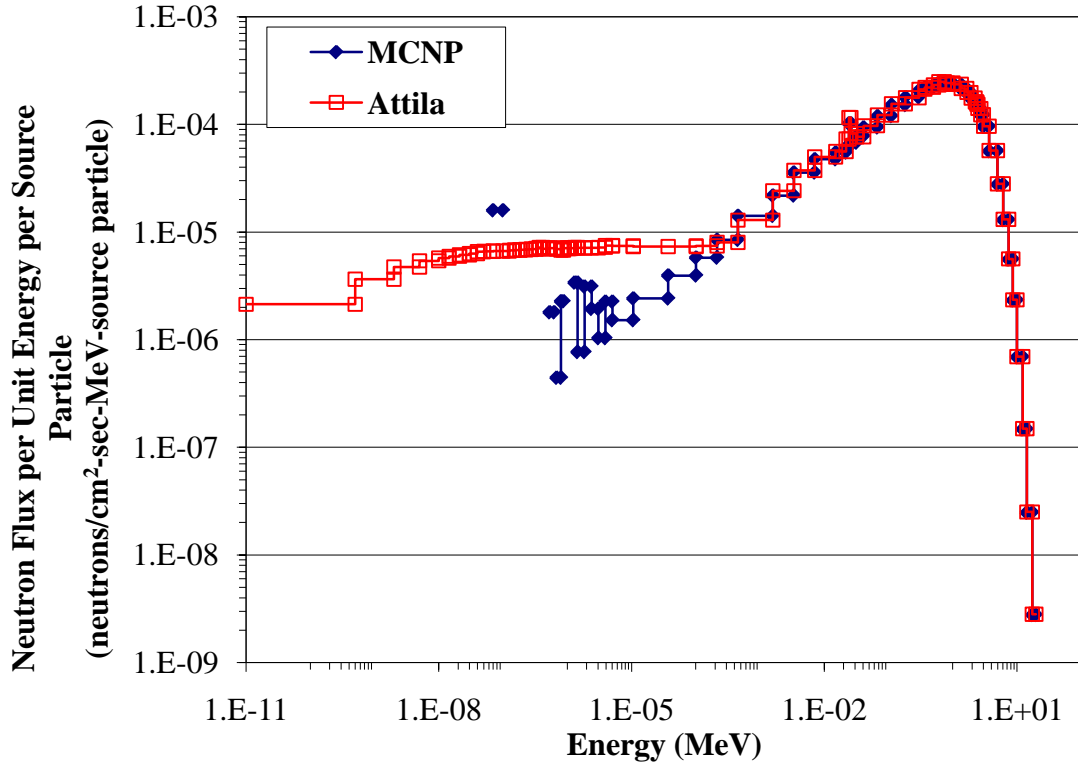
Figure 36. Comparison of Attila and MCNP Neutron Flux for the Irradiation of Iron

3.5.2 Cross Sections

Although the ENDF/B-VI cross sections for iron do not contain any unresolved

resonances, they do contain resolved resonances making them the most difficult cross

sections in this document to collapse. Iron has four naturally occurring isotopes ^{54}Fe,

^{56}Fe, ^{57}Fe and ^{58}Fe, with corresponding natural abundances of 5.8%, 91.72%, 2.2% and

0.28%. Unfortunately the GROUPR subroutine produces an energy grid error when

95

collapsing ^{57}Fe, so the comparison of the RADSAT-NG and GROUPR cross sections for ^{57}Fe has been omitted. ^{54}Fe has 7 gamma producing reactions which result in 52 discrete gamma rays and 7 continua; ^{56}Fe has 7 gamma producing reactions which create in 308 discrete gamma rays and 7 continua; ^{57}Fe has 7 gamma producing reactions which create in 112 discrete gamma rays and 7 continua; and ^{58}Fe has 14 gamma producing reactions resulting in 143 discrete gamma rays and 7 continua. Table 18 contains a list of the gamma producing interactions in iron and the gamma rays produced by each interaction. The ^{54}Fe, ^{56}Fe and ^{58}Fe RADSAT-NG cross sections were collapsed from the ENDF/B-VI cross section data at 300K. A comparison of the RADSAT-NG and GROUPR radiative capture cross sections for ^{54}Fe, ^{56}Fe and ^{58}Fe are shown in Figure 37, Figure 38, and Figure 39, respectively.
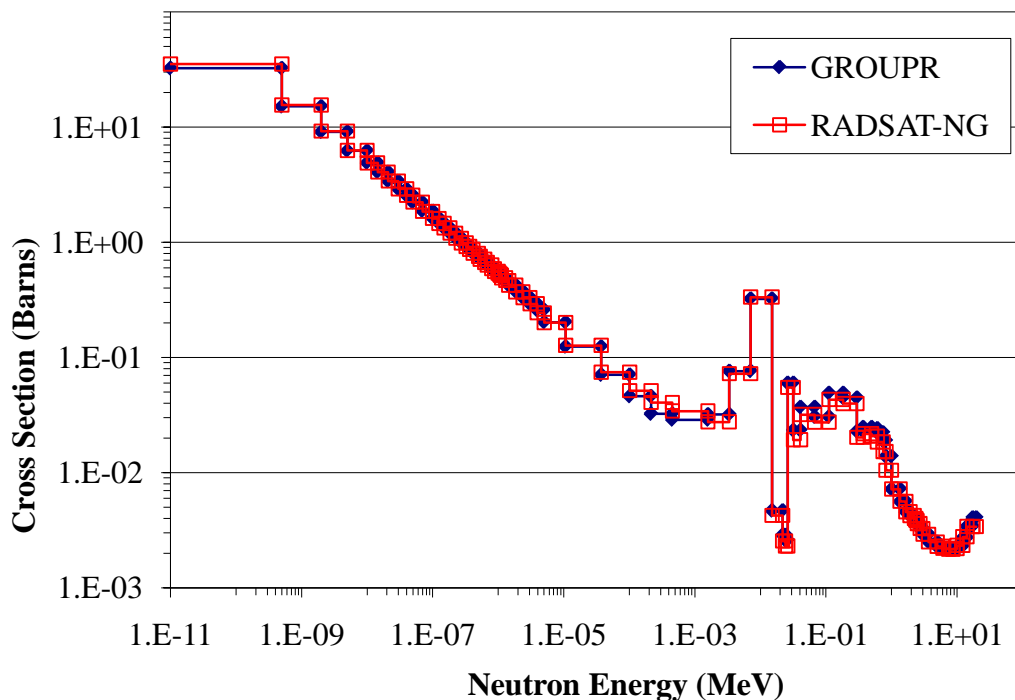
Figure 37. Comparison of the GROUPR and RADSAT-NG ^{54}Fe Radiative Capture Photon Production Cross Section

Table 18. Discrete Gamma Rays Produced by Iron

Isotope	Reaction	Gamma Rays (MeV)
^{54}Fe	(n,n')	0.412, 0.757, 1.13, 1.153, 1.408, 1.551, 1.758, 1.887, 2.959, 3.166
^{54}Fe	(n,γ)	9.2978, 8.8864, 7.385, 7.363, 7.2463, 6.8268, 6.617, 6.2689, 5.7454, 5.5075, 5.3911, 4.8028, 4.707, 4.5896, 4.535, 4.495, 4.455, 4.18, 4.012, 3.96, 3.906, 3.792, 3.552, 3.508, 3.38, 3.04, 3.028, 3.005, 2.873, 2.791, 2.67, 2.618, 2.47, 2.052, 1.918, 1.872, 1.638, 1.506, 1.315, 1.24, 0.931, 0.412
^{56}Fe	(n,n')	0.368, 0.734, 0.787, 0.847, 0.952, 0.977, 1.038, 1.061, 1.089, 1.14, 1.16, 1.174, 1.175, 1.238, 1.272, 1.303, 1.335, 1.36, 1.442, 1.459, 1.462, 1.64, 1.671, 1.772, 1.811, 1.852, 1.964, 2.015, 2.035, 2.095, 2.113, 2.273, 2.373, 2.425, 2.523, 2.598, 2.602, 2.658, 2.755, 2.76, 2.96, 2.985, 3.01, 3.202, 3.253, 3.273, 3.37, 3.449, 3.451, 3.455, 3.548, 3.554, 3.602, 3.611, 3.663, 3.832
^{56}Fe	(n,γ)	7.6456, 7.6312, 7.2788, 7.199, 6.742, 6.7174, 6.5485, 6.3805, 6.2764, 6.2194, 6.1293, 6.1021, 6.0184, 5.992, 5.9204, 5.9014, 5.7849, 5.7306, 5.3258, 5.318, 5.1797, 5.0474, 5.0421, 4.9483, 4.914, 4.8566, 4.8455, 4.84, 4.8256, 4.8098, 4.724, 4.687, 4.6751, 4.6593, 4.5974, 4.5555, 4.4625, 4.4182, 4.4057, 4.3783, 4.3238, 4.2745, 4.218, 4.2102, 4.1948, 4.0733, 3.991, 3.9817, 3.9553, 3.9215, 3.854, 3.8424, 3.7766, 3.7236, 3.7109, 3.6894, 3.663, 3.649, 3.6413, 3.6102, 3.5086, 3.5045, 3.4364, 3.4129, 3.3563, 3.2911, 3.267, 3.2393, 3.2253, 3.186, 3.1669, 3.1031, 3.0751, 3.0609, 3.0479, 3.0276, 3.0147, 2.9703, 2.954, 2.9502, 2.9434, 2.9358, 2.8737, 2.8354, 2.8325, 2.8215, 2.815, 2.7559, 2.753, 2.7342, 2.7212, 2.7046, 2.6966, 2.6916, 2.6825, 2.6543, 2.6189, 2.6031, 2.5981, 2.582, 2.5743, 2.5624, 2.5371, 2.534, 2.5262, 2.517, 2.5072, 2.4908, 2.486, 2.4802, 2.466, 2.4621, 2.4243, 2.4151, 2.4074, 2.3918, 2.3853, 2.3517, 2.3489, 2.246, 2.2162, 2.2068, 2.2027, 2.1982, 2.1928, 2.1866, 2.1647, 2.1515, 2.1386, 2.1295, 2.1134, 2.1045, 2.1013, 2.097, 2.0919, 2.0812, 2.0689, 2.0662, 2.0457, 2.0397, 2.0332, 1.991, 1.987, 1.9821, 1.9764, 1.9734, 1.9653, 1.9431, 1.9318, 1.9276, 1.8995, 1.8559, 1.8513, 1.8419, 1.8364, 1.8289, 1.8259, 1.8129, 1.8105, 1.8023, , 1.7601, 1.7253, 1.7224, 1.7172, 1.7102, 1.705, 1.7008, 1.6973, 1.691, 1.6746, 1.6721, 1.6555, 1.646, 1.627, 1.6128, 1.5846, 1.506, 1.4924, 1.4872, 1.4609, 1.4574, 1.447, 1.4356, 1.4302, 1.412, 1.3817, 1.3716, 1.3691, 1.3587, 1.3556, 1.3518, 1.3452, 1.3055, 1.3009, 1.284, 1.2823, 1.2633, 1.2606, 1.2555, 1.251, 1.2186, 1.2154, 1.1973, 1.186, 1.1595, 1.1198, 1.1156, 1.1109, 1.0773, 1.0439, 1.0411, 1.0264, 1.022, 1.019, 1.0069, 0.9918, 0.9882, 0.9771, 0.942, 0.92085, 0.89828, 0.88478, 0.87075, 0.8495, 0.8379, 0.83491, 0.8186, 0.80309, 0.7494, 0.74731, 0.7351, 0.723, 0.7064, 0.7034, 0.69203, 0.65756, 0.60354, 0.6013, 0.59863, 0.57509, 0.56992, 0.56419, 0.4601, 0.36675, 0.35236, 0.33954, 0.3359, 0.2511, 0.23029, 0.21187, 0.13652, 0.12208

Table 18 (continued).

| ⁵⁷Fe	(n,n')	0.993, 0.87, 0.706, 0.692, 0.64, 0.569, 0.367, 0.353, 0.339, 0.23, 0.137, 0.123, 0.014
⁵⁷Fe	(n,γ)	10.0441, 9.2337, 8.3697, 7.2622, 7.163, 6.9607, 6.84, 6.5064, 6.4143, 6.1631, 6.0287, 5.9056, 5.89, 5.747, 5.7218, 5.6916, 5.6002, 5.4939, 5.241, 5.223, 5.212, 5.092, 5.044, 5.001, 4.889, 4.8239, 4.789, 4.7498, 4.712, 4.6265, 4.592, 4.521, 4.506, 4.483, 4.443, 4.411, 4.38, 4.342, 4.3221, 4.2981, 4.189, 4.185, 4.1399, 4.08, 4.062, 4.006, 3.987, 3.952, 3.8818, 3.74, 3.54, 3.486, 3.326, 3.28, 3.205, 3.183, 3.162, 3.071, 2.876, 2.82, 2.781, 2.726, 2.5135, 2.4906, 2.4669, 2.4335, 2.2733, 2.1376, 2.0655, 1.971, 1.8625, 1.6742, 1.6625, 1.6572, 1.4677, 1.4463, 1.3225, 1.306, 1.2927, 1.269, 1.2668, 1.2602, 1.2507, 1.2387, 1.1646, 1.1073, 1.0974, 0.8982, 0.8636, 0.8544, 0.8105, 0.5247, 0.4593, 0.4109, 0.2781, 0.2526, 0.2431, 0.2387, 0.2336
⁵⁸Fe	(n,n')	0.811, 0.864, 1.675
⁵⁸Fe	(n,γ)	6.5809, 6.2936, 6.2284, 6.1044, 6.097, 6.0127, 5.8542, 5.6722, 5.6117, 5.5739, 5.5653, 5.4195, 5.3833, 5.3754, 5.3691, 5.2043, 5.136, 5.0092, 4.9232, 4.7638, 4.7578, 4.7295, 4.6618, 4.6287, 4.6189, 4.508, 4.4187, 4.26, 4.1643, 4.1334, 4.126, 4.1142, 4.0725, 4.0357, 4.0115, 3.862, 3.824, 3.7705, 3.7573, 3.6644, 3.59, 3.5321, 3.5234, 3.513, 3.5022, 3.4778, 3.4226. 3.3408, 3.3371, 3.2395, 3.2003, 3.1964, 3.1292, 3.114, 3.1084, 3.0979, 3.0814, 3.0704, 3.0571, 2.9666, 2.9482, 2.9162, 2.9086, 2.8964, 2.8726, 2.7516, 2.6354, 2.5784, 2.5332, 2.5051, 2.4943, 2.4478, 2.4286, 2.3616, 2.3397, 2.3224, 2.2793, 2.2409, 2.1602, 2.1382, 2.103, 2.091, 2.084, 1.9619, 1.9568, 1.9187, 1.9043, 1.7495, 1.7303, 1.7221, 1.7199, 1.6476, 1.5988, 1.5699, 1.5517, 1.5488, 1.5448, 1.4773, 1.4683, 1.3762, 1.3484, 1.3233, 1.2736, 1.2355, 1.2112, 1.1925, 1.1622, 1.1369, 1.0621, 1.0591, 1.0488, 0.9689, 0.87512, 0.84124, 0.8269, 0.7769, 0.767, 0.75692, 0.7274, 0.7109, 0.6997, 0.69719, 0.6886, 0.6706, 0.6429, 0.6273, 0.6131, 0.6107, 0.60538, 0.5912, 0.57081, 0.5525, 0.5374, 0.465. 0.43943, 0.3791, 0.3747, 0.28703, 0.2804
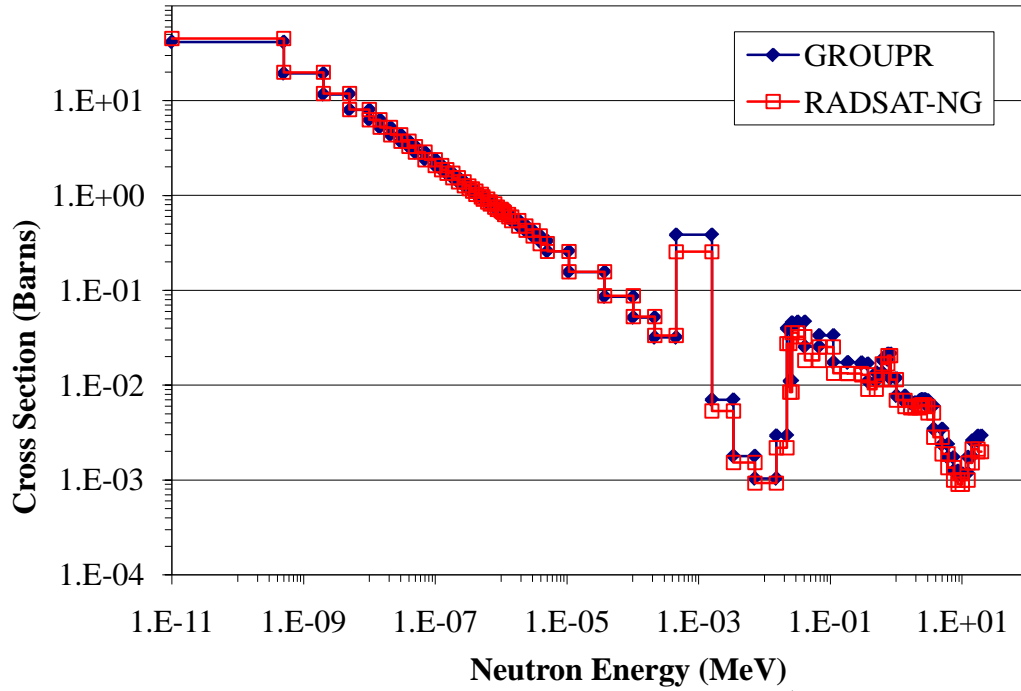
Figure 38. Comparison of the GROUPR and RADSAT-NG ^{56}Fe Radiative Capture
Photon Production Cross Section
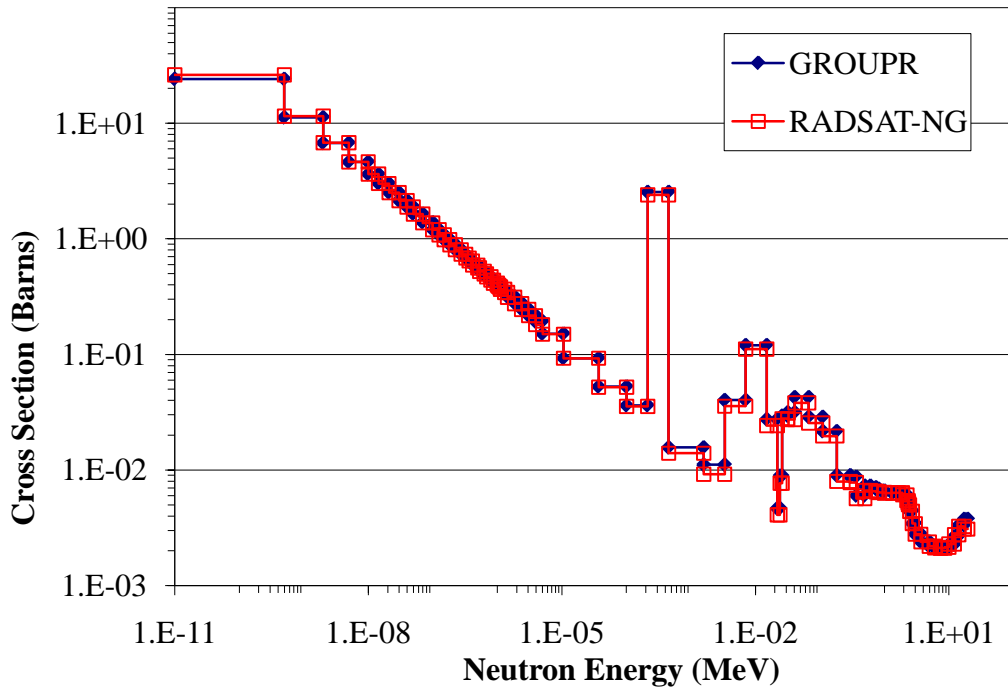
Figure 39. Comparison of the GROUPR and RADSAT-NG ^{58}Fe Radiative Capture
Photon Production Cross Section

A comparison of all of the RADSAT-NG photon production cross section for ^{54}Fe, ^{56}Fe and ^{58}Fe and the GROUPR collapsed cross sections is shown in Table 19. Most of these cross sections agree to within a few percent of the GROUPR collapsed cross sections. For the ^{54}Fe (n,2n) interaction, the RADSAT-NG and GROUPR photon production cross sections differ by 22.64%. The difference is due to a factor of 1.7 and a factor of 2.5 differences in the second and third highest energy groups, respectively. Similarly for the ^{54}Fe (n,nα) photon production cross section, the RADSAT-NG and GROUPR photon production cross sections differ by 42.20% due to a difference in the second and third highest energy groups of a factor of 2.3 and 1.5, respectively. The 15% difference in the ^{54}Fe (n,np) photon production cross section for RADSAT-NG and GROUPR is due to a factor of 1.5 difference in the fourth highest energy group. For the ^{56}Fe (n,p) photon production cross section, the RADSAT-NG and GROUPR collapsed cross sections differ by approximately 7.16%. This is due to the fact that the all of the energy groups calculated by the RADSAT-NG and GROUPR method differ consistently by a range of 6 to 15%. A graphical comparison of the RADSAT-NG and GROUPR ^{56}Fe (n,p) cross section is shown in Figure 40. Finally the 17.56% difference in the ^{58}Fe (n,2n) photon production cross section for RADSAT-NG and GROUPR is due to a constant 13~19% difference all four energy groups the cross section is present in. The remainder of the RADSAT-NG cross sections agree with the GROUPR collapsed cross sections to within approximately 3% or better.

Table 19. Comparison of Total Cross Section for RADSAT-NG and Cross Sections
Produced by GROUPR for Iron

Cross Section	RADSAT-NG Total Cross Section (Barns)	GROUPR Total Cross Section (Barns)	Percent Difference (%)
^{54}Fe (n,n')	2.09E+01	2.12E+01	1.22
^{54}Fe (n,2n)	8.22E-02	6.70E-02	22.64
^{54}Fe (n,nα)	6.26E-02	4.40E-02	42.20
^{54}Fe (n,np)	1.30E+00	1.13E+00	15.54
^{54}Fe (n,γ)	1.08E+02	1.05E+02	3.12
^{54}Fe (n,p)	7.25E+00	7.34E+00	1.14
^{54}Fe (n,α)	7.99E-01	7.89E-01	1.27
^{56}Fe (n,n')	3.54E+01	3.54E+01	8.18E-05
^{56}Fe (n,2n)	1.70E+00	1.70E+00	0.03
^{56}Fe (n,nα)	5.12E-02	4.98E-02	2.91
^{56}Fe (n,np)	4.07E-01	4.04E-01	0.71
^{56}Fe (n,γ)	1.38E+02	1.34E+02	3.03
^{56}Fe (n,p)	1.18E+00	1.27E+00	7.16
^{56}Fe (n,α)	4.11E-01	4.11E-01	0.17
^{57}Fe (n,n')	7.08E+01	------	------
^{57}Fe (n,2n)	7.37E+00	------	------
^{57}Fe (n,nα)	6.98E-02	------	------
^{57}Fe (n,np)	2.79E-01	------	------
^{57}Fe (n,γ)	2.32E+02	------	------
^{57}Fe (n,p)	5.24E-01	------	------
^{57}Fe (n,α)	3.86E-01	------	------
^{58}Fe (n,n')	3.72E+01	3.71E+01	0.27
^{58}Fe (n,2n)	6.37E+00	7.73E+00	17.56
^{58}Fe (n,nα)	2.59E-02	2.56E-02	1.15
^{58}Fe (n,np)	4.54E-02	4.42E-02	2.71
^{58}Fe (n,γ)	8.25E+01	8.02E+01	2.87
^{58}Fe (n,p)	8.81E-02	8.92E-02	1.25
^{58}Fe (n,α)	1.57E-01	1.58E-01	0.62
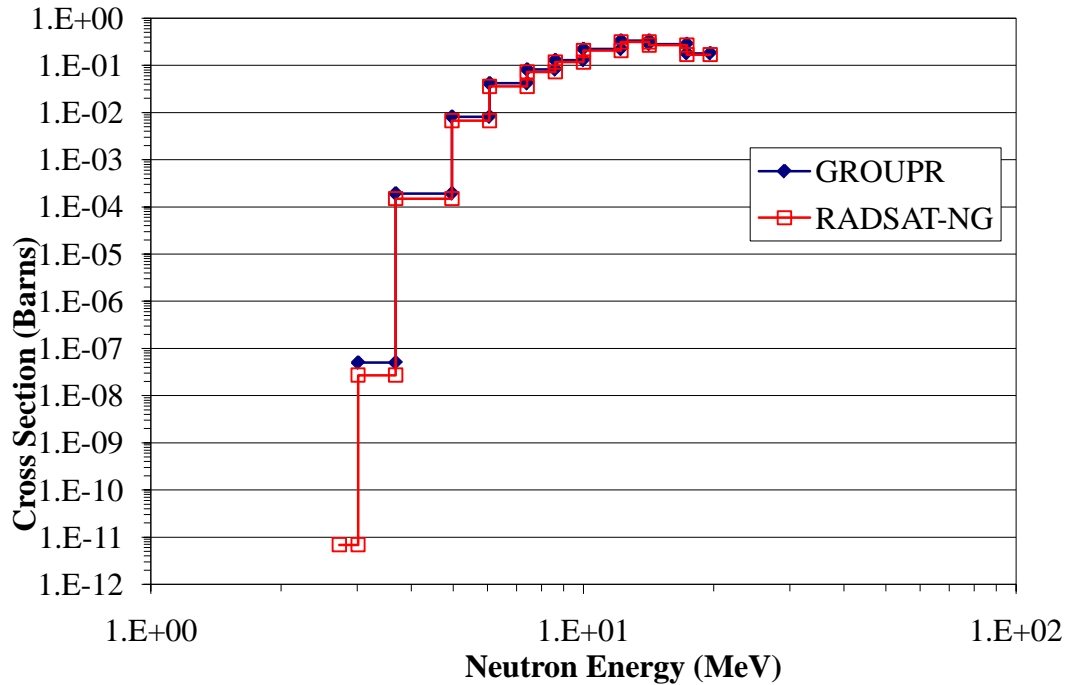
Figure 40. Comparison of the GROUPR and RADSAT-NG ^{56}Fe (n,p) Photon Production
Cross Section

3.5.3   Photon Flux within Detector

Once the induced photon spectrum has been calculated for the irradiation of iron

using the RADSAT-NG cross sections and the spatially dependent neutron flux obtained

from Attila, the problem dependent photon group structure was generated using the

RADSAT interface. The RADSAT group generator then was used to produce the

specialized photon group structure containing 150 continuum groups and 149 0.3-keV

wide peak groups, one for the 511-keV annihilation peak and the remaining peak groups

148 most intense gamma rays produced by iron. Although a $1/\sqrt{E}$ energy weighting

factor was supplied, this will not affect the spacing of the continuum groups like it

normally would since there are just enough continuum groups to place one between every

peak group. Additionally, a 2-cm thick glass attenuator was applied to the source

spectrum for the purpose of choosing the photon group structure. The purpose of the attenuator feature is to artificially reduce the intensity of the x-rays produced that would not greatly impact the detector response. This feature is only used for the purpose of choosing a photon energy bin structure. It allows the group generator to reduce the importance of these high intensity low energy gamma rays while increasing the importance of other lower intensity higher energy gamma rays which may be more noticeable in the final detector response than the x-rays.

A comparison of the volume-averaged gamma flux in the detector from the neutron irradiation of iron calculated using the RADSAT method and MCNP is shown in Figure 41. The total photon flux within the detector for the RADSAT calculation is within 7.03% of the MCNP result. This is probably due to the RADSAT calculation not properly accounting for the low angle scatter properly in this region below the 849.5 keV gamma ray. This artifact does not typically affect the detector response because this energy region is dominated by Compton Scattering interactions in the detector. The seven most intense gamma rays for MCNP and RADSAT show typical agreement to within 2%. The statistical uncertainty of the MCNP simulation for the same gamma ray emissions is equal to or greater than the percent difference between the MCNP and RADSAT calculations as shown in Table 20.
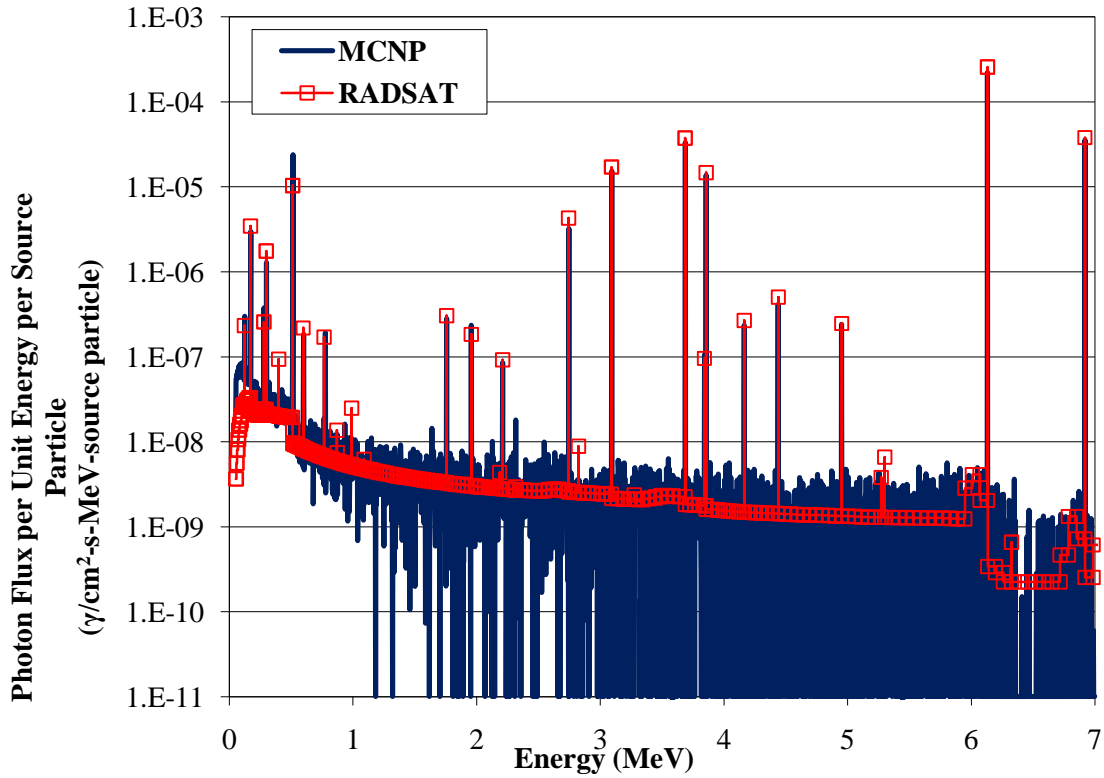
Table 20. Comparison of Photon Flux for Top Seven Most Intense Peaks Produced by the Neutron Irradiation of Iron

Gamma-Ray Energy (MeV)	MCNP (γ/cm^2-sec-source particle)	MCNP Relative Uncertainty (%)	RADSAT (γ/cm^2-sec-source particle)	Percent Difference (%)
0.8495	5.52E-06	1.16	5.63E-06	1.92
1.24	5.89E-07	3.62	5.91E-07	0.20
1.811	3.51E-07	4.71	3.52E-07	0.42
2.113	2.11E-07	6.13	2.11E-07	0.41
2.273	1.22E-07	7.8	1.20E-07	1.24
2.517	1.02E-07	9.13	1.03E-07	0.71
2.6031	1.15E-07	10.66	1.15E-07	0.63
Total	1.29E-05	0.75	1.38E-05	7.03
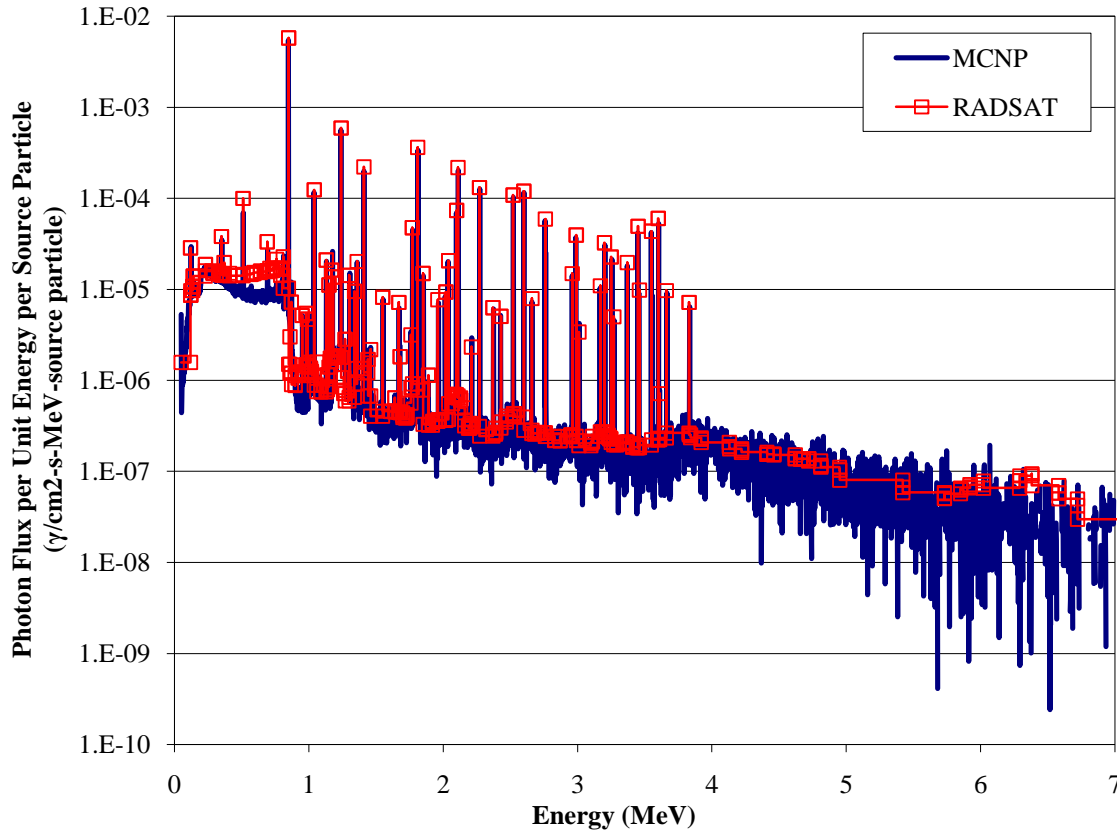
Figure 41. Comparison of Volume-Averaged Photon Flux in Detector using RADSAT and MCNP for Iron

CHAPTER 4

CONCLUSIONS

Based on the series of simple benchmarking problems, and the comparison to MCNP5 results, the coupled Monte Carlo-deterministic transport methods being developed and implemented in RADSAT are capable of accurately and efficiently modeling neutron-induced gamma rays for high-resolution gamma-ray spectroscopy applications. The series of simple benchmark problems showed good agreement between RADSAT- and MCNP-calculated photon production rates and photon transport to a detector location, typically within 5% for the 5 highest intensity gamma rays. The polyethylene test case demonstrated good agreement between RADSAT and MCNP for a pulse-height tally, within 5% for the prominent peak regions, in a high-resolution HPGe spectrometer.

The key enabler for RADSAT neutron-gamma method is the RADSAT-NG multigroup cross-section preparation method development in this work which, unlike currently available neutron-gamma cross-section libraries and preparation methods, tabulates the discrete-energy and continuum neutron-induced photon source terms separately. The comparison of the RADSAT-NG cross section library and cross sections collapsed using the GROUPR subroutine of NJOY typically showed good agreement. The main discrepancy present in the comparison of the two methods is in the first and last energy groups with cross sections. The general shape and magnitude of the RADSAT-NG multigroup cross-section preparation method is the same as the cross sections collapsed using the GROUPR subroutine of NJOY.

While demonstrating solution accuracy is the necessary first step in the use of RADSAT for coupled neutron-photon problems for high-resolution gamma-ray spectroscopy applications, the primary motivator for using the coupled method over pure Monte Carlo method is the potential for significantly lower computational times which may enable new ways of approaching some high-resolution gamma-ray applications. In this work, the RADSAT and MCNP5 computational times for each problem were recorded, and normalized to a typical single-processor 3 GHz desktop computer. For the series of test cases, the run times for RADSAT were approximately 25-500 times shorter than for MCNP, when assuming a 40 mCi ^{252}Cf neutron source and 600 seconds of "real-world measurement time," as shown in Table 21.

Table 21. Comparison of MCNP and RADSAT Computational Times for Simple Cube Problems

Simulation	RADSAT (hours)	MCNP (hours)	Run-Time Ratio
Polyethylene	5	914	183
Phosphorus	1.9	910	479
Nitrogen	3	84	28
Oxygen	3.5	93	27
Iron	5	198	40

The run-time comparisons can vary depending on the composition of materials in the problem and size or complexity of the problem geometry. The calculations completed in RADSAT were used primarily to complete a proof of principle, so little effort was spent optimizing the RADSAT calculational parameters in order to reduce run time. Two forms of variance reduction were used in the MCNP simulations, the geometric biasing of the neutron source toward the cube and neutron importance weighting in the detector

volume to compare the induced photon spectrum from specific materials. However, additional variance reduction techniques could substantially reduce run times for specific problems.

This study represents a proof-of-principle study for the coupled Monte Carlo-deterministic method to simulate neutron-induced gamma rays for high-resolution gamma-ray spectroscopy applications. This work, therefore, represents only a preliminary assessment of RADSAT methods using a narrow subset of neutron-induced photon problems.

CHAPTER 5

RECOMMENDATIONS

Although promising results have been obtained from the proof-of-concept

analysis, additional testing to determine the range of applicability of the method will need

to be completed before this method will be fully integrated into the RADSAT package.

The results produced in this study were for a simple geometry and only covered a limited

number of materials. Although the RADSAT-NG cross-section preparation method has

been shown to produce acceptable results for the materials tested, the method still needs

to be tested for more materials, particularly materials containing unresolved resonances.

More complex geometries should also be tested to determine how the assumption of

isotropic photon production affects the photon flux at the detector location. The

systematic bias between MCNP and Attila calculated flux at low energies although not

central to this work, must be resolved, and understood in order to increase confidence in

the RADSAT coupled neutron gamma and neutron-only calculations. Additional

evaluation of spatial discretization in the calculation of neutron flux and neutron-induced

photon source terms will shed more light on both aspects—accuracy and computational

efficiency—and allow a more thorough evaluation of the strengths and limitations of

RADSAT methods over a wide range of radiation detection problems.

Experimental validation of computer codes is an important step in determining if

the computational method is working properly. A set of benchmarking experiments

should be developed to determine if the RADSAT coupled neutron gamma method is

working properly. It should be noted that the ability to properly benchmark the

RADSAT-NG method will depend on the accuracy of the underlying cross section library

that was collapsed, not just the cross section collapsing method or the transport method.

The experimental validation will help point out short comings that may be common to

both the RADSAT-NG method and MCNP.

In order for the methods developed in this study to be properly integrated into the

RADSAT interface, some additions to the RADSAT user interface are necessary. The

RADSAT-NG cross-section preparation method has already been implemented into a

program RADSAT-NG_Collapser which is currently being tested. The calculations of the

neutron-induced photon spectra are completed using a Visual Basic script external from

the RADSAT interface. The results must then be loaded into the RADSAT interface as

source terms. In order to remove this intermediate step, these calculations will be

completed within the RADSAT interface. The integration of these procedures into the

code has not yet begun but is anticipated to begin in the near future.

APPENDIX A

Example Attila Input File for Neutron Transport Problem in C_2H_4

```
rtt_attila_input

header_block
  version 1.0.0
  title "Poly_Ge_Coarse_79_S16P2"
  info "C2H4 Cube Test2_5cm_Ge Coarse Mesh - 5 cm 79 group cross-section library
Transport Parameters - S16P2 "

input_file_block
  mesh_file_type rtt
  mesh_file "../Test2_5cm_Ge_5cm.mesh.inp"
  volume_source_file "Poly_Ge_Coarse_79_S16P2.vsrc.inp"
  edit_file "Poly_Ge_Coarse_79_S16P2.edit.inp"
  cross_section_file "../kynea3_4e18.xs.inp"
  aux_xs_file "../kynea3_4e18.xs_aux.inp"

output_controls_block
  output_prefix "Poly_Ge_Coarse_79_S16P2"
  write_tecplot_file .true.
  scratch_directory "./"

transport_controls_block
  angular_quadrature_def
    aqd_quad_name "QSet_0001"
    aqd_quad_verbosity silent
    aqd_sn_quadrature_set tri_cheby_lobatto
    aqd_sn_order 16
    aqd_moment_to_discrete_map galerkin
  end_angular_quadrature_def
  scattering_degree 2
  problem_type steady_state
  starting_moments zero

energy_group_block
  collapse_strategy noclps
  ngroups 79

iteration_controls_block
  max_outers 200
  si_conv_criteria 0.0001
```

dummy_solution .false.

mesh_region_definition_block
 region_index 1
 side_index 2
 region_def 1 "Universe" 2 0.001205
 region_def 2 "Source_Box" 2 0.001205
 region_def 3 "detector" 2 0.001205
 region_def 4 "cube4_4_4" 1 0.5
 region_def 5 "cube4_4_3" 1 0.5
 region_def 6 "cube4_4_2" 1 0.5
 region_def 7 "cube4_4_1" 1 0.5
 region_def 8 "cube4_3_4" 1 0.5
 region_def 9 "cube4_3_3" 1 0.5
 region_def 10 "cube4_3_2" 1 0.5
 region_def 11 "cube4_3_1" 1 0.5
 region_def 12 "cube4_2_4" 1 0.5
 region_def 13 "cube4_2_3" 1 0.5
 region_def 14 "cube4_2_2" 1 0.5
 region_def 15 "cube4_2_1" 1 0.5
 region_def 16 "cube4_1_4" 1 0.5
 region_def 17 "cube4_1_3" 1 0.5
 region_def 18 "cube4_1_2" 1 0.5
 region_def 19 "cube4_1_1" 1 0.5
 region_def 20 "cube3_4_4" 1 0.5
 region_def 21 "cube3_4_3" 1 0.5
 region_def 22 "cube3_4_2" 1 0.5
 region_def 23 "cube3_4_1" 1 0.5
 region_def 24 "cube3_3_4" 1 0.5
 region_def 25 "cube3_3_3" 1 0.5
 region_def 26 "cube3_3_2" 1 0.5
 region_def 27 "cube3_3_1" 1 0.5
 region_def 28 "cube3_2_4" 1 0.5
 region_def 29 "cube3_2_3" 1 0.5
 region_def 30 "cube3_2_2" 1 0.5
 region_def 31 "cube3_2_1" 1 0.5
 region_def 32 "cube3_1_4" 1 0.5
 region_def 33 "cube3_1_3" 1 0.5
 region_def 34 "cube3_1_2" 1 0.5
 region_def 35 "cube3_1_1" 1 0.5
 region_def 36 "cube2_4_4" 1 0.5
 region_def 37 "cube2_4_3" 1 0.5
 region_def 38 "cube2_4_2" 1 0.5
 region_def 39 "cube2_4_1" 1 0.5
 region_def 40 "cube2_3_4" 1 0.5
 region_def 41 "cube2_3_3" 1 0.5

region_def 42 "cube2_3_2" 1 0.5
region_def 43 "cube2_3_1" 1 0.5
region_def 44 "cube2_2_4" 1 0.5
region_def 45 "cube2_2_3" 1 0.5
region_def 46 "cube2_2_2" 1 0.5
region_def 47 "cube2_2_1" 1 0.5
region_def 48 "cube2_1_4" 1 0.5
region_def 49 "cube2_1_3" 1 0.5
region_def 50 "cube2_1_2" 1 0.5
region_def 51 "cube2_1_1" 1 0.5
region_def 52 "cube1_4_4" 1 0.5
region_def 53 "cube1_4_3" 1 0.5
region_def 54 "cube1_4_2" 1 0.5
region_def 55 "cube1_4_1" 1 0.5
region_def 56 "cube1_3_4" 1 0.5
region_def 57 "cube1_3_3" 1 0.5
region_def 58 "cube1_3_2" 1 0.5
region_def 59 "cube1_3_1" 1 0.5
region_def 60 "cube1_2_4" 1 0.5
region_def 61 "cube1_2_3" 1 0.5
region_def 62 "cube1_2_2" 1 0.5
region_def 63 "cube1_2_1" 1 0.5
region_def 64 "cube1_1_4" 1 0.5
region_def 65 "cube1_1_3" 1 0.5
region_def 66 "cube1_1_2" 1 0.5
region_def 67 "cube1_1_1" 1 0.5
side_def 1 "(+)Universe@5"
side_def 79 "(+)Universe@2"
side_def 81 "(+)Universe@3"
side_def 83 "(+)Universe@4"
side_def 85 "(+)Universe@1"
side_def 160 "(+)Universe@6"
side_def 250 "(+)Universe/(-)cube1_4_1@1"
side_def 268 "(+)Universe/(-)cube4_4_1@3"
side_def 286 "(+)Universe/(-)cube4_4_4@3"
side_def 304 "(+)Universe/(-)cube4_1_4@2"
side_def 322 "(+)Universe/(-)cube1_4_4@2"
side_def 340 "(+)Universe/(-)cube4_4_4@1"
side_def 409 "(+)Universe/(-)detector@5"
side_def 412 "(+)Universe/(-)detector@2"
side_def 415 "(+)Universe/(-)detector@3"
side_def 418 "(+)Universe/(-)detector@4"
side_def 421 "(+)Universe/(-)detector@6"
side_def 424 "(+)Universe/(-)detector@1"
side_def 478 "(+)Universe/(-)Source_Box@5"
side_def 481 "(+)Universe/(-)Source_Box@2"

```
side_def 484 "(+)Universe/(-)Source_Box@3"
side_def 487 "(+)Universe/(-)Source_Box@4"
side_def 490 "(+)Universe/(-)Source_Box@6"
side_def 493 "(+)Universe/(-)Source_Box@1"
side_def 1285 "(+)Universe/(-)cube4_3_4@1"
side_def 1299 "(+)Universe/(-)cube4_4_3@2"
side_def 1309 "(+)Universe/(-)cube4_4_4@2"
side_def 1363 "(+)cube4_4_4/(-)cube3_4_4@1"
side_def 1369 "(+)cube4_4_4/(-)cube4_3_4@1"
side_def 1381 "(+)cube4_4_4/(-)cube4_4_3@1"
side_def 1491 "(+)Universe/(-)cube4_4_3@1"
side_def 1501 "(+)Universe/(-)cube4_4_2@2"
side_def 1562 "(+)cube4_4_3/(-)cube3_4_3@1"
side_def 1568 "(+)cube4_4_3/(-)cube4_3_3@1"
side_def 1580 "(+)cube4_4_3/(-)cube4_4_2@1"
side_def 1691 "(+)Universe/(-)cube4_4_2@1"
side_def 1701 "(+)Universe/(-)cube4_4_1@2"
side_def 1769 "(+)cube4_4_2/(-)cube3_4_2@1"
side_def 1775 "(+)cube4_4_2/(-)cube4_3_2@1"
side_def 1787 "(+)cube4_4_2/(-)cube4_4_1@1"
side_def 1895 "(+)Universe/(-)cube4_4_1@1"
side_def 1905 "(+)Universe/(-)cube4_3_4@2"
side_def 1914 "(+)Universe/(-)cube4_3_1@2"
side_def 1993 "(+)cube4_4_1/(-)cube3_4_1@1"
side_def 1999 "(+)cube4_4_1/(-)cube4_3_1@1"
side_def 2125 "(+)Universe/(-)cube4_3_3@1"
side_def 2134 "(+)Universe/(-)cube4_2_4@2"
side_def 2216 "(+)cube4_3_4/(-)cube3_3_4@1"
side_def 2222 "(+)cube4_3_4/(-)cube4_2_4@1"
side_def 2234 "(+)cube4_3_4/(-)cube4_3_3@1"
side_def 2344 "(+)Universe/(-)cube4_3_2@1"
side_def 2432 "(+)cube4_3_3/(-)cube3_3_3@1"
side_def 2438 "(+)cube4_3_3/(-)cube4_2_3@1"
side_def 2450 "(+)cube4_3_3/(-)cube4_3_2@1"
side_def 2561 "(+)Universe/(-)cube4_3_1@1"
side_def 2655 "(+)cube4_3_2/(-)cube3_3_2@1"
side_def 2661 "(+)cube4_3_2/(-)cube4_2_2@1"
side_def 2673 "(+)cube4_3_2/(-)cube4_3_1@1"
side_def 2788 "(+)Universe/(-)cube4_2_1@2"
side_def 2794 "(+)Universe/(-)cube4_2_4@1"
side_def 2898 "(+)cube4_3_1/(-)cube3_3_1@1"
side_def 2904 "(+)cube4_3_1/(-)cube4_2_1@1"
side_def 3034 "(+)Universe/(-)cube4_2_3@1"
side_def 3043 "(+)Universe/(-)cube4_1_4@3"
side_def 3150 "(+)cube4_2_4/(-)cube3_2_4@1"
side_def 3156 "(+)cube4_2_4/(-)cube4_1_4@1"
```

```
side_def 3168 "(+)cube4_2_4/(-)cube4_2_3@1"
side_def 3282 "(+)Universe/(-)cube4_2_2@1"
side_def 3395 "(+)cube4_2_3/(-)cube3_2_3@1"
side_def 3401 "(+)cube4_2_3/(-)cube4_1_3@1"
side_def 3413 "(+)cube4_2_3/(-)cube4_2_2@1"
side_def 3528 "(+)Universe/(-)cube4_2_1@1"
side_def 3647 "(+)cube4_2_2/(-)cube3_2_2@1"
side_def 3653 "(+)cube4_2_2/(-)cube4_1_2@1"
side_def 3665 "(+)cube4_2_2/(-)cube4_2_1@1"
side_def 3784 "(+)Universe/(-)cube4_1_1@2"
side_def 3790 "(+)Universe/(-)cube4_1_1@1"
side_def 3919 "(+)cube4_2_1/(-)cube3_2_1@1"
side_def 3925 "(+)cube4_2_1/(-)cube4_1_1@1"
side_def 4056 "(+)Universe/(-)cube4_1_4@1"
side_def 4070 "(+)Universe/(-)cube4_1_3@2"
side_def 4076 "(+)Universe/(-)cube3_4_4@1"
side_def 4212 "(+)cube4_1_4/(-)cube3_1_4@1"
side_def 4226 "(+)cube4_1_4/(-)cube4_1_3@1"
side_def 4350 "(+)Universe/(-)cube4_1_3@1"
side_def 4360 "(+)Universe/(-)cube4_1_2@2"
side_def 4502 "(+)cube4_1_3/(-)cube3_1_3@1"
side_def 4516 "(+)cube4_1_3/(-)cube4_1_2@1"
side_def 4641 "(+)Universe/(-)cube4_1_2@1"
side_def 4651 "(+)Universe/(-)cube4_1_1@3"
side_def 4799 "(+)cube4_1_2/(-)cube3_1_2@1"
side_def 4813 "(+)cube4_1_2/(-)cube4_1_1@1"
side_def 4938 "(+)Universe/(-)cube3_1_4@2"
side_def 4944 "(+)Universe/(-)cube3_4_1@2"
side_def 5101 "(+)cube4_1_1/(-)cube3_1_1@1"
side_def 5243 "(+)Universe/(-)cube3_3_4@1"
side_def 5253 "(+)Universe/(-)cube3_4_4@2"
side_def 5409 "(+)cube3_4_4/(-)cube2_4_4@1"
side_def 5415 "(+)cube3_4_4/(-)cube3_3_4@1"
side_def 5427 "(+)cube3_4_4/(-)cube3_4_3@1"
side_def 5549 "(+)Universe/(-)cube3_4_3@1"
side_def 5711 "(+)cube3_4_3/(-)cube2_4_3@1"
side_def 5717 "(+)cube3_4_3/(-)cube3_3_3@1"
side_def 5729 "(+)cube3_4_3/(-)cube3_4_2@1"
side_def 5852 "(+)Universe/(-)cube3_4_2@1"
side_def 6020 "(+)cube3_4_2/(-)cube2_4_2@1"
side_def 6026 "(+)cube3_4_2/(-)cube3_3_2@1"
side_def 6038 "(+)cube3_4_2/(-)cube3_4_1@1"
side_def 6162 "(+)Universe/(-)cube3_4_1@1"
side_def 6171 "(+)Universe/(-)cube3_3_1@1"
side_def 6349 "(+)cube3_4_1/(-)cube2_4_1@1"
side_def 6355 "(+)cube3_4_1/(-)cube3_3_1@1"
```

```
side_def 6492 "(+)Universe/(-)cube3_2_4@1"
side_def 6672 "(+)cube3_3_4/(-)cube2_3_4@1"
side_def 6678 "(+)cube3_3_4/(-)cube3_2_4@1"
side_def 6690 "(+)cube3_3_4/(-)cube3_3_3@1"
side_def 6991 "(+)cube3_3_3/(-)cube2_3_3@1"
side_def 6997 "(+)cube3_3_3/(-)cube3_2_3@1"
side_def 7009 "(+)cube3_3_3/(-)cube3_3_2@1"
side_def 7316 "(+)cube3_3_2/(-)cube2_3_2@1"
side_def 7322 "(+)cube3_3_2/(-)cube3_2_2@1"
side_def 7334 "(+)cube3_3_2/(-)cube3_3_1@1"
side_def 7461 "(+)Universe/(-)cube3_2_1@1"
side_def 7660 "(+)cube3_3_1/(-)cube2_3_1@1"
side_def 7666 "(+)cube3_3_1/(-)cube3_2_1@1"
side_def 7807 "(+)Universe/(-)cube3_1_4@1"
side_def 8008 "(+)cube3_2_4/(-)cube2_2_4@1"
side_def 8014 "(+)cube3_2_4/(-)cube3_1_4@1"
side_def 8026 "(+)cube3_2_4/(-)cube3_2_3@1"
side_def 8352 "(+)cube3_2_3/(-)cube2_2_3@1"
side_def 8358 "(+)cube3_2_3/(-)cube3_1_3@1"
side_def 8370 "(+)cube3_2_3/(-)cube3_2_2@1"
side_def 8702 "(+)cube3_2_2/(-)cube2_2_2@1"
side_def 8708 "(+)cube3_2_2/(-)cube3_1_2@1"
side_def 8720 "(+)cube3_2_2/(-)cube3_2_1@1"
side_def 8851 "(+)Universe/(-)cube3_1_1@2"
side_def 9071 "(+)cube3_2_1/(-)cube2_2_1@1"
side_def 9077 "(+)cube3_2_1/(-)cube3_1_1@1"
side_def 9227 "(+)Universe/(-)cube3_1_3@1"
side_def 9233 "(+)Universe/(-)cube2_4_4@1"
side_def 9459 "(+)cube3_1_4/(-)cube2_1_4@1"
side_def 9473 "(+)cube3_1_4/(-)cube3_1_3@1"
side_def 9612 "(+)Universe/(-)cube3_1_2@1"
side_def 9843 "(+)cube3_1_3/(-)cube2_1_3@1"
side_def 9857 "(+)cube3_1_3/(-)cube3_1_2@1"
side_def 9997 "(+)Universe/(-)cube3_1_1@1"
side_def 10233 "(+)cube3_1_2/(-)cube2_1_2@1"
side_def 10247 "(+)cube3_1_2/(-)cube3_1_1@1"
side_def 10388 "(+)Universe/(-)cube2_4_1@2"
side_def 10394 "(+)Universe/(-)cube2_1_4@2"
side_def 10639 "(+)cube3_1_1/(-)cube2_1_1@1"
side_def 10798 "(+)Universe/(-)cube2_4_4@2"
side_def 10807 "(+)Universe/(-)cube2_3_4@1"
side_def 11051 "(+)cube2_4_4/(-)cube1_4_4@1"
side_def 11057 "(+)cube2_4_4/(-)cube2_3_4@1"
side_def 11069 "(+)cube2_4_4/(-)cube2_4_3@1"
side_def 11207 "(+)Universe/(-)cube2_4_3@1"
side_def 11457 "(+)cube2_4_3/(-)cube1_4_3@1"
```

```
side_def 11463 "(+)cube2_4_3/(-)cube2_3_3@1"
side_def 11475 "(+)cube2_4_3/(-)cube2_4_2@1"
side_def 11614 "(+)Universe/(-)cube2_4_2@1"
side_def 11870 "(+)cube2_4_2/(-)cube1_4_2@1"
side_def 11876 "(+)cube2_4_2/(-)cube2_3_2@1"
side_def 11888 "(+)cube2_4_2/(-)cube2_4_1@1"
side_def 12028 "(+)Universe/(-)cube2_4_1@1"
side_def 12037 "(+)Universe/(-)cube2_3_1@1"
side_def 12303 "(+)cube2_4_1/(-)cube1_4_1@1"
side_def 12309 "(+)cube2_4_1/(-)cube2_3_1@1"
side_def 12462 "(+)Universe/(-)cube2_2_4@1"
side_def 12730 "(+)cube2_3_4/(-)cube1_3_4@1"
side_def 12736 "(+)cube2_3_4/(-)cube2_2_4@1"
side_def 12748 "(+)cube2_3_4/(-)cube2_3_3@1"
side_def 13153 "(+)cube2_3_3/(-)cube1_3_3@1"
side_def 13159 "(+)cube2_3_3/(-)cube2_2_3@1"
side_def 13171 "(+)cube2_3_3/(-)cube2_3_2@1"
side_def 13582 "(+)cube2_3_2/(-)cube1_3_2@1"
side_def 13588 "(+)cube2_3_2/(-)cube2_2_2@1"
side_def 13600 "(+)cube2_3_2/(-)cube2_3_1@1"
side_def 13743 "(+)Universe/(-)cube2_2_1@1"
side_def 14030 "(+)cube2_3_1/(-)cube1_3_1@1"
side_def 14036 "(+)cube2_3_1/(-)cube2_2_1@1"
side_def 14193 "(+)Universe/(-)cube2_1_4@1"
side_def 14482 "(+)cube2_2_4/(-)cube1_2_4@1"
side_def 14488 "(+)cube2_2_4/(-)cube2_1_4@1"
side_def 14500 "(+)cube2_2_4/(-)cube2_2_3@1"
side_def 14930 "(+)cube2_2_3/(-)cube1_2_3@1"
side_def 14936 "(+)cube2_2_3/(-)cube2_1_3@1"
side_def 14948 "(+)cube2_2_3/(-)cube2_2_2@1"
side_def 15384 "(+)cube2_2_2/(-)cube1_2_2@1"
side_def 15390 "(+)cube2_2_2/(-)cube2_1_2@1"
side_def 15402 "(+)cube2_2_2/(-)cube2_2_1@1"
side_def 15549 "(+)Universe/(-)cube2_1_1@2"
side_def 15857 "(+)cube2_2_1/(-)cube1_2_1@1"
side_def 15863 "(+)cube2_2_1/(-)cube2_1_1@1"
side_def 16029 "(+)Universe/(-)cube2_1_3@1"
side_def 16035 "(+)Universe/(-)cube1_4_4@1"
side_def 16349 "(+)cube2_1_4/(-)cube1_1_4@1"
side_def 16363 "(+)cube2_1_4/(-)cube2_1_3@1"
side_def 16518 "(+)Universe/(-)cube2_1_2@1"
side_def 16837 "(+)cube2_1_3/(-)cube1_1_3@1"
side_def 16851 "(+)cube2_1_3/(-)cube2_1_2@1"
side_def 17007 "(+)Universe/(-)cube2_1_1@1"
side_def 17331 "(+)cube2_1_2/(-)cube1_1_2@1"
side_def 17345 "(+)cube2_1_2/(-)cube2_1_1@1"
```

```
side_def 17502 "(+)Universe/(-)cube1_4_1@3"
side_def 17508 "(+)Universe/(-)cube1_1_1@3"
side_def 17841 "(+)cube2_1_1/(-)cube1_1_1@1"
side_def 18013 "(+)Universe/(-)cube1_4_4@3"
side_def 18028 "(+)Universe/(-)cube1_4_3@2"
side_def 18034 "(+)Universe/(-)cube1_3_4@1"
side_def 18372 "(+)cube1_4_4/(-)cube1_3_4@1"
side_def 18384 "(+)cube1_4_4/(-)cube1_4_3@1"
side_def 18544 "(+)Universe/(-)cube1_4_3@1"
side_def 18555 "(+)Universe/(-)cube1_4_2@2"
side_def 18899 "(+)cube1_4_3/(-)cube1_3_3@1"
side_def 18911 "(+)cube1_4_3/(-)cube1_4_2@1"
side_def 19072 "(+)Universe/(-)cube1_4_2@1"
side_def 19083 "(+)Universe/(-)cube1_4_1@2"
side_def 19433 "(+)cube1_4_2/(-)cube1_3_2@1"
side_def 19445 "(+)cube1_4_2/(-)cube1_4_1@1"
side_def 19607 "(+)Universe/(-)cube1_3_4@2"
side_def 19613 "(+)Universe/(-)cube1_3_1@2"
side_def 19972 "(+)cube1_4_1/(-)cube1_3_1@1"
side_def 20150 "(+)Universe/(-)cube1_3_3@1"
side_def 20156 "(+)Universe/(-)cube1_2_4@1"
side_def 20517 "(+)cube1_3_4/(-)cube1_2_4@1"
side_def 20529 "(+)cube1_3_4/(-)cube1_3_3@1"
side_def 20693 "(+)Universe/(-)cube1_3_2@1"
side_def 21059 "(+)cube1_3_3/(-)cube1_2_3@1"
side_def 21071 "(+)cube1_3_3/(-)cube1_3_2@1"
side_def 21236 "(+)Universe/(-)cube1_3_1@1"
side_def 21607 "(+)cube1_3_2/(-)cube1_2_2@1"
side_def 21619 "(+)cube1_3_2/(-)cube1_3_1@1"
side_def 21784 "(+)Universe/(-)cube1_2_1@2"
side_def 21791 "(+)Universe/(-)cube1_2_4@2"
side_def 22171 "(+)cube1_3_1/(-)cube1_2_1@1"
side_def 22353 "(+)Universe/(-)cube1_2_3@1"
side_def 22359 "(+)Universe/(-)cube1_1_4@1"
side_def 22741 "(+)cube1_2_4/(-)cube1_1_4@1"
side_def 22753 "(+)cube1_2_4/(-)cube1_2_3@1"
side_def 22921 "(+)Universe/(-)cube1_2_2@1"
side_def 23308 "(+)cube1_2_3/(-)cube1_1_3@1"
side_def 23320 "(+)cube1_2_3/(-)cube1_2_2@1"
side_def 23489 "(+)Universe/(-)cube1_2_1@1"
side_def 23881 "(+)cube1_2_2/(-)cube1_1_2@1"
side_def 23893 "(+)cube1_2_2/(-)cube1_2_1@1"
side_def 24062 "(+)Universe/(-)cube1_1_1@1"
side_def 24069 "(+)Universe/(-)cube1_1_1@2"
side_def 24470 "(+)cube1_2_1/(-)cube1_1_1@1"
side_def 24652 "(+)Universe/(-)cube1_1_4@3"
```

```
      side_def 24659 "(+)Universe/(-)cube1_1_4@2"
      side_def 25073 "(+)cube1_1_4/(-)cube1_1_3@1"
      side_def 25248 "(+)Universe/(-)cube1_1_3@1"
      side_def 25255 "(+)Universe/(-)cube1_1_3@2"
      side_def 25674 "(+)cube1_1_3/(-)cube1_1_2@1"
      side_def 25850 "(+)Universe/(-)cube1_1_2@1"
      side_def 25857 "(+)Universe/(-)cube1_1_2@2"
      side_def 26281 "(+)cube1_1_2/(-)cube1_1_1@1"

   material_definition_block
      material_def 1 "Poly" 0
      material_def 2 "Air" 0
      material_comp 1 16 0.333
      material_comp 1 47 0.667
      material_comp 2 61 0.99632
      material_comp 2 62 0.00368

   cross_section_block
      nparticle 1
      nfine_groups 79
      xsfile_format dtf
      isotope_def 16 0 "c" 0
      isotope_def 47 0 "h1(ch2)" 0
      isotope_def 61 0 "n14" 0
      isotope_def 62 0 "n15" 0
      edit_xs_def 1 "absorption"
      edit_xs_def 2 "nu-fission"

   end_rtt_attila_input
```

APPENDIX B

Radion15, SCALE44 and Kynea3 Group Structure

Table 22. Comparison of Radion15, SCALE44 and Kynea3 Neutron Energy Group Structure.

Group #	Radion15 Group Boundary (MeV)	SCALE44 Group Boundary (MeV)	Kynea3 Group Boundary (MeV)
1	2.00E+01 – 1.50E+01	2.00E+01 – 8.19E+00	1.73E+01 – 1.96E+01
2	1.50E+01 – 1.20E+01	8.19E+00 – 6.43E+00	1.42E+01 – 1.73E+01
3	1.20E+01 – 1.00E+01	6.43E+00 – 4.80E+00	1.22E+01 – 1.42E+01
4	1.00E+01 – 7.79E+00	4.80E+00 – 3.00E+00	1.00E+01 – 1.22E+01
5	7.79E+00 – 6.07E+00	3.00E+00 – 2.48E+00	8.61E+00 – 1.00E+01
6	6.07E+00 – 4.72E+00	2.48E+00 – 2.35E+00	7.41E+00 – 8.61E+00
7	4.72E+00 – 3.68E+00	2.35E+00 – 1.85E+00	6.07E+00 – 7.41E+00
8	3.68E+00 – 2.87E+00	1.85E+00 – 1.40E+00	4.97E+00 – 6.07E+00
9	2.87E+00 – 2.23E+00	1.40E+00 – 9.00E-01	3.68E+00 – 4.97E+00
10	2.23E+00 – 1.74E+00	9.00E-01 – 4.00E-01	3.01E+00 – 3.68E+00
11	1.74E+00 – 1.19E+00	4.00 E-01 – 1.00E-01	2.73E+00 – 3.01E+00
12	1.19E+00 – 8.21E-01	1.00 E-01 – 2.50E-02	2.47E+00 – 2.73E+00
13	8.21E-01 – 2.35E-01	2.50E-02 – 1.70E-02	2.37E+00 – 2.47E+00
14	2.35E-01 – 6.74E-02	1.70E-02 – 3.00E-03	2.35E+00 – 2.37E+00
15	6.74E-02 – 1.93E-02	3.00E-03 – 5.50E-04	2.23E+00 – 2.35E+00
16	1.93E-02 – 5.53E-03	5.50E-04 – 1.00E-04	1.92E+00 – 2.23E+00
17	5.53E-03 – 3.54E-04	1.00E-04 – 3.00E-05	1.65E+00 – 1.92E+00
18	3.54E-04 – 2.26E-05	3.00E-05 – 1.00E-05	1.35E+00 – 1.65E+00
19	2.26E-05 – 3.47E-06	1.00E-05 – 8.10E-06	1.00E+00 – 1.35E+00
20	3.47E-06 – 6.25E-07	8.10E-06 – 6.00E-06	8.21E-01 – 1.00E+00
21	6.25E-07 – 1.24E-08	6.00E-06 – 4.75E-06	7.43E-01 – 8.21E-01
22	1.24E-08 –1.00E-11	4.75E-06 – 3.00E-06	6.08E-01 – 7.43E-01
23	-----------------------	3.00E-06 – 1.77E-06	4.98E-01 – 6.08E-01
24	-----------------------	1.77E-06 – 1.00E-06	3.69E-01 – 4.98E-01
25	-----------------------	1.00E-06 – 6.25E-07	2.97E-01 – 3.69E-01
26	-----------------------	6.25E-07 – 4.00E-07	1.83E-01 – 2.97E-01
27	-----------------------	4.00E-07 – 3.75E-07	1.11E-01 – 1.83E-01
28	-----------------------	3.75E-07 – 3.50E-07	6.74E-02 – 1.11E-01
29	-----------------------	3.50E-07 – 3.25E-07	4.09E-02 – 6.74E-02
30	-----------------------	3.25E-07 – 2.75E-07	3.18E-02 – 4.09E-02
31	-----------------------	2.75E-07 – 2.50E-07	2.61E-02 – 3.18E-02
32	-----------------------	2.50E-07 – 2.25E-07	2.42E-02 – 2.61E-02
33	-----------------------	2.25E-07 – 2.00E-07	2.19E-02 – 2.42E-02
34	-----------------------	2.00E-07 – 1.50E-07	1.50E-02 – 2.19E-02

Table 22 Cont.

Group #	Radion15 Group Boundary (MeV)	SCALE44 Group Boundary (MeV)	Kynea3 Group Boundary (MeV)
35	------------------------	1.50E-07 – 1.00E-07	7.10E-03 – 1.50E-02
36	------------------------	1.00E-07 – 7.00E-08	3.35E-03 – 7.10E-03
37	------------------------	7.00E-08– 5.00E-08	1.58E-03 – 3.35E-03
38	------------------------	5.00E-08 – 4.00E-08	4.54E-04 – 1.58E-03
39	------------------------	4.00E-08 – 3.00E-08	2.14E-04 – 4.54E-04
40	------------------------	3.00E-08 – 2.53E-08	1.01E-04 – 2.14E-04
41	------------------------	2.53E-08 – 1.00E-08	3.73E-05 – 1.01E-04
42	------------------------	1.00E-08 – 7.50E-09	1.07E-05 – 3.73E-05
43	------------------------	7.50E-09 – 3.00E-09	5.04E-06 – 1.07E-05
44	------------------------	3.00E-09 – 1.00E-11	3.93E-06 – 5.04E-06
45	------------------------	------------------------	3.06E-06 – 3.93E-06
46	------------------------	------------------------	2.38E-06 – 3.06E-06
47	------------------------	------------------------	1.86E-06 – 2.38E-06
48	------------------------	------------------------	1.45E-06 – 1.86E-06
49	------------------------	------------------------	1.30E-06 – 1.45E-06
50	------------------------	------------------------	1.13E-06 – 1.30E-06
51	------------------------	------------------------	1.08E-06 – 1.13E-06
52	------------------------	------------------------	1.04E-06 – 1.08E-06
53	------------------------	------------------------	1.00E-06 – 1.04E-06
54	------------------------	------------------------	8.76E-07 – 1.00E-06
55	------------------------	------------------------	8.00E-07 – 8.76E-07
56	------------------------	------------------------	6.83E-07 – 8.00E-07
57	------------------------	------------------------	6.25E-07 – 6.83E-07
58	------------------------	------------------------	5.32E-07 – 6.25E-07
59	------------------------	------------------------	5.00E-07 – 5.32E-07
60	------------------------	------------------------	4.14E-07 – 5.00E-07
61	------------------------	------------------------	3.67E-07 – 4.14E-07
62	------------------------	------------------------	3.25E-07 – 3.67E-07
63	------------------------	------------------------	2.75E-07 – 3.25E-07
64	------------------------	------------------------	2.25E-07 – 2.75E-07
65	------------------------	------------------------	1.84E-07 – 2.25E-07
66	------------------------	------------------------	1.50E-07 – 1.84E-07
67	------------------------	------------------------	1.25E-07 – 1.50E-07
68	------------------------	------------------------	1.00E-07 – 1.25E-07
69	------------------------	------------------------	7.00E-08 – 1.00E-07
70	------------------------	------------------------	5.00E-08 – 7.00E-08
71	------------------------	------------------------	4.00E-08 – 5.00E-08
72	------------------------	------------------------	3.00E-08 – 4.00E-08
73	------------------------	------------------------	2.10E-08 – 3.00E-08
74	------------------------	------------------------	1.45E-08 – 2.10E-08
75	------------------------	------------------------	1.00E-08 – 1.45E-08
76	------------------------	------------------------	5.00E-09 – 1.00E-08

Table 22 Cont.

Group #	Radion15 Group Boundary (MeV)	SCALE44 Group Boundary (MeV)	Kynea3 Group Boundary (MeV)
77	-------------------------	-------------------------	2.00E-09 – 5.00E-09
78	-------------------------	-------------------------	5.00E-10 – 2.00E-09
79	-------------------------	-------------------------	1.00E-11 – 5.00E-10

RadSat (n, gamma) Trial - MCNP Version
c
c Cell Cards
c
c Germanium Detector
c
c Germanium Crystal
c
1   32 -5.32 (((2 -4 -5)(-2 :7 :8))(10 :-8)) &
            (-12 :4 :5)   imp:n=1 imp:p=1 $ Active crystal volume
2   32 -5.32 ((((2 -4 -3 5):(-1 4 -3))(1 :3 :-11)): &
            (12 -4 -5))(-11 :5 :4)   imp:n=1 imp:p=1 $ Outer [P] Dead Layer
3   32 -5.32 (2 -8 6 -7):(9 -10 8)   imp:n=1 imp:p=1 $ Inner [N] Dead Layer
c
c Detector Cup Assembly
c
4   13 -2.70   (-61 30 -31 32):(-32 33 -31) imp:n=1 imp:p=1 $ Al Inner Can Side and
bottom
5   13 -2.70   (31 -34 -35 36)   imp:n=1 imp:p=1 $ Al Inner Can top ring
6   13 -2.70   (31 -34 -37 38)   imp:n=1 imp:p=1 $ Al Inner Can bottom ring
7   7 -1.01   (61 -60 -34):(31 -34 63 -61) imp:n=1 imp:p=1 $ Thin Inner Can cap
c
c End Cap
c
8   13 -2.70   (84 -85 -82)   imp:n=1 imp:p=1 $ Al EndCap Window
9   13 -2.70   (82 -83 -85 81):(-80 81 -82) imp:n=1 imp:p=1 $ Al EndCap
c
c Vacuum
c
10   0 (-6 -8 2):(-9 8)   imp:n=1 imp:p=1 $ Vacuum
11   0 ((-2 32 -30):(2 -1 3 -30)):(1 -61 -30) imp:n=1 imp:p=1 $ Vacuum
12   0 (-33 80 -82)   imp:n=1 imp:p=1 $ Vacuum
13   0 (60 -84 -82):(34 -82 -60 33)   imp:n=1 imp:p=1 $ Vacuum
14   0 (31 -34 35 -63)   imp:n=1 imp:p=1 $ Vacuum
15   0 (31 -34 -36 37)   imp:n=1 imp:p=1 $ Vacuum
16   0 (-34 31 -38 33)   imp:n=1 imp:p=1 $ Vacuum
17   0 (11 -1 -3)   imp:n=1 imp:p=1 $ Vacuum
c

```
18   13  -2.70   -200 201 -202          imp:n=1 imp:p=1 $ Rear section of collimator
19   13  -2.70   -205 201  202 -203      imp:n=1 imp:p=1 $ Cylindrical wall of
collimator
20   200 -1.05   -202 204 -205          imp:n=1 imp:p=1 $ Plastic cap on front of
sensor
21   2  -1.205E-3 -201 301 302 -303 304 -305   imp:n=1 imp:p=1 $ Housing (batteries,
etc.) behind sensor
c
c Remainder of Problem
c
501  1  -0.5   -501                imp:n=1 imp:p=1 $ C2H4 Box
502  2  -1.205E-3 -502             imp:n=1 imp:p=1 $ Air for Cf-252 Source
900  2  -1.205E-3 -999(85:-81:83) #18 #19 #20 &
          #21 #501 #502            imp:n=1 imp:p=1 $ Air Around Box
999  0      999                imp:n=0 imp:p=0 $ Vacuum
c

c Surface Cards
c
c
c Coaxial Germanium Detector Surface Definition Cards
c
c Germanium Crystal
c
1  101  pz    -0.600 $ Top face of outer dead layer
2  101  pz    -3.470 $ Bottom face of active volume (~2.7 cm thick below bottom of
dead layer (surface 4))
3  101  cz    2.500 $ Outer radius of outer dead layer
4  101  pz    -0.670 $ Bottom face of outer dead layer (0.7 mm thick), top face of active
volume
5  101  cz    2.270 $ Outer radius of active volume
6  101  cz    0.500 $ Radius of inner hole
7  101  cz    0.570 $ Radius of inner dead layer
8  101  pz    -2.500 $ Top of inner cylinder
9  101  sz    -2.500   0.5 $ Round the bottom of the hole
10  101  sz   -2.500   0.57 $ Round the bottom of the dead layer
11  101  kz    1.620   1.0  -1 $ Knock corners off dead layer
12  101  kz    1.480   1.0  -1 $ Knock corners off Ge Core crystal
c
c  Cone that can be used to simulate additional 'features'
c 13  101  kz    -1186.  1.0e-005    1 $ Additional Dead Layer
c
c Detector Cup
c
30  101  cz    2.501 $ Inner wall radius
31  101  cz    2.551 $ Outer wall radius
```

```
32  101  pz   -4.800 $ Inside [top] of bottom piece
33  101  pz   -5.000 $ Outside [bottom] of bottom piece
34  101  cz    2.650 $ Outer screw Flange radius
35  101  pz   -1.590 $ Top of top screw Flange
36  101  pz   -2.090 $ Bottom of top screw flange
37  101  pz   -2.580 $ Top of bottom screw Flange
38  101  pz   -3.080 $ Bottom of bottom screw flange
c
c Cap for Detector Cup
c
60  101  pz   -0.570 $ Outer face
61  101  pz   -0.599 $ Inner face, top of detector cup
63  101  pz   -0.900 $ Lower extent of cap
c
c End Cap and End Cap Window
c
80  101  pz   -7.000 $ Inside Lower bound of detector end cap
81  101  pz   -7.100 $ Outside Lower bound of detector end cap
82  101  cz    3.150 $ Inside radius of end cap
83  101  cz    3.250 $ Outside radius of end cap
84  101  pz   -0.100 $ Inside detector Face (Window)
85  101  pz    0.000 $ Outside detector face (Window)
c
c Collimator around detector crystal
200 101  pz   -7.1  $ front face of rear section
201 101  pz   -7.4  $ back face of rear section
202 101  cz    3.25 $ inside of collimator wall
203 101  cz    3.55 $ outside of collimator wall
204 101  pz    0.0  $ front surface of collimator wall
205 101  pz    0.2  $ front face of front section
c
c Remainder of Problem
c
501   rpp -10 10 -10 10 -10 10          $ C2H4 Box
c
502   box -15  -0.25 -0.25
      -0.5   0    0
       0   0.5    0
       0    0   0.5              $ Cf-252 Source
c
999   rpp -16.5 31 -11.5 11.5 -11.5 11.5    $ Problem Boundary
c

c *************************** Data cards
***************************
c
```

```
Mode n p
c
c Translation Card
c Moves detector 5 centemeters off +x face of cube
*tr101 15.2 0 0    90 90   0   90   0   90  $ rotate from +z to -x
c
c SDEF Cards
c
sdef  erg=d1  par=1  x=d2 y=d3 z=d4 vec=1 0 0 dir=d5
sp1   -3 1.025 2.926
si2   -15.499 -15.001
sp2   0 1
si3   -0.249 0.249
sp3   0 1
si4   -0.249 0.249
sp4   0 1
si5   0 1
sp5   0 1
c
c Tally Definition Cards
c
F4:p 1                        $ Photon Tally in Detector
E4 0  0.05 3000I 7              $ Photon Energy Bins
c
F14:n 501                      $ Neutron Flux in Box (79 Group)
E14  1.0000E-11 5.0000E-10 2.0000E-09 5.0000E-09 1.0000E-08 1.4500E-08
     2.1000E-08 3.0000E-08 4.0000E-08 5.0000E-08 7.0000E-08 1.0000E-07
     1.2500E-07 1.5000E-07 1.8400E-07 2.2500E-07 2.7500E-07 3.2500E-07
     3.6680E-07 4.1399E-07 5.0000E-07 5.3158E-07 6.2506E-07 6.8256E-07
     8.0000E-07 8.7643E-07 1.0000E-06 1.0400E-06 1.0800E-06 1.1253E-06
     1.3000E-06 1.4450E-06 1.8554E-06 2.3824E-06 3.0590E-06 3.9279E-06
     5.0435E-06 1.0677E-05 3.7266E-05 1.0130E-04 2.1445E-04 4.5400E-04
     1.5846E-03 3.3546E-03 7.1017E-03 1.5034E-02 2.1875E-02 2.4176E-02
     2.6058E-02 3.1828E-02 4.0868E-02 6.7379E-02 1.1109E-01 1.8316E-01
     2.9721E-01 3.6883E-01 4.9787E-01 6.0810E-01 7.4274E-01 8.2085E-01
     1.0026E+00 1.3534E+00 1.6530E+00 1.9205E+00 2.2313E+00 2.3457E+00
     2.3653E+00 2.4660E+00 2.7253E+00 3.0119E+00 3.6788E+00 4.9659E+00
     6.0653E+00 7.4082E+00 8.6071E+00 1.0000E+01 1.2214E+01 1.4191E+01
     1.7332E+01 1.9640E+01
c
F24:n 501                      $ Neutron Tally in C2H4
c
C Reaction Rate Card
FM24   (4.2934e-2  3 102)          $ Radiative Capture in H-1
     (4.9379e-6  4 102)          $ Radiative Capture in H-2
     (2.1467e-2  5 102)          $ Radiative Capture in C
```

```
        (2.1467e-2  5 51)              $ Inelastic Scatter in C
c
fc8  Detective (13% HPGe) pulse-height tally
f8:p  (1 3)   $ Pulse Height tally on cells (1 3) for a P-Type, or (1 2) for an
c  Gaussian Energy Broadening Term
ft8 geb 0.0028  0.0008  0  $ for Ge
e8 0 1e-5 10000I 11
c
c Material Cards
c
m1    1001  -0.143718
      6000  -0.856282            $ C2H4
mt1   poly.60t
c
m2    7014  0.99632
      7015  0.00368             $ Air, den=0.001205 g/cc
c
m7    6000  1            $ Carbon, den=1.01 g/cc
c
m13   13027  1             $ Aluminum, den=2.70 g/cc
c
m32   32070  0.2084             $ Germanium, den=5.32 g/cc
      32072  0.2754
      32073  0.0773
      32074  0.3628
      32076  0.0761
c
m200  1001 -0.085 $ H    Homogenized mix of plastic and Aluminum (Detector Housing)
      6000 -0.915 $ C
     13027 -1    $ Al
c
c Materials for tallies
c
m3    1001  1            $ H-1
m4    1002  1            $ H-2
m5    6000  1            $ Carbon
c
phys:p 100 0 0 0 1
c
nps  8.88E10
c
rand gen=2 seed=508645327 stride=258685
```

APPENDIX D

Summary of NJOY99.259 Modules Used in Calculations

The MODER module is purely a formatting routine that is used within NJOY to convert files to binary and vice versa [3]. The MODER module was used to convert the ENDF file into the binary format used by NJOY for computation procedures within the code.

RECONR module was used to reconstruct pointwise cross-sections from the resonance parameters and interpolation schemes in the ENDF/B format. The RECONR module in NJOY produces pointwise cross sections on a union energy grid that is suitable for linear interpolation in the PENDF format [3]. Additionally the summation cross sections, such as the total and inelastic, "are reconstructed to be exactly equal to the sum of their parts at all energies.

BROADR module was used to calculate the Doppler broadening of the pointwise PENDF cross sections. The method employed by the BROADR module is often referred to as "kernel broadening" since "it uses a detailed integration of the integral equation defining the effective cross section. It is a fully accurate method, treating all resonance and nonresonance cross sections including multilevel effects." [3]

UNRESR module was used to produce the effective self-shielded pointwise cross section in the unresolved resonance range using the resonance parameters in the ENDF files. Although none of the elements included in this project include unresolved resonances, it does not hurt to include this subroutine in the input file. Since there are no unresolved resonance parameters in the ENDF files, the subroutine does not perform a

function but acts as a place holder for future NJOY runs which could contain unresolved resonance features.

ACER module was used to produce a point-wise cross-section file (of the form used by MCNP5). The ACER module was key to the process because the file it produces contains separate cross-sections for the production of discrete gamma rays and for continuum photons. Both are provided on a single union energy grid suitable for linear interpolation, making subsequent collapsing relatively straightforward. No data points were removed using the ACER subroutine. It was used merely as a formatting routine to convert the PENDF file, an internal file used by NJOY, to a file more easily collapsed.

GROUPR module was used to produce photon production matrices from ENDF/B-VI data. The Bondarenko narrow-resonance flux weighting approximation [3] was used for all calculations.

APPENDIX E

NJOY99.259 Input File to Produce ACER file for Hydrogen

```
moder / Convert data to binary on Unit-21
 1 -21
 'ENDF/B-VI H-1' /
 20 125
 0 /
 reconr / Reconstruct x-sect from resonance parameters on Unit-22
 -21 -22
 'PENDF TAPR FOR H-1 FROM ENDF/B-VI' /
 125 2 /
 0.001  0.0  0.005 / Reconstruction 0.1% (0.5% max)
 '1-H-1 FROM ENDF/B-VI '/
 'PROCESSED BY NJOY-99 '/
 0 /
 broadr / Doppler broadening to Unit-23
 -21 -22 -23
 125 1 0 0 0 /
 0.001/
 300./
 0/
 unresr / Does not do any harm if no unresolved res
 -21 -23 -24
 125 1 4 1
 300.
 1.E10 1.E6 1.E3 10.
 0 /
acer
 -21 -26 0 25 27
 1 1 1/
 'acer run for h-1'/
 125  /
 0/
 /
 stop
```

APPENDIX F

RADSAT-NG Cross Section Example Format

ZAID

*********************Discrete*******************

$E_{\gamma 1}$ (MeV)

σ_{g1}	σ_{g2}	σ_{g3}	σ_{g4}	σ_{g5}	σ_{g6}
σ_{g7}	σ_{g8}	σ_{g9}	σ_{g10}	σ_{g11}	σ_{g12}
$_{g13}$	σ_{g14}	σ_{g15}	σ_{g16}	σ_{g17}	σ_{g18}
σ_{g19}	σ_{g20}	σ_{g21}	σ_{g22}	σ_{g23}	σ_{g24}
σ_{g25}	σ_{g26}	σ_{g27}	σ_{g28}	σ_{g29}	σ_{g30}
σ_{g31}	σ_{g32}	σ_{g33}	σ_{g34}	σ_{g35}	σ_{g36}
σ_{g37}	σ_{g38}	σ_{g39}	σ_{g40}	σ_{g41}	σ_{g42}
σ_{g43}	σ_{g44}	σ_{g45}	σ_{g46}	σ_{g47}	σ_{g48}
σ_{g49}	σ_{g50}	σ_{g51}	σ_{g52}	σ_{g53}	σ_{g54}
σ_{g55}	σ_{g56}	σ_{g57}	σ_{g58}	σ_{g59}	σ_{g60}
σ_{g61}	σ_{g62}	σ_{g63}	σ_{g64}	σ_{g65}	σ_{g66}
σ_{g67}	σ_{g68}	σ_{g69}	σ_{g70}	σ_{g71}	σ_{g72}
σ_{g73}	σ_{g74}	σ_{g75}	σ_{g76}	σ_{g77}	σ_{g78}
σ_{g79}					

$E_{\gamma 2}$ (MeV)

σ_{g1}	σ_{g2}	σ_{g3}	σ_{g4}	σ_{g5}	σ_{g6}
σ_{g7}	σ_{g8}	σ_{g9}	σ_{g10}	σ_{g11}	σ_{g12}
σ_{g13}	σ_{g14}	σ_{g15}	σ_{g16}	σ_{g17}	σ_{g18}
σ_{g19}	σ_{g20}	σ_{g21}	σ_{g22}	σ_{g23}	σ_{g24}
σ_{g25}	σ_{g26}	σ_{g27}	σ_{g28}	σ_{g29}	σ_{g30}
σ_{g31}	σ_{g32}	σ_{g33}	σ_{g34}	σ_{g35}	σ_{g36}
σ_{g37}	σ_{g38}	σ_{g39}	σ_{g40}	σ_{g41}	σ_{g42}
σ_{g43}	σ_{g44}	σ_{g45}	σ_{g46}	σ_{g47}	σ_{g48}
σ_{g49}	σ_{g50}	σ_{g51}	σ_{g52}	σ_{g53}	σ_{g54}
σ_{g55}	σ_{g56}	σ_{g57}	σ_{g58}	σ_{g59}	σ_{g60}
σ_{g61}	σ_{g62}	σ_{g63}	σ_{g64}	σ_{g65}	σ_{g66}
σ_{g67}	σ_{g68}	σ_{g69}	σ_{g70}	σ_{g71}	σ_{g72}
σ_{g73}	σ_{g74}	σ_{g75}	σ_{g76}	σ_{g77}	σ_{g78}
σ_{g79}					

$E_{\gamma 3}$ (MeV)

σ_{g1}	σ_{g2}	σ_{g3}	σ_{g4}	σ_{g5}	σ_{g6}
σ_{g7}	σ_{g8}	σ_{g9}	σ_{g10}	σ_{g11}	σ_{g12}
σ_{g13}	σ_{g14}	σ_{g15}	σ_{g16}	σ_{g17}	σ_{g18}

$\sigma_{g}19$	$\sigma_{g}20$	$\sigma_{g}21$	$\sigma_{g}22$	$\sigma_{g}23$	$\sigma_{g}24$
$\sigma_{g}25$	$\sigma_{g}26$	$\sigma_{g}27$	$\sigma_{g}28$	$\sigma_{g}29$	$\sigma_{g}30$
$\sigma_{g}31$	$\sigma_{g}32$	$\sigma_{g}33$	$\sigma_{g}34$	$\sigma_{g}35$	$\sigma_{g}36$
$\sigma_{g}37$	$\sigma_{g}38$	$\sigma_{g}39$	$\sigma_{g}40$	$\sigma_{g}41$	$\sigma_{g}42$
$\sigma_{g}43$	$\sigma_{g}44$	$\sigma_{g}45$	$\sigma_{g}46$	$\sigma_{g}47$	$\sigma_{g}48$
$\sigma_{g}49$	$\sigma_{g}50$	$\sigma_{g}51$	$\sigma_{g}52$	$\sigma_{g}53$	$\sigma_{g}54$
$\sigma_{g}55$	$\sigma_{g}56$	$\sigma_{g}57$	$\sigma_{g}58$	$\sigma_{g}59$	$\sigma_{g}60$
$\sigma_{g}61$	$\sigma_{g}62$	$\sigma_{g}63$	$\sigma_{g}64$	$\sigma_{g}65$	$\sigma_{g}66$
$\sigma_{g}67$	$\sigma_{g}68$	$\sigma_{g}69$	$\sigma_{g}70$	$\sigma_{g}71$	$\sigma_{g}72$
$\sigma_{g}73$	$\sigma_{g}74$	$\sigma_{g}75$	$\sigma_{g}76$	$\sigma_{g}77$	$\sigma_{g}78$
$\sigma_{g}79$					

*********************Continuum********************

Continuum

$\sigma_{g}1{\rightarrow}p1$	$\sigma_{g}2{\rightarrow}p1$	$\sigma_{g}3{\rightarrow}p1$	$\sigma_{g}4{\rightarrow}p1$	$\sigma_{g}5{\rightarrow}p1$	$\sigma_{g}6{\rightarrow}p1$
$\sigma_{g}7{\rightarrow}p1$	$\sigma_{g}8{\rightarrow}p1$	$\sigma_{g}9{\rightarrow}p1$	$\sigma_{g}10{\rightarrow}p1$	$\sigma_{g}11{\rightarrow}p1$	$\sigma_{g}12{\rightarrow}p1$
$\sigma_{g}13{\rightarrow}p1$	$\sigma_{g}14{\rightarrow}p1$	$\sigma_{g}15{\rightarrow}p1$	$\sigma_{g}16{\rightarrow}p1$	$\sigma_{g}17{\rightarrow}p1$	$\sigma_{g}18{\rightarrow}p1$
$\sigma_{g}19{\rightarrow}p1$	$\sigma_{g}20{\rightarrow}p1$	$\sigma_{g}21{\rightarrow}p1$	$\sigma_{g}22{\rightarrow}p1$	$\sigma_{g}23{\rightarrow}p1$	$\sigma_{g}24{\rightarrow}p1$
$\sigma_{g}25{\rightarrow}p1$	$\sigma_{g}26{\rightarrow}p1$	$\sigma_{g}27{\rightarrow}p1$	$\sigma_{g}28{\rightarrow}p1$	$\sigma_{g}29{\rightarrow}p1$	$\sigma_{g}30{\rightarrow}p1$
$\sigma_{g}31{\rightarrow}p1$	$\sigma_{g}32{\rightarrow}p1$	$\sigma_{g}33{\rightarrow}p1$	$\sigma_{g}34{\rightarrow}p1$	$\sigma_{g}35{\rightarrow}p1$	$\sigma_{g}36{\rightarrow}p1$
$\sigma_{g}37{\rightarrow}p1$	$\sigma_{g}38{\rightarrow}p1$	$\sigma_{g}39{\rightarrow}p1$	$\sigma_{g}40{\rightarrow}p1$	$\sigma_{g}41{\rightarrow}p1$	$\sigma_{g}42{\rightarrow}p1$
$\sigma_{g}43{\rightarrow}p1$	$\sigma_{g}44{\rightarrow}p1$	$\sigma_{g}45{\rightarrow}p1$	$\sigma_{g}46{\rightarrow}p1$	$\sigma_{g}47{\rightarrow}p1$	$\sigma_{g}48{\rightarrow}p1$
$\sigma_{g}49{\rightarrow}p1$	$\sigma_{g}50{\rightarrow}p1$	$\sigma_{g}51{\rightarrow}p1$	$\sigma_{g}52{\rightarrow}p1$	$\sigma_{g}53{\rightarrow}p1$	$\sigma_{g}54{\rightarrow}p1$
$\sigma_{g}55{\rightarrow}p1$	$\sigma_{g}56{\rightarrow}p1$	$\sigma_{g}57{\rightarrow}p1$	$\sigma_{g}58{\rightarrow}p1$	$\sigma_{g}59{\rightarrow}p1$	$\sigma_{g}60{\rightarrow}p1$
$\sigma_{g}61{\rightarrow}p1$	$\sigma_{g}62{\rightarrow}p1$	$\sigma_{g}63{\rightarrow}p1$	$\sigma_{g}64{\rightarrow}p1$	$\sigma_{g}65{\rightarrow}p1$	$\sigma_{g}66{\rightarrow}p1$
$\sigma_{g}67{\rightarrow}p1$	$\sigma_{g}68{\rightarrow}p1$	$\sigma_{g}69{\rightarrow}p1$	$\sigma_{g}70{\rightarrow}p1$	$\sigma_{g}71{\rightarrow}p1$	$\sigma_{g}72{\rightarrow}p1$
$\sigma_{g}73{\rightarrow}p1$	$\sigma_{g}74{\rightarrow}p1$	$\sigma_{g}75{\rightarrow}p1$	$\sigma_{g}76{\rightarrow}p1$	$\sigma_{g}77{\rightarrow}p1$	$\sigma_{g}78{\rightarrow}p1$
$\sigma_{g}79{\rightarrow}p1$	$\sigma_{g}1{\rightarrow}p2$	$\sigma_{g}2{\rightarrow}p2$	$\sigma_{g}3{\rightarrow}p2$	$\sigma_{g}4{\rightarrow}p2$	$\sigma_{g}5{\rightarrow}p2$
$\sigma_{g}6{\rightarrow}p2$	$\sigma_{g}7{\rightarrow}p2$	$\sigma_{g}8{\rightarrow}p2$	$\sigma_{g}9{\rightarrow}p2$	$\sigma_{g}10{\rightarrow}p2$	$\sigma_{g}11{\rightarrow}p2$
$\sigma_{g}12{\rightarrow}p2$	$\sigma_{g}13{\rightarrow}p2$	$\sigma_{g}14{\rightarrow}p2$	$\sigma_{g}15{\rightarrow}p2$	$\sigma_{g}16{\rightarrow}p2$	$\sigma_{g}17{\rightarrow}p2$
$\sigma_{g}18{\rightarrow}p2$	$\sigma_{g}19{\rightarrow}p2$	$\sigma_{g}20{\rightarrow}p2$	$\sigma_{g}21{\rightarrow}p2$	$\sigma_{g}22{\rightarrow}p2$	$\sigma_{g}23{\rightarrow}p2$
$\sigma_{g}24{\rightarrow}p2$	$\sigma_{g}25{\rightarrow}p2$	$\sigma_{g}26{\rightarrow}p2$	$\sigma_{g}27{\rightarrow}p2$	$\sigma_{g}28{\rightarrow}p2$	$\sigma_{g}29{\rightarrow}p2$
$\sigma_{g}30{\rightarrow}p2$	$\sigma_{g}31{\rightarrow}p2$	$\sigma_{g}32{\rightarrow}p2$	$\sigma_{g}33{\rightarrow}p2$	$\sigma_{g}34{\rightarrow}p2$	$\sigma_{g}35{\rightarrow}p2$
$\sigma_{g}36{\rightarrow}p2$	$\sigma_{g}37{\rightarrow}p2$	$\sigma_{g}38{\rightarrow}p2$	$\sigma_{g}39{\rightarrow}p2$	$\sigma_{g}40{\rightarrow}p2$	$\sigma_{g}41{\rightarrow}p2$
$\sigma_{g}42{\rightarrow}p2$	$\sigma_{g}43{\rightarrow}p2$	$\sigma_{g}44{\rightarrow}p2$	$\sigma_{g}45{\rightarrow}p2$	$\sigma_{g}46{\rightarrow}p2$	$\sigma_{g}47{\rightarrow}p2$
$\sigma_{g}48{\rightarrow}p2$	$\sigma_{g}49{\rightarrow}p2$	$\sigma_{g}50{\rightarrow}p2$	$\sigma_{g}51{\rightarrow}p2$	$\sigma_{g}52{\rightarrow}p2$	$\sigma_{g}53{\rightarrow}p2$
$\sigma_{g}54{\rightarrow}p2$	$\sigma_{g}55{\rightarrow}p2$	$\sigma_{g}56{\rightarrow}p2$	$\sigma_{g}57{\rightarrow}p2$	$\sigma_{g}58{\rightarrow}p2$	$\sigma_{g}59{\rightarrow}p2$
$\sigma_{g}60{\rightarrow}p2$	$\sigma_{g}61{\rightarrow}p2$	$\sigma_{g}62{\rightarrow}p2$	$\sigma_{g}63{\rightarrow}p2$	$\sigma_{g}64{\rightarrow}p2$	$\sigma_{g}65{\rightarrow}p2$
$\sigma_{g}66{\rightarrow}p2$	$\sigma_{g}67{\rightarrow}p2$	$\sigma_{g}68{\rightarrow}p2$	$\sigma_{g}69{\rightarrow}p2$	$\sigma_{g}70{\rightarrow}p2$	$\sigma_{g}71{\rightarrow}p2$
$\sigma_{g}72{\rightarrow}p2$	$\sigma_{g}73{\rightarrow}p2$	$\sigma_{g}74{\rightarrow}p2$	$\sigma_{g}75{\rightarrow}p2$	$\sigma_{g}76{\rightarrow}p2$	$\sigma_{g}77{\rightarrow}p2$
$\sigma_{g}78{\rightarrow}p2$	$\sigma_{g}79{\rightarrow}p2$	$\sigma_{g}1{\rightarrow}pn$	$\sigma_{g}2{\rightarrow}pn$	$\sigma_{g}3{\rightarrow}pn$	$\sigma_{g}4{\rightarrow}pn$
$\sigma_{g}5{\rightarrow}pn$	$\sigma_{g}6{\rightarrow}pn$	$\sigma_{g}7{\rightarrow}pn$	$\sigma_{g}8{\rightarrow}pn$	$\sigma_{g}9{\rightarrow}pn$	$\sigma_{g}10{\rightarrow}pn$
$\sigma_{g}11{\rightarrow}pn$	$\sigma_{g}12{\rightarrow}pn$	$\sigma_{g}13{\rightarrow}pn$	$\sigma_{g}14{\rightarrow}pn$	$\sigma_{g}15{\rightarrow}pn$	$\sigma_{g}16{\rightarrow}pn$
$\sigma_{g}17{\rightarrow}pn$	$\sigma_{g}18{\rightarrow}pn$	$\sigma_{g}19{\rightarrow}pn$	$\sigma_{g}20{\rightarrow}pn$	$\sigma_{g}21{\rightarrow}pn$	$\sigma_{g}22{\rightarrow}pn$
$\sigma_{g}23{\rightarrow}pn$	$\sigma_{g}24{\rightarrow}pn$	$\sigma_{g}25{\rightarrow}pn$	$\sigma_{g}26{\rightarrow}pn$	$\sigma_{g}27{\rightarrow}pn$	$\sigma_{g}28{\rightarrow}pn$

$\sigma_{g29} \rightarrow pn$ $\sigma_{g30} \rightarrow pn$ $\sigma_{g31} \rightarrow pn$ $\sigma_{g32} \rightarrow pn$ $\sigma_{g33} \rightarrow pn$ $\sigma_{g34} \rightarrow pn$

$\sigma_{g35} \rightarrow pn$ $\sigma_{g36} \rightarrow pn$ $\sigma_{g37} \rightarrow pn$ $\sigma_{g38} \rightarrow pn$ $\sigma_{g39} \rightarrow pn$ $\sigma_{g40} \rightarrow pn$

$\sigma_{g41} \rightarrow pn$ $\sigma_{g42} \rightarrow pn$ $\sigma_{g43} \rightarrow pn$ $\sigma_{g44} \rightarrow pn$ $\sigma_{g45} \rightarrow pn$ $\sigma_{g46} \rightarrow pn$

$\sigma_{g47} \rightarrow pn$ $\sigma_{g48} \rightarrow pn$ $\sigma_{g49} \rightarrow pn$ $\sigma_{g50} \rightarrow pn$ $\sigma_{g51} \rightarrow pn$ $\sigma_{g52} \rightarrow pn$

$\sigma_{g53} \rightarrow pn$ $\sigma_{g54} \rightarrow pn$ $\sigma_{g55} \rightarrow pn$ $\sigma_{g56} \rightarrow pn$ $\sigma_{g57} \rightarrow pn$ $\sigma_{g58} \rightarrow pn$

$\sigma_{g59} \rightarrow pn$ $\sigma_{g60} \rightarrow pn$ $\sigma_{g61} \rightarrow pn$ $\sigma_{g62} \rightarrow pn$ $\sigma_{g63} \rightarrow pn$ $\sigma_{g64} \rightarrow pn$

$\sigma_{g65} \rightarrow pn$ $\sigma_{g66} \rightarrow pn$ $\sigma_{g67} \rightarrow pn$ $\sigma_{g68} \rightarrow pn$ $\sigma_{g69} \rightarrow pn$ $\sigma_{g70} \rightarrow pn$

$\sigma_{g71} \rightarrow pn$ $\sigma_{g72} \rightarrow pn$ $\sigma_{g73} \rightarrow pn$ $\sigma_{g74} \rightarrow pn$ $\sigma_{g75} \rightarrow pn$ $\sigma_{g76} \rightarrow pn$

$\sigma_{g77} \rightarrow pn$ $\sigma_{g78} \rightarrow pn$ $\sigma_{g79} \rightarrow pn$

APPENDIX G

NJOY99.259 Input File to Produce GROUPR file for Hydrogen

```
moder / Convert data to binary on Unit-21
 1 -21
 'ENDF/B-VI H-1' /
 20 125
 0 /
 reconr / Reconstruct x-sect from resonance parameters on Unit-22
 -21 -22
 'PENDF TAPR FOR H-1 FROM ENDF/B-VI' /
 125 2 /
 0.001  0.0  0.005 / Reconstruction 0.1% (0.5% max)
 '1-H-1 FROM ENDF/B-VI '/
 'PROCESSED BY NJOY-99 '/
 0 /
 broadr / Doppler broadening to Unit-23
 -21 -22 -23
 125 1 0 0 0 /
 0.001/
 300./
 0/
 unresr / Does not do any harm if no unresolved res
 -21 -23 -24
 125 1 4 1
 300.
 1.E10 1.E6 1.E3 10.
 0 /
 groupr
 -21 -26 0  25
 125 1 1 1 1 1 4 1
 '1-H-1 FROM ENDF/B-VI' /
 300.
 1.E10 1.E6 1.E3 10.
 79/ number of neutron groups
 1.0000E-05 5.0000E-04 2.0000E-03 5.0000E-03 1.0000E-02 1.4500E-02
 2.1000E-02 3.0000E-02 4.0000E-02 5.0000E-02 7.0000E-02 1.0000E-01
 1.2500E-01 1.5000E-01 1.8400E-01 2.2500E-01 2.7500E-01 3.2500E-01
 3.6680E-01 4.1399E-01 5.0000E-01 5.3158E-01 6.2506E-01 6.8256E-01
 8.0000E-01 8.7643E-01 1.0000E+00 1.0400E+00 1.0800E+00 1.1253E+00
 1.3000E+00 1.4450E+00 1.8554E+00 2.3824E+00 3.0590E+00 3.9279E+00
 5.0435E+00 1.0677E+01 3.7266E+01 1.0130E+02 2.1445E+02 4.5400E+02
 1.5846E+03 3.3546E+03 7.1017E+03 1.5034E+04 2.1875E+04 2.4176E+04
```

2.6058E+04 3.1828E+04 4.0868E+04 6.7379E+04 1.1109E+05 1.8316E+05
2.9721E+05 3.6883E+05 4.9787E+05 6.0810E+05 7.4274E+05 8.2085E+05
1.0026E+06 1.3534E+06 1.6530E+06 1.9205E+06 2.2313E+06 2.3457E+06
2.3653E+06 2.4660E+06 2.7253E+06 3.0119E+06 3.6788E+06 4.9659E+06
6.0653E+06 7.4082E+06 8.6071E+06 1.0000E+07 1.2214E+07 1.4191E+07
1.7332E+07 1.9640E+07
 399/ number of photon group
 50000 100000 150000 200000 250000 300000 350000 400000
 450000 500000 550000 600000 650000 700000 750000 800000
 850000 900000 950000 1000000 1050000 1100000 1150000
 1200000 1250000 1300000 1350000 1400000 1450000 1500000
 1550000 1600000 1650000 1700000 1750000 1800000 1850000
 1900000 1950000 2000000 2050000 2100000 2150000 2200000
 2250000 2300000 2350000 2400000 2450000 2500000 2550000
 2600000 2650000 2700000 2750000 2800000 2850000 2900000
 2950000 3000000 3050000 3100000 3150000 3200000 3250000
 3300000 3350000 3400000 3450000 3500000 3550000 3600000
 3650000 3700000 3750000 3800000 3850000 3900000 3950000
 4000000 4050000 4100000 4150000 4200000 4250000 4300000
 4350000 4400000 4450000 4500000 4550000 4600000 4650000
 4700000 4750000 4800000 4850000 4900000 4950000 5000000
 5050000 5100000 5150000 5200000 5250000 5300000 5350000
 5400000 5450000 5500000 5550000 5600000 5650000 5700000
 5750000 5800000 5850000 5900000 5950000 6000000 6050000
 6100000 6150000 6200000 6250000 6300000 6350000 6400000
 6450000 6500000 6550000 6600000 6650000 6700000 6750000
 6800000 6850000 6900000 6950000 7000000 7050000 7100000
 7150000 7200000 7250000 7300000 7350000 7400000 7450000
 7500000 7550000 7600000 7650000 7700000 7750000 7800000
 7850000 7900000 7950000 8000000 8050000 8100000 8150000
 8200000 8250000 8300000 8350000 8400000 8450000 8500000
 8550000 8600000 8650000 8700000 8750000 8800000 8850000
 8900000 8950000 9000000 9050000 9100000 9150000 9200000
 9250000 9300000 9350000 9400000 9450000 9500000 9550000
 9600000 9650000 9700000 9750000 9800000 9850000 9900000
 9950000 10000000 10050000 10100000 10150000 10200000
 10250000 10300000 10350000 10400000 10450000 10500000
 10550000 10600000 10650000 10700000 10750000 10800000
 10850000 10900000 10950000 11000000 11050000 11100000
 11150000 11200000 11250000 11300000 11350000 11400000
 11450000 11500000 11550000 11600000 11650000 11700000
 11750000 11800000 11850000 11900000 11950000 12000000
 12050000 12100000 12150000 12200000 12250000 12300000
 12350000 12400000 12450000 12500000 12550000 12600000
 12650000 12700000 12750000 12800000 12850000 12900000
 12950000 13000000 13050000 13100000 13150000 13200000

```
13250000  13300000  13350000  13400000  13450000  13500000
13550000  13600000  13650000  13700000  13750000  13800000
13850000  13900000  13950000  14000000  14050000  14100000
14150000  14200000  14250000  14300000  14350000  14400000
14450000  14500000  14550000  14600000  14650000  14700000
14750000  14800000  14850000  14900000  14950000  15000000
15050000  15100000  15150000  15200000  15250000  15300000
15350000  15400000  15450000  15500000  15550000  15600000
15650000  15700000  15750000  15800000  15850000  15900000
15950000  16000000  16050000  16100000  16150000  16200000
16250000  16300000  16350000  16400000  16450000  16500000
16550000  16600000  16650000  16700000  16750000  16800000
16850000  16900000  16950000  17000000  17050000  17100000
17150000  17200000  17250000  17300000  17350000  17400000
17450000  17500000  17550000  17600000  17650000  17700000
17750000  17800000  17850000  17900000  17950000  18000000
18050000  18100000  18150000  18200000  18250000  18300000
18350000  18400000  18450000  18500000  18550000  18600000
18650000  18700000  18750000  18800000  18850000  18900000
18950000  19000000  19050000  19100000  19150000  19200000
19250000  19300000  19350000  19400000  19450000  19500000
19550000  19600000  19650000  19700000  19750000  19800000
19850000  19900000  19950000  20000000
0.0000E+0  0.000E+00         0         0         1        89
        89         5
1.0000E-5  5.250E-04  9.0000E-3  3.550E-01  1.6000E-2  5.520E-01
2.4000E-2  7.120E-01  2.9000E-2  7.850E-01  3.3000E-2  8.290E-01
4.3000E-2  8.980E-01  5.0000E-2  9.180E-01  5.4000E-2  9.210E-01
5.9000E-2  9.180E-01  7.0000E-2  8.920E-01  9.0000E-2  7.990E-01
1.1200E-1  6.860E-01  1.4000E-1  5.200E-01  1.7000E-1  3.830E-01
2.1000E-1  2.520E-01  3.0000E-1  1.080E-01  4.0000E-1  6.870E-02
4.9000E-1  5.100E-02  5.7000E-1  4.370E-02  6.0000E-1  4.130E-02
1.0000E+0  2.491E-02  4.0000E+0  6.786E-03  9.1180E+3  2.977E-06
2.0000E+4  1.413E-06  3.0700E+4  9.884E-07  6.0700E+4  5.814E-07
1.2000E+5  3.677E-07  2.0100E+5  2.770E-07  2.8300E+5  2.432E-07
3.5600E+5  2.344E-07  3.7700E+5  2.160E-07  3.9900E+5  1.738E-07
4.4200E+5  6.395E-08  4.7400E+5  1.381E-07  5.0200E+5  1.672E-07
5.4000E+5  1.936E-07  6.5000E+5  1.872E-07  7.7000E+5  1.587E-07
9.0000E+5  1.363E-07  9.4100E+5  1.134E-07  1.0000E+6  7.268E-08
1.0500E+6  9.139E-08  1.1200E+6  1.083E-07  1.1900E+6  1.228E-07
1.2100E+6  1.192E-07  1.3100E+6  5.451E-08  1.4000E+6  9.666E-08
2.2200E+6  4.684E-08  2.3500E+6  5.814E-08  2.6300E+6  3.807E-08
3.0000E+6  2.965E-08  4.0000E+6  1.626E-08  5.0000E+6  8.634E-09
6.0000E+6  4.490E-09  8.0000E+6  1.169E-09  1.0000E+7  2.947E-10
1.2570E+7  2.304E-11  1.2600E+7  2.236E-11  1.2700E+7  2.024E-11
1.2800E+7  1.832E-11  1.2900E+7  1.658E-11  1.3000E+7  1.501E-11
```

```
1.3100E+7  1.358E-11  1.3200E+7  1.229E-11  1.3300E+7  1.112E-11
1.3400E+7  1.006E-11  1.3500E+7  9.108E-12  1.3600E+7  8.242E-12
1.3700E+7  7.458E-12  1.3800E+7  6.748E-12  1.3900E+7  6.106E-12
1.4070E+7  5.151E-12  1.4200E+7  4.522E-12  1.4300E+7  4.091E-12
1.4400E+7  3.702E-12  1.4500E+7  3.349E-12  1.4600E+7  3.030E-12
1.4700E+7  2.741E-12  1.4800E+7  2.479E-12  1.4900E+7  2.243E-12
1.5000E+7  2.029E-12  1.5100E+7  1.835E-12  1.5200E+7  1.660E-12
1.5300E+7  1.501E-12  1.5400E+7  1.358E-12  1.5500E+7  1.228E-12
1.5676E+7  1.029E-12  2.0000E+7  1.317E-14 /
 16/
 0/
 0/
 moder
 -23 27
stop
```

Example RADSAT "Pseudo-Isotope" File for Phosphorus

radion_spectra
title "   Phosphorus Induced Photon Spectrum   "
info "   79 neutron groups, 399 gamma groups, Total   "
version "1.0.0"
created "   19-Jan-09 19:2"
last_modified "   30-Jan-09 12:4"
discrete gamma "   Total   " conserve_particles
info " "

1.27	1.5E-06
2.23	5.55E-07

end_discrete
constant gamma "   Total   " conserve_particles
info " "

0.1	0.05	6.535E-09
0.15	0.1	9.456E-09
0.2	0.15	1.149E-08
0.25	0.2	1.286E-08
0.3	0.25	1.373E-08
0.35	0.3	1.422E-08
0.4	0.35	1.447E-08
0.45	0.4	1.451E-08
0.5	0.45	1.44E-08
0.55	0.5	1.412E-08
0.6	0.55	1.373E-08
0.65	0.6	1.33E-08
0.7	0.65	1.284E-08
0.75	0.7	1.238E-08
0.8	0.75	1.196E-08
0.85	0.8	1.161E-08
0.9	0.85	1.127E-08
0.95	0.9	1.093E-08
1	0.95	1.061E-08
1.05	1	1.033E-08
1.1	1.05	1.005E-08
1.15	1.1	9.778E-09
1.2	1.15	9.529E-09
1.25	1.2	9.298E-09
1.3	1.25	9.04E-09
1.35	1.3	8.754E-09
1.4	1.35	8.484E-09

1.45	1.4	8.225E-09
1.5	1.45	7.97E-09
1.55	1.5	7.508E-09
1.6	1.55	7.103E-09
1.65	1.6	6.962E-09
1.7	1.65	6.819E-09
1.75	1.7	6.671E-09
1.8	1.75	6.558E-09
1.85	1.8	6.479E-09
1.9	1.85	6.4E-09
1.95	1.9	6.321E-09
2	1.95	6.242E-09
2.05	2	6.076E-09
2.1	2.05	5.824E-09
2.15	2.1	5.572E-09
2.2	2.15	5.32E-09
2.25	2.2	5.068E-09
2.3	2.25	4.87E-09
2.35	2.3	4.731E-09
2.4	2.35	4.599E-09
2.45	2.4	4.466E-09
2.5	2.45	4.333E-09
2.55	2.5	4.195E-09
2.6	2.55	4.051E-09
2.65	2.6	3.914E-09
2.7	2.65	3.784E-09
2.75	2.7	3.654E-09
2.8	2.75	3.543E-09
2.85	2.8	3.451E-09
2.9	2.85	3.36E-09
2.95	2.9	3.272E-09
3	2.95	3.19E-09
3.05	3	3.097E-09
3.1	3.05	2.991E-09
3.15	3.1	2.888E-09
3.2	3.15	2.791E-09
3.25	3.2	2.696E-09
3.3	3.25	2.623E-09
3.35	3.3	2.574E-09
3.4	3.35	2.53E-09
3.45	3.4	2.489E-09
3.5	3.45	2.447E-09
3.55	3.5	2.403E-09
3.6	3.55	2.359E-09
3.65	3.6	2.318E-09
3.7	3.65	2.279E-09

3.75	3.7	2.24E-09
3.8	3.75	2.149E-09
3.85	3.8	2.005E-09
3.9	3.85	1.862E-09
3.95	3.9	1.719E-09
4	3.95	1.577E-09
4.05	4	1.491E-09
4.1	4.05	1.459E-09
4.15	4.1	1.429E-09
4.2	4.15	1.402E-09
4.25	4.2	1.376E-09
4.3	4.25	1.362E-09
4.35	4.3	1.361E-09
4.4	4.35	1.36E-09
4.45	4.4	1.362E-09
4.5	4.45	1.365E-09
4.55	4.5	1.315E-09
4.6	4.55	1.211E-09
4.65	4.6	1.108E-09
4.7	4.65	1.007E-09
4.75	4.7	9.071E-10
4.8	4.75	6.46E-10
4.85	4.8	4.314E-10
4.9	4.85	4.242E-10
4.95	4.9	4.171E-10
5	4.95	4.106E-10
5.05	5	4.112E-10
5.1	5.05	4.183E-10
5.15	5.1	4.254E-10
5.2	5.15	4.325E-10
5.25	5.2	4.396E-10
5.3	5.25	4.364E-10
5.35	5.3	4.231E-10
5.4	5.35	4.1E-10
5.45	5.4	3.969E-10
5.5	5.45	3.839E-10
5.55	5.5	3.681E-10
5.6	5.55	3.496E-10
5.65	5.6	3.317E-10
5.7	5.65	3.143E-10
5.75	5.7	2.969E-10
5.8	5.75	2.842E-10
5.85	5.8	2.763E-10
5.9	5.85	2.684E-10
5.95	5.9	2.605E-10
6	5.95	2.53E-10

6.05	6	2.481E-10
6.1	6.05	2.452E-10
6.15	6.1	2.422E-10
6.2	6.15	2.393E-10
6.25	6.2	2.364E-10
6.3	6.25	2.298E-10
6.35	6.3	2.197E-10
6.4	6.35	2.1E-10
6.45	6.4	2.003E-10
6.5	6.45	1.906E-10
6.55	6.5	2.152E-10
6.6	6.55	2.74E-10
6.65	6.6	3.329E-10
6.7	6.65	3.917E-10
6.75	6.7	4.507E-10
6.8	6.75	4.454E-10
6.85	6.8	3.755E-10
6.9	6.85	3.057E-10
6.95	6.9	2.36E-10
7	6.95	1.665E-10
7.05	7	1.437E-10
7.1	7.05	1.676E-10
7.15	7.1	1.917E-10
7.2	7.15	2.159E-10
7.25	7.2	2.401E-10
7.3	7.25	2.361E-10
7.35	7.3	2.038E-10
7.4	7.35	1.717E-10
7.45	7.4	1.396E-10
7.5	7.45	1.076E-10
7.55	7.5	9.584E-11
7.6	7.55	6.725E-11
7.65	7.6	3.987E-11
7.7	7.65	5.065E-11
7.75	7.7	6.143E-11
7.8	7.75	5.902E-11
7.85	7.8	4.344E-11
7.9	7.85	2.785E-11
7.95	7.9	1.535E-11
8	7.95	1.052E-11
8.05	8	1.029E-11
8.1	8.05	1.007E-11
8.15	8.1	9.85E-12
8.2	8.15	9.634E-12
8.25	8.2	9.428E-12
8.3	8.25	9.227E-12

8.35	8.3	9.026E-12
8.4	8.35	8.825E-12
8.45	8.4	8.629E-12
8.5	8.45	8.444E-12
8.55	8.5	8.263E-12
8.6	8.55	8.082E-12
8.65	8.6	7.901E-12
8.7	8.65	7.724E-12
8.75	8.7	7.555E-12
8.8	8.75	7.393E-12
8.85	8.8	7.231E-12
8.9	8.85	7.068E-12
8.95	8.9	6.906E-12
9	8.95	6.753E-12
9.05	9	6.608E-12
9.1	9.05	6.463E-12
9.15	9.1	6.319E-12
9.2	9.15	6.175E-12
9.25	9.2	6.034E-12
9.3	9.25	5.901E-12
9.35	9.3	5.772E-12
9.4	9.35	5.644E-12
9.45	9.4	5.516E-12
9.5	9.45	5.388E-12
9.55	9.5	5.265E-12
9.6	9.55	5.149E-12
9.65	9.6	5.037E-12
9.7	9.65	4.924E-12
9.75	9.7	4.811E-12
9.8	9.75	4.698E-12
9.85	9.8	4.59E-12
9.9	9.85	4.488E-12
9.95	9.9	4.39E-12
10	9.95	4.291E-12
10.05	10	4.193E-12
10.1	10.05	4.095E-12
10.15	10.1	3.033E-12
10.2	10.15	1.064E-12
10.25	10.2	1.058E-13
10.3	10.25	1.032E-13
10.35	10.3	1.007E-13
10.4	10.35	9.83E-14
10.45	10.4	9.588E-14
10.5	10.45	9.349E-14
10.55	10.5	9.122E-14
10.6	10.55	8.904E-14

10.65	10.6	8.686E-14
10.7	10.65	8.469E-14
10.75	10.7	8.26E-14
10.8	10.75	8.063E-14
10.85	10.8	7.867E-14
10.9	10.85	7.672E-14
10.95	10.9	7.477E-14
11	10.95	7.293E-14
11.05	11	7.119E-14
11.1	11.05	6.945E-14
11.15	11.1	6.772E-14
11.2	11.15	6.6E-14
11.25	11.2	6.438E-14
11.3	11.25	6.283E-14
11.35	11.3	6.129E-14
11.4	11.35	5.975E-14
11.45	11.4	5.822E-14
11.5	11.45	5.679E-14
11.55	11.5	5.543E-14
11.6	11.55	5.406E-14
11.65	11.6	5.27E-14
11.7	11.65	5.134E-14
11.75	11.7	5.006E-14
11.8	11.75	4.886E-14
11.85	11.8	4.766E-14
11.9	11.85	4.647E-14
11.95	11.9	4.527E-14
12	11.95	4.412E-14
12.05	12	4.304E-14
12.1	12.05	4.2E-14
12.15	12.1	4.095E-14
12.2	12.15	3.991E-14
12.25	12.2	3.886E-14
12.3	12.25	3.789E-14
12.35	12.3	3.698E-14
12.4	12.35	3.608E-14
12.45	12.4	3.517E-14
12.5	12.45	3.427E-14
12.55	12.5	3.336E-14
12.6	12.55	3.252E-14
12.65	12.6	3.174E-14
12.7	12.65	3.096E-14
12.75	12.7	3.018E-14
12.8	12.75	2.941E-14
12.85	12.8	2.863E-14
12.9	12.85	1.412E-14

12.95	12.9	0
13	12.95	0
13.05	13	0
13.1	13.05	0
13.15	13.1	0
13.2	13.15	0
13.25	13.2	0
13.3	13.25	0
13.35	13.3	0
13.4	13.35	0
13.45	13.4	0
13.5	13.45	0
13.55	13.5	0
13.6	13.55	0
13.65	13.6	0
13.7	13.65	0
13.75	13.7	0
13.8	13.75	0
13.85	13.8	0
13.9	13.85	0
13.95	13.9	0
14	13.95	0
14.05	14	0
14.1	14.05	0
14.15	14.1	0
14.2	14.15	0
14.25	14.2	0
14.3	14.25	0
14.35	14.3	0
14.4	14.35	0
14.45	14.4	0
14.5	14.45	0
14.55	14.5	0
14.6	14.55	0
14.65	14.6	0
14.7	14.65	0
14.75	14.7	0
14.8	14.75	0
14.85	14.8	0
14.9	14.85	0
14.95	14.9	0
15	14.95	0
15.05	15	0
15.1	15.05	0
15.15	15.1	0
15.2	15.15	0

15.25	15.2	0
15.3	15.25	0
15.35	15.3	0
15.4	15.35	0
15.45	15.4	0
15.5	15.45	0
15.55	15.5	0
15.6	15.55	0
15.65	15.6	0
15.7	15.65	0
15.75	15.7	0
15.8	15.75	0
15.85	15.8	0
15.9	15.85	0
15.95	15.9	0
16	15.95	0
16.05	16	0
16.1	16.05	0
16.15	16.1	0
16.2	16.15	0
16.25	16.2	0
16.3	16.25	0
16.35	16.3	0
16.4	16.35	0
16.45	16.4	0
16.5	16.45	0
16.55	16.5	0
16.6	16.55	0
16.65	16.6	0
16.7	16.65	0
16.75	16.7	0
16.8	16.75	0
16.85	16.8	0
16.9	16.85	0
16.95	16.9	0
17	16.95	0
17.05	17	0
17.1	17.05	0
17.15	17.1	0
17.2	17.15	0
17.25	17.2	0
17.3	17.25	0
17.35	17.3	0
17.4	17.35	0
17.45	17.4	0
17.5	17.45	0

17.55	17.5	0
17.6	17.55	0
17.65	17.6	0
17.7	17.65	0
17.75	17.7	0
17.8	17.75	0
17.85	17.8	0
17.9	17.85	0
17.95	17.9	0
18	17.95	0
18.05	18	0
18.1	18.05	0
18.15	18.1	0
18.2	18.15	0
18.25	18.2	0
18.3	18.25	0
18.35	18.3	0
18.4	18.35	0
18.45	18.4	0
18.5	18.45	0
18.55	18.5	0
18.6	18.55	0
18.65	18.6	0
18.7	18.65	0
18.75	18.7	0
18.8	18.75	0
18.85	18.8	0
18.9	18.85	0
18.95	18.9	0
19	18.95	0
19.05	19	0
19.1	19.05	0
19.15	19.1	0
19.2	19.15	0
19.25	19.2	0
19.3	19.25	0
19.35	19.3	0
19.4	19.35	0
19.45	19.4	0
19.5	19.45	0
19.55	19.5	0
19.6	19.55	0
19.65	19.6	0
19.7	19.65	0
19.75	19.7	0
19.8	19.75	0

19.85	19.8	0
19.9	19.85	0
19.95	19.9	0
20	19.95	0

end_constant
end_radion_spectra

REFERENCES

1. L.E. SMITH, et al., "Coupling Deterministic and Monte Carlo Transport Methods for the Simulation of Gamma-Ray Spectroscopy Scenarios," submitted to *IEEE Trans. Nucl. Sci.*, December 2008.

2. *MCNP—A General Monte Carlo N-Particle Transport Code*, Los Alamos National Laboratory, LA-UR-03-1987, 2003.

3. *NJOY99.0 – Code System for Producing Pointwise and Multigroup Neutron and Photon Cross-Sections from ENDF/B Data,* Oak Ridge National Laboratory, PSR-480/NJOY99.0 (2000).

4. G.W. McKinney, "MCNP Applications for the 21st Century," SNA 2000 Conference, Tokyo, Japan, September 2000.

5. *MCNPX^{TM} User's Manual*, Los Alamos National Laboratory, LA-UR-02-2607, 2002.

6. S. Agostinelli, J. Allison, K. Amako, J. Apostolakis, H. Araujo, P. Arce, et al., "GEANT4 – A Simulation Toolkit," *Nucl. Inst. Meth. A*, 506, 250-303, 2003.

7. *Fluka: a multi-particle transport code,* CERN European Organization for Nuclear Research, CERN-2005-010, 2005.

8. *The MARS Code System User's Guide Version 15*, Fermi National Accelerator Laboratory, 2009.

9. *PENELOPE-2006: A Code System for Monte Carlo Simulation of Electron and Photon Transport,* Workshop Proceedings Barcelona Spain, ISBN 92-64-02301-1, 2006

10. J.J. Duderstadt and W.R. Martin, "Transport Theory," John Wiley & Sons, Inc., New York, 1979.

11. J.M. McGhee, et al., *Attila User's Manual*, Transpire, Inc. (2007).

12. W.A. Rhoades and D.B. Simpson, "The TORT Three-Dimensional Discrete Ordinates Neutron/Photon Transport Code," Oak Ridge National Laboratory, ORNL/TM-13221, 1997.

13. R.E. Alcouffe, R.S. Baker, J.A. Dahl, S.A. Turner, and R. Ward, "PARTISN: A Time-Dependent, Parallel Neutral Particle Transport Code System," Los Alamos

National Laboratory, LA-UR-05-3925, 2005.

14.   R.E. Alcouffe, R.S. Baker, F.W. Brinkley, D.R. Marr, R.D. O'Dell, and W.F. Walters, "DANTSYS: A Diffusion Accelerated Neutral Particle Transport Code System," Los Alamos National Laboratory, LA-12969-M, 1995.

15.   T.A. Brunner, "Forms of Approximate Radiation Transport," SAND2002-1778, Sandia National Laboratory, 2002.

16.   T.A. Wareing, J.M. McGhee, and J.E. Morel, "ATTILA, A Three-Dimensional, Unstructured Tetrahedral Mesh Discrete Ordinates Code," *Trans. Am. Nucl. Soc.*, 75, 146, 1996.

17.   D.J. Mitchell and J. Mattingly, "Rapid Computation of Gamma-ray Spectra for One-Dimensional Source Models," American Nuclear Society Annual Meeting, San Diego, 2008.

18.   I. Davis, (private communication), 2008.

19.   M.W. Shaver, L.E. Smith, R.T. Pagh, E.A. Miller, and R.S. Wittman, "The Coupling of a Deterministic Transport Field Solution to a Monte Carlo Boundary Condition for the simulation of Large Gamma-Ray Spectrometers," submitted to *Nuclear Technology*, May 2008.

20.   *SCALE – Version 5.1*, Oak Ridge National Laboratory, ORNL/TM-2005/39, 2006.

21.   E.S. Varley and J. Mattingly, "Rapid Feynman-Y Synthesis: Kynea3 Cross-Section Library Development," *Trans. Amer. Nucl. Soc.*, Vol. 98, pp.575 – 576 (2008).

22.   J. E. White, et al., "VITAMIN-B6: A Fine-Group Cross-Section Library Based on ENDF/B-VI for Radiation Transport Applications," Proc. of the International Conference on Nuclear Data for Science and Technology, Gatlinburg, TN, pp. 733-736 (1994).

23.   J.E. White, et al., "BUGLE-96: A Revised Multigroup Cross-Section Library for LWR Applications Based on ENDF/B-VI Release 3," presented at the American Nuclear Society Radiation Protection & Shielding Topical Meeting, Falmouth, MA (1996).

24.   "SolidWorks" <http://www.solidworks.com/> (Accessed May 13, 2008).

25.   T.A. Wareing, J.M. McGhee, J.E. Morel, S.D. Pautz, "Discontinuous Finite Element Sn Methods on Three-Dimensional Unstructured Grids," Nucl. Sci.

Engr., Vol. 138, Number 2, July 2001.

26.   T.A. Wareing, J.E. Morel, J.M. McGhee, "Coupled Electron-Photon Transport Methods on 3-D Unstructured Grids," Trans Am. Nucl. Soc., Washington D.C., Vol 83, 2000.

27.   J.J. Duderstadt and L.J. Hamilton, "Nuclear Reactor Analysis," John Wiley & Sons, Inc., New York, 1976.

28.   I.I. Bondarenko, Ed., "Group Constants for Nuclear Reactor Calculations," Consultants Bureau, New York, 1964.

29.   N.M. Greene, "BONAMI: Resonance Self-Shielding by the Bondarenko Method," Ridge National Laboratory, ORNL/NUREG/CSD-2/V2/R6, 1998.

30.   L.J. Lorence, "CEPXS/ONELD Version 2.0: A Discrete Ordinates Code Package for General One-Dimensional Coupled Electron-Photon Transport," *IEEE Trans. Nucl. Sci.*, 39, 1031, 1992.

31.   Kenneth Barbalace. Periodic Table of the Elements. EnvironmentalChemistry.com. 1995 - 2009. Accessed on-line: 4/22/2009 http://EnvironmentalChemistry.com/yogi/periodic/